



The
University
Of
Sheffield.

**DEEP LEARNED ELECTRICAL RESISTANCE
TOMOGRAPHY APPLICATIONS IN
STRUCTURAL HEALTH MONITORING**

Liang Chen

Supervisors:

Dr. Danny Smyl

Dr. Shan-Shan Huang

A thesis submitted for the degree of Doctor of Philosophy

Department of Civil and Structural engineering

The University of Sheffield

July 2022

Contents

| | |
|---|-----------|
| 1 Acknowledgement | 6 |
| List of Figures | 7 |
| List of Tables | 11 |
| 2 Abstract | 14 |
| 3 Introduction | 16 |
| 3.1 Background | 16 |
| 3.1.1 Strucutral Health Monitoring | 16 |
| 3.1.2 Electrical Resistance Tomography and Forward Model | 16 |
| 3.1.3 Machine learning and neural network | 22 |
| 3.1.4 Artificial Neural Network | 24 |
| 3.1.5 Convolutional Neural Network | 27 |
| 3.1.6 Activation Function | 29 |
| 3.1.7 Training of Neural Network | 33 |
| 3.1.8 Back-propagation | 35 |
| 3.2 Aim of the thesis | 39 |
| 3.3 Connections between the published papers | 40 |
| 3.4 Contribution to the publications | 41 |
| 4 Novelty of the publications | 45 |
| 5 Probabilistic Cracking Prediction via Deep Learned Electrical Tomography | 46 |
| 5.1 Abstract | 46 |
| 5.2 Introduction | 47 |
| 5.2.1 Background | 47 |
| 5.2.2 Machine learning and damage prediction | 48 |
| 5.2.3 Paper structure | 51 |

| | | |
|----------|--|-----------|
| 5.3 | Electrical Resistance Tomography and Direct Inversion | 52 |
| 5.3.1 | The ERT inverse problem | 53 |
| 5.4 | Training Data Acquisition and Training Methodology | 55 |
| 5.4.1 | Overview | 55 |
| 5.4.2 | Crack pattern generation | 58 |
| 5.4.3 | Data Processing and Training | 58 |
| 5.5 | Results and Discussion | 64 |
| 5.6 | Flexural Crack Reconstruction | 64 |
| 5.6.1 | Shear Crack Reconstruction | 65 |
| 5.6.2 | Discussion | 68 |
| 5.7 | Conclusions | 71 |
| 5.8 | Acknowledgements | 71 |
| 6 | Predicting strain and stress fields in self-sensing nanocomposites using deep learned electrical tomography | 72 |
| 6.1 | Abstract | 72 |
| 6.2 | Introduction | 72 |
| 6.2.1 | Background and context | 72 |
| 6.2.2 | Machine learning and neural networks | 75 |
| 6.2.3 | Paper structure | 76 |
| 6.3 | Electrical Resistance Tomography | 77 |
| 6.3.1 | Forward model | 78 |
| 6.3.2 | ERT inverse problem | 80 |
| 6.4 | Experiment Data Acquisition | 82 |
| 6.4.1 | CNF specimen and experiment set up | 82 |
| 6.4.2 | Piezoresistivity model | 84 |
| 6.5 | Deep learned ERT tomography framework | 85 |
| 6.5.1 | Overview | 85 |
| 6.5.2 | Selection of regression based machine learning approaches | 86 |
| 6.6 | Training Data Acquisition and Neural Network Methodology | 87 |

| | | |
|----------|--|------------|
| 6.6.1 | Integration of the elastic FE model, CEM and piezoresistivity model | 88 |
| 6.6.2 | Neural network architecture and training | 93 |
| 6.7 | Results and Discussion | 96 |
| 6.7.1 | Results | 97 |
| 6.7.2 | Discussion | 102 |
| 6.8 | Conclusion | 106 |
| 6.9 | Acknowledgement | 107 |
| 7 | Data-driven superresolution of numerical simulations and experimental measurements | 108 |
| 7.1 | Abstract | 108 |
| 7.2 | Introduction | 108 |
| 7.3 | Data-driven superresolution of reduced order models and implementation in inverse problems | 111 |
| 7.3.1 | Approach to superresolution of reduced order models | 111 |
| 7.3.2 | Mechanical simulation study | 112 |
| 7.4 | Electrical Resistance Tomography Inversion | 116 |
| 7.5 | The ERT Forward Model | 117 |
| 7.6 | ERT Inverse Problem | 118 |
| 7.6.1 | Experimental Inversion Study | 120 |
| 7.7 | Selection of the architecture of NN | 124 |
| 7.7.1 | Rationale of selecting NN | 124 |
| 7.7.2 | Architecture of selected NNs | 125 |
| 7.8 | Results | 127 |
| 7.8.1 | Mechanical simulation study evaluation | 127 |
| 7.8.2 | Experimental inversion study validation | 128 |
| 7.9 | Discussion | 131 |
| 7.10 | Conclusions | 133 |
| 8 | Conclusion | 134 |

9 Bibliography **136**

10 Appendix **154**

 10.1 Hyperparameter Tuning in Neural Network Training 154

 10.2 Generating and Pre-Process of training data for Neural Networks 155

1 Acknowledgement

Firstly I want to express my sincerest gratitude to Dr. Danny Smyl and Dr. Shan-Shan Huang who are my academic supervisors during my PhD study. This has been a special 3 years due to the pandemic, I am really grateful for all the efforts they made to help me throughout this journey. I also want to thank for the financial and mental support from my family members.

List of Figures

| | | |
|----|---|----|
| 1 | Voltage Measurement in ERT (Karhunen, Seppänen, Lehtikoinen, Monteiro & Kaipio 2010) | 17 |
| 2 | 2-Point and 4-Point Electrical Conductivity Measurement Technique Hou & Lynch (2009) | 17 |
| 3 | Electrodes set up and current flow of Wenner Technique Hou & Lynch (2009) | 19 |
| 4 | Typical ERT experiment set up Hallaji et al. (2014) | 20 |
| 5 | A typical ANN architecture with two hidden layers | 24 |
| 6 | Feature detection operation of input image in CNN | 28 |
| 7 | Construction of convolutional layer in CNN | 29 |
| 8 | Max pooling operation to construct pooled feature map in CNN | 29 |
| 9 | Plot of a typical binary step function giving output of 1 and 0 | 30 |
| 10 | Plot of unipolar sigmoid function spanning between (0,1) | 31 |
| 11 | Plot of bipolar sigmoid function spanning between (-1,1) | 31 |
| 12 | Plot of hyperbolic tangent function shows steeper gradient around origin . . | 32 |
| 13 | Plot of softplus and rectifier function shows their smooth transition difference | 33 |
| 14 | Domain discretization for the flexural cracking investigation consisting of 2557 nodes and 4896 elements. | 57 |
| 15 | Domain discretization for the shear cracking investigation consisting of 5047 nodes and 9680 elements. | 57 |
| 16 | Sample conductivity distribution used in flexural cracking training data. . . . | 58 |
| 17 | Sample conductivity distribution used in shear cracking training data. | 59 |
| 18 | Schematic trained ANN architecture. | 62 |
| 19 | Schematic trained CNN architecture. | 63 |
| 20 | Loss function minimization for an ANN used in this work. | 63 |
| 21 | Loss function minimization for an CNN used in this work (non-segmented data). | 64 |
| 22 | NN predictions of experimental flexural cracking patterns. | 66 |
| 23 | NN predictions of simulated shear cracking patterns. | 67 |

| | | |
|----|--|-----|
| 24 | a) Photograph of experimental specimen with electrodes, grip tabs, and gauge section shown. b) SEM images of the underlying CNF network including a close-up of a single CNF. | 83 |
| 25 | Flowchart of determining the mechanical states via ERT and a GA. | 86 |
| 26 | Flowchart of the proposed deep learned framework. | 86 |
| 27 | Discretized domain that is used in the integrated model: a) Domain discretization of the gauge section of the CNF/epoxy specimen consisting of 1576 elements and 870 nodes; b) Boundary conditions that are implemented in the elastic FE model. The domain is fixed in x and y directions at the bottom. Displacements are allowed in y-direction on top layer nodes. | 89 |
| 28 | Flowchart of the training data generation path. | 91 |
| 29 | Sample strain distribution within N_ϵ training data. | 92 |
| 30 | Sample stress distribution within N_σ training data. | 92 |
| 31 | Loss function minimization for the predictor N_ϵ | 96 |
| 32 | Loss function minimization for the predictor N_σ | 96 |
| 33 | Comparison between the predicted strain and stress distributions and their corresponding simulation samples: a) Prediction of the strain field (left) and simulated strain field from the integrated model (right); b) Prediction of the stress field (left) and simulated stress field from the integrated model (right). | 98 |
| 34 | Neural network predictions of experimental data (top two rows) and the DIC reconstructions (bottom two rows) considering different displacement states (Hassan & Tallman 2020 <i>b</i>). | 101 |
| 35 | Simulated homogeneous voltages and experimental voltage measurements prior to error correction. | 103 |
| 36 | Simulated homogeneous voltages and experimental voltage measurements after error correction. | 103 |
| 37 | Histogram plot of stress training samples prior to data processing. | 104 |
| 38 | Histogram plot of stress training samples posterior to data processing. | 104 |

| | | |
|----|--|-----|
| 39 | Boundary and loading condition of the domain used for the mechanical simulation study. The domain is fixed in x and y direction at the left boundary. Displacement in X direction are allowed on the right bottom node. Nodal forces are applied on the right boundary. | 113 |
| 40 | Flowchart of decomposing the displacement vectors modelled on lower order mesh ($p = 1$). | 114 |
| 41 | Flowchart of decomposing the displacement vectors modelled on lower order mesh ($p = 2$). | 114 |
| 42 | Flowchart of the training process of NNs S_x and S_y for the mechanical simulation study | 115 |
| 43 | Experimental set up of a KIT4 current injection module which consists of a water tank with a plastic inclusion (Hauptmann, Kolehmainen, Mach, Savolainen, Seppänen & Siltanen 2017). | 121 |
| 44 | Water tank discretization consisting of with 1145 Nodes and 2144 Elements. | 123 |
| 45 | Flowchart of reconstructing the difference of the internal conductivity via solving the conventional ERT inverse problem based on high fidelity measurements with TV prior regularization. | 123 |
| 46 | Flowchart of reconstructing difference of the internal conductivity via proposed SR approach based on low fidelity measurements with TV prior regularization. | 124 |
| 47 | Loss function minimization of SR operator S_x | 126 |
| 48 | Loss function minimization of SR operator S_y | 126 |
| 49 | Loss function minimization of SR operator S_V | 128 |
| 50 | Comparison between the displacement field yielded from the SR approach and the simulation results: a) Predicted displacement field modelled on $p = 2$ mesh which is then interpolated on $p = 1$ mesh; b) Simulated displacement field modelled on $p = 2$ mesh which is then interpolated on $p = 1$ mesh; c) Simulated displacement field modelled on $p = 1$ mesh. | 129 |

51 Comparison between the conventional reconstruction of $\Delta\sigma$ based on simulated high fidelity measurements and the reconstruction via proposed SR approach:
a) TV prior reconstruction of $\Delta\sigma$ based on high fidelity, simulated measurements based on 16 electrodes; b) TV prior reconstruction of $\Delta\sigma$ based on up-sampled voltage measurements via SR approach. 130

52 Comparison between the experimental images of the inclusions, the conventional reconstructions of $\Delta\sigma$ and the reconstructions of $\Delta\sigma$ via the SR approach considering two different experimental inclusion cases: a) Experimental positioning images of circular and rectangular inclusions in the water tank; b) TV prior reconstruction of $\Delta\sigma$ based on low fidelity experimental measurements (8 electrodes); c) TV prior reconstruction of $\Delta\sigma$ based on high fidelity experimental measurements (16 electrodes); d) TV prior reconstruction of $\Delta\sigma$ based on up-sampled low fidelity experimental measurements (8 electrodes). 131

List of Tables

| | | |
|----|---|-----|
| 1 | Geometry and mesh details for the flexural cracking investigation. | 56 |
| 2 | Geometry and mesh details for the shear cracking investigation. | 56 |
| 3 | Summary of the ANN architecture used for reconstructing flexural cracks. | 61 |
| 4 | Summary of ANN architecture used for reconstructing shear cracks. | 61 |
| 5 | Summary of CNN architecture used for reconstructing shear cracks. | 62 |
| 6 | Mean square errors for shear crack predictions. | 69 |
| 7 | Geometry and mesh details for the adapted CNF specimen domain. | 88 |
| 8 | Summary of the ANN architecture (N_ϵ) for predicting strain distributions. | 94 |
| 9 | Summary of the ANN architecture (N_σ) for predicting stress distributions. | 95 |
| 10 | Computation runtimes for predicting strain and stress distributions using NNs and ERT plus GA considering different displacement cases. | 100 |
| 11 | The average first principal strain ($\bar{\epsilon}_p$) and stress distribution ($\bar{\sigma}_p$) obtained via NNs and ERT plus GA considering different displacement cases (d). | 100 |
| 12 | The L_2 norm of first principal strain ($\ \epsilon_p\ ^2$) and stress distribution ($\ \sigma_p\ ^2$) obtained via NNs and ERT plus GA considering different displacement cases (d). | 100 |
| 13 | Geometry and mesh details for the water tank. | 122 |
| 14 | Summary of the NN architecture S_x and S_y for up-sampling displacement fields modelled on lower order mesh. | 125 |
| 15 | Summary of the NN architecture S_V for up-sampling low fidelity voltage measurements based on 8 electrodes. | 127 |
| 16 | MSE and norm error analysis of the mechanical simulations study. | 128 |

Nomenclature

| | | | |
|---------------|---|--------------------|---|
| V_{16} | Voltage measurement from 16 electrodes | ϵ_p | strain distribution |
| V_8 | Voltage measurement from 8 electrodes | γ | Conductivity distribution (Paper 2) |
| $x_{sim,p=1}$ | Simulated x direction displacement on lower order mesh | γ_c | composite conductivity |
| $x_{sim,p=2}$ | Simulated x direction displacement on higher order mesh | γ_f | nanofiller conductivity |
| $y_{sim,p=1}$ | Simulated y direction displacement on lower order mesh | γ_m | matrix conductivity |
| $y_{sim,p=2}$ | Simulated y direction displacement on higher order mesh | λ | Scalar regularization |
| S_x | NNs operators aiming to learn the mapping between displacements vectors computed from lower and higher order meshes on x directions | λ_1 | nanofiller waviness ratio |
| S_y | NNs operators aiming to learn the mapping between displacements vectors computed from lower and higher order meshes on y directions | \mathcal{A} | Trained NN |
| S | learned function | \mathcal{L} | Binary cross-entropy loss |
| α | regularization hyperparameter | N | the length of the FE solution vectors |
| ϵ_1 | non-random model error term | Ω | target domain boundary |
| | | $\partial\Omega$ | target domain boundary |
| | | ϕ | the potential barrier height felt by a tunneling electron |
| | | σ | Conductivity distribution |
| | | σ_p | stress distribution |
| | | \tilde{p}_σ | Training data output |
| | | d_f | nanofiller diameter |
| | | dS | infinitesimal surface |
| | | e | Error term |

| | | | |
|-----------------|--|-------------|---|
| e_1 | charge of an electron | $U(\sigma)$ | finite element forward model |
| e_l | l^{th} electrode | $u(x)$ | potential distribution |
| h | Planck's constant | u_A | accurate FE solution |
| I_l | current injection on l^{th} electrode | u_R | reduced order FE solution |
| J | Jacobian matrix | U_l | potential measurement on l^{th} electrode |
| L_e | Cholesky factorized noise weighting (Paper 2) | V | measured voltages |
| l_f | nanofiller length | v_f | nanofiller volume fraction |
| L_R | Cholesky factorized noise weighting | V_0 | the experimental voltage measurements taken from the unstressed reference state |
| $L_{\Delta e}$ | regularization matrices | V_h | voltage simulations from an assumed homogeneous and unstressed sample |
| L_γ | regularization matrices (Paper 2) | W | diagonal noise weighting matrix |
| m | mass of an electron | w | Network weights |
| $N_\epsilon(V)$ | the average inter-nanofiller separation distance | x | Cartesian coordinates |
| $N_\sigma(V)$ | represent the learned NN operators used for predicting | y_i | Desired output (Paper 2) |
| P | percolation probability | y_t | Binary sample labels |
| p_t | Binary predictions output | Yx_i | Predicted output (Paper 2) |
| t | the average inter-nanofiller separation distance | z_l | contact impedance |
| | | N | Total number of training samples |

2 Abstract

In recent studies, electrical resistance tomography (ERT) has been explored as a non-destructive testing imaging modality in conjunction with structural health monitoring (SHM). This imaging modality has been shown to be able to locate cracks in cement-based materials as well as reconstruct strain and stress distributions in nano-composite materials. However, due to the ill-conditioned nature of the ERT inverse problem, the computational cost of solving such problems can be high. In order to reduce the overall computational cost of solving the ERT inverse problem in practical applications, we propose using a deep learning approach to address this challenge. The deep-learned ERT frameworks have been successfully implemented and validated using simulation and experimental data for various materials relevant to SHM. The results indicate that the deep-learned ERT frameworks are feasible for implementation in SHM applications.

In my first publication, I successfully used feed-forward (ANN) and convolutional neural network (CNN) to directly solve the ERT inverse problem to predict the probabilistic spatial flexural/shear crack distribution on cement-based materials. The feasibility of the deep-learned framework was confirmed by experimental and simulated patterns, which showed the potential of using neural networks to reconstruct crack locations with significantly reduced computational cost.

In my second publication, I explored a deep-learned framework for reconstructing strain/stress distributions in nano-composites. This research has the potential to obtain the mechanical state of nano-composites without prior knowledge of forces, boundary conditions, etc. The feasibility of this framework could directly solve the ERT problem associated with reduced computational cost based on ERT measurements alone.

In my third research, I focused on using a data-driven approach to super-resolve low-fidelity data to achieve high-fidelity results without compromising accuracy with limited computational power. Super-resolution of mechanical finite elements models with lower-order meshes was used for the simulation study, while reduced ERT measurements were used for the ex-

perimental inverse problem. The results indicate that there is potential for using data-driven super-resolution to achieve meaningful results from low-fidelity data.

The limitations and potential future research are also discussed in this thesis to provide a more comprehensive view of the deep-learned methodologies.

3 Introduction

3.1 Background

3.1.1 Structural Health Monitoring

Structural health monitoring (SHM) methodologies are widely applied in civil and aerospace industries to assess structural states. Aiming at predicting and preventing catastrophic structural failures, SHM approaches should at least provide accurate monitoring/prediction on the location and severity of potential structural damages. Farrar et al. has referred to the detection, localization, classification, assessment and prediction as hierarchies for SHM (Farrar & Worden 2012). In this thesis, my research is focusing on the first three hierarchies with reduced computational cost. Historically speaking, SHM originated from railway tap testing (Stanley & Moore 1995) and has since draw substantial research interests in the past years aiming to develop methodologies that could monitor the structures qualitatively and quantitatively.

During this period there are SHM technologies that were developed into commercially available applications. There are various commercially available non-destructive testing (NDT) approaches such as ultrasonic, electromagnetic, radiographic, photographic and infrared testings. However, few traditional NDT modalities (e.g. electromagnetic testing) have disadvantages such as the following: 1) high energy consumption, 2) high operational cost due to the transportation and implementation of the equipment and 3) can not be implemented on a large scale. For example, ultrasonic testing can only monitor structures locally rather than reflecting the structural health globally, hence the industry is in need of a modality that could offer accurate and continuous monitoring with lower costs. (Gholizadeh 2016, Mutlib, Baharom, El-Shafie & Nuawi 2016, Montinaro, Cerniglia & Pitarresi 2018, Kong & Li 2018, Ma & Li 2018).

3.1.2 Electrical Resistance Tomography and Forward Model

Electrical resistance tomography (ERT) is an NDT technique which reconstructs the internal conductivity of the domain based on boundary voltage measurements. This technique was chosen to be the main approach for this thesis due to the following advantages: 1) lower

implementation costs, 2) lower energy consumption and 3) faster data collection (Liu, Smyl & Du 2020).

In a typical ERT experiment, firstly, alternating or direct current is injected on the boundary electrodes shown in 1. Then potential difference measurements between different electrodes

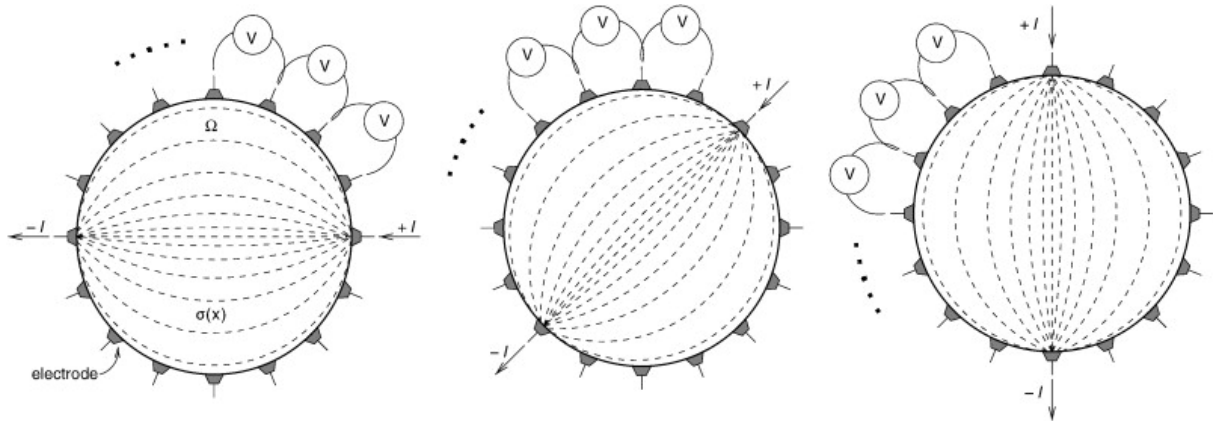


Figure 1: Voltage Measurement in ERT (Karhunen, Seppänen, Lehtikoinen, Monteiro & Kaipio 2010)

will then be taken and recorded. The voltage measurement data will be used to solve the ERT ill-posed inverse problem. As a result, the internal conductivity distribution is reconstructed.

In this paragraph, I briefly introduce the historical development of ERT experimental set up (Hou & Lynch 2009). Experimental ERT measurement was developed starting from two-point technique introduced by (Vilhunen, Kaipio, Vauhkonen, Savolainen & Vauhkonen 2002). As shown in Figure 2 Since direct currents are injected on two boundary electrodes and the

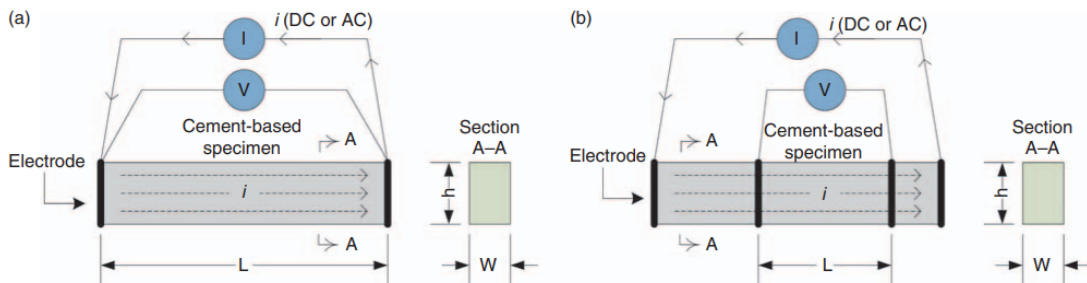


Figure 2: 2-Point and 4-Point Electrical Conductivity Measurement Technique Hou & Lynch (2009)

voltage differences are taken between them. According to Ohm's law, the conductivity can be calculated as following.

$$\sigma = \frac{I}{V} \frac{L}{wh} \quad (1)$$

The above testing method was firstly used in rapid chloride penetration protocols (Layssi, Ghods, Alizadeh & Salehi 2015, Bentz 2007). However two point measurement have two disadvantages as following: 1) Internal electrochemical reaction induces reduced conductivity and the electrode-specimen interface. This could potentially damage the accuracy at the electrode position however this error is negligible since we are not considering data from damaged electrode and 2) the polarization of the specimen. A possible solution is to switch from direct current to alternating current which could provides insufficient time for the above two problems to develop. In addition, another experimental technique known as four point measurement technique is similar to two point measurement technique with two additional electrodes which separate the excited electrodes. Nonetheless, the above equations still holds for this technique and offers more accurate results (Hou & Lynch 2009).

From other studies, Gower and Millard proposed an modified four point measurement technique (Gowers & Millard 1999) known as Wenner technique. This technique installs four electrodes at the surface of the specimen with equal spacing. In their research, specimens were assumed as a infinite half-space, the mathematical expression for this technique is as following

$$\sigma = \frac{I}{V} \frac{1}{2\pi a} \quad (2)$$

Experimental setting up can be seen in [Figure 3](#). However this experimental technique is

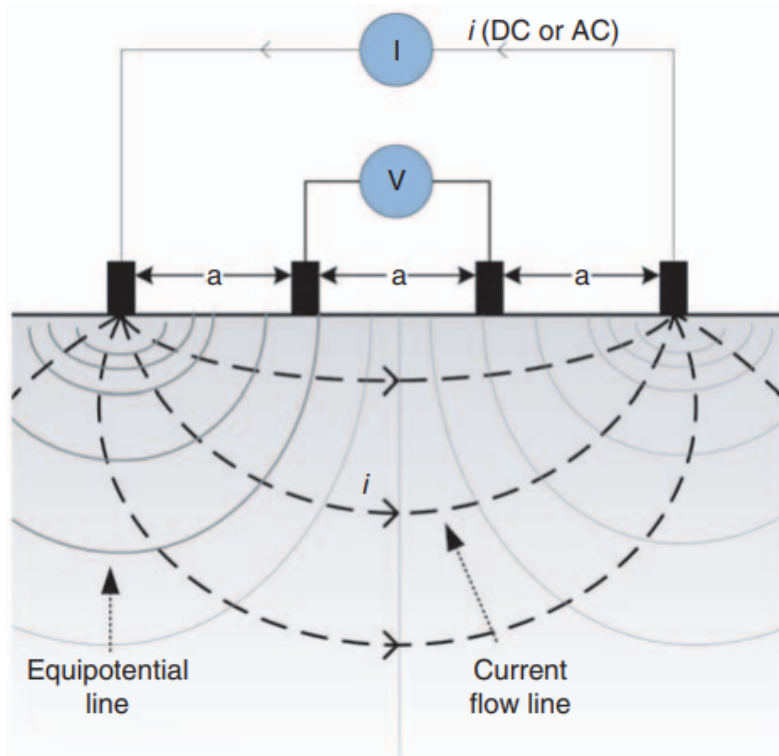


Figure 3: Electrodes set up and current flow of Wenner Technique Hou & Lynch (2009) limited by the assumption of infinite half-space which is only satisfied when the thickness of specimen is at least four times of electrode spacing.

Furthermore, researchers discovered that electrical impedance tomography (EIS) with frequency response analyser can be used to measure impedance of the specimen (Gholizadeh 2016, Hou & Lynch 2009). EIS, however, is not capable of including inhomogeneity of concrete conductivity hence is not accurate in terms of its spatial distribution.

ERT is similar to EIS however is another typical electrical measurement modality. Typical modern experimental set up ERT measurement KIT4 is shown in Figure 4. Electrodes are installed the boundary surface of the specimen, current is injected and taken out in two electrodes while potential difference is measured in pair of adjacent electrodes. The injection and measurement protocols varies, for example voltage can be taken as pairs of one fixed electrode with another electrode following clock-wise order. As explored by Hallai et al. (Hallaji, Seppänen & Pour-Ghaz 2014) and Smyl et al. (Smyl, Pour-Ghaz & Seppänen 2018),

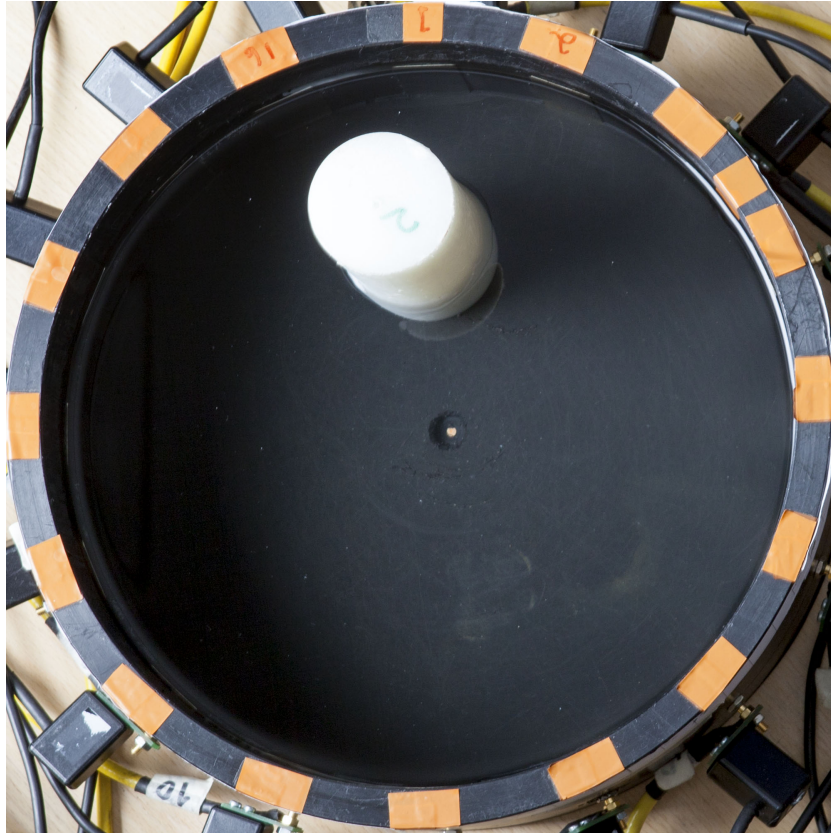


Figure 4: Typical ERT experiment set up Hallaji et al. (2014)

sensing skins can be used to provide quantitative reconstruction of cracks hence copper or silver sensing skins are often implemented in ERT experiments.

With the advantages of ERT mentioned above, ERT still suffers from high computational costs from solving ill-conditioned ERT inverse problems. The ill conditioning of ERT problems is mainly due to the following reasons: 1) noisy voltage measurement data, 2) ill-conditioned Hessian matrices computed while implementing the optimization algorithm, 3) diffusive nature of the injected currents and 4) numerical modelling errors (Chen, Hassan, Tallman, Huang & Smyl 2022). Since ERT is an ill conditioned inverse problem, in order to solve such problem we need to establish a forward model describing the explicit relationship between boundary voltage measurements and the internal conductivity. Such model is known as Complete Electrode Model (CEM) (Cheng, Isaacson, Newell & Gisser 1989, Karhunen, Seppänen, Lehtikoinen, Blunt, Kaipio & Monteiro 2010) which consists a partial differential

equation with boundary conditions shown as following:

$$\nabla \cdot (\sigma \nabla u) = 0, x \in \Omega \quad (3)$$

$$\int_{e_l} \sigma \frac{\partial u}{\partial n} dS = I_l, l = 1, \dots, L \quad (4)$$

$$\sigma \frac{\partial u}{\partial n} = 0, x \in \partial\Omega \setminus \cup_{l=1}^L e_l \quad (5)$$

$$u + z_l \sigma \frac{\partial u}{\partial n} = U_l, l = 1, \dots, L. \quad (6)$$

Equation (3) is the Laplace equation which describes steady-state diffusion (Tallman & Smyl 2020) in a target domain Ω with a boundary $\partial\Omega$. Further, x represents Cartesian coordinates within the domain while $\sigma(x)$ and $u(x)$ represents the conductivity distribution and potential distribution within the target. Equations (4) to (6) provide the necessary boundary conditions to solve equation (3), where e_l represents the l^{th} electrode hence U_l is the potential measurement on the corresponding electrode. I_l represents the current injection on l^{th} electrode. dS represents the infinitesimal surface of Ω while z_l represents the contact impedance between the l^{th} electrode and the internal domain. Equations (4) to (6) provide an accurate forward model solution by taking the shunting effects of electrodes and their contact impedance into account (Vauhkonen 1997). Lastly, in order to satisfy the current conservation law and fixed potential reference level which would ensure an unique solution, the following equations are written to complete the CEM

$$\sum_{l=1}^L I_l = 0 \quad (7)$$

$$\sum_{l=1}^L U_l = 0. \quad (8)$$

We would like to emphasize that the CEM describes the forward problem where the internal conductivity is known, from which the electrode potentials can be computed. As such, we adopt the CEM in generating training data sets which consist of boundary voltage measurements accompanied by corresponding internal conductivity distribution is known. However, in pragmatic imaging scenarios, the internal conductivity distribution is unknown. Therefore, conductivity estimates must be obtained using an inverse methodology as described in the forthcoming sections.

3.1.3 Machine learning and neural network

As mentioned in the previous sections, solving an ill conditioned ERT inverse problem requires high computational cost. Herein, in order to reduce the overall computational costs of solving ERT inverse problems, this thesis explores the implementation of the Neural Networks (NNs) to solve ERT inverse problems directly considering different materials as well as using NNs to superresolve low-fidelity data. NNs are implemented with deep learning techniques which in most cases utilize gradient descent algorithms and back-propagation to minimise the error functions. Training of the NNs aims at reducing the discrepancies between the predicted values and the 'true' values. The weight and bias of each neuron are then saved during training which serves as a fundamental aspect in predicting the next output (Ying 2019). NNs are capable of solving both classification and regression problems, however the architectures and hyper-parameters of NNs are highly dependent on the patterns of which NNs are learning. In addition, the architectures and hyper-parameters of NNs are often adjusted with trial and error aiming at yielding the least prediction error. As a result, the calibration of architectures and hyper-parameters of NNs are often considered to be an "art" by machine learning engineers (LeCun, Bengio & Hinton 2015).

The concept and implementation of Neural Network was proposed in mid 20th Kröse et al. (1993) and research interests grew exponentially since the discovery of back-propagation and hardware development. Neural Network, in principle, aims to mimic the biological neuron process where raw data is passed on neurons (units) to produce an output. According to Papert Papert (1961), Neural Network learning algorithm is capable of learning any linear function from raw data. However, a multilayer network could offer the possibility of becoming

a deep learning network which leads to recognizing more complex representation especially in higher dimensional data. Currently Neural Network is implemented with Deep Learning aiming to solve difficult science, medical and business problems. For example, image classification, speech and document recognition, etc. LeCun et al. (2015).

In this project we will be using supervised machine learning where data set contains input and corresponding output are provided for the network to train. An objective function is formulated to compare the difference between predicted value and actual value which is called error during each epoch within training. During this training process, the parameters like the individual weights and bias of neurons will be adjusted leading to the steepest gradient descent in error space, aiming at approaching the pre-set threshold value for the objective function. Hence reach the possible minimum point in error space. Mostly, Stochastic Gradient Descent(SGD) algorithm is implemented during the training process for faster and more accurate approach.

There are different network architectures available targeting at solving and recognizing different patterns. A simple fully connected Artificial Neural Network (ANN) is effective at solving shallow classification tasks while Convolutional Neural Network (CNN) by embedding extra convolutional and max pooling layer are more powerful than conventional ANN hence are used for more complex recognition and classification tasks such as speech, text, handwriting image classification. Furthermore, Recurrent Neural Network (RNN) has also be the source of interest in recent years and by incorporating more adjustable parameters and dimensions this is a extremely powerful architecture that is mostly applied on markets prediction, society analysis, game playing AI, etc.

The motivation behind implementing NNs in this project is to utilize its capability of recognizing non-linear representation and to be more specific is to achieve direct inversion from measured voltages to electrical conductivity distribution hence to reconstruct the potential cracks. Since dependence between V and σ that we aimed to fit in this case is non-linear and by transforming ERT inverse problem to a binary classification task in NNS, their feasibilities

can be investigated.

3.1.4 Artificial Neural Network

As shown in [Figure 35](#) and mentioned in clause 2.3.1, we can observe the process of the

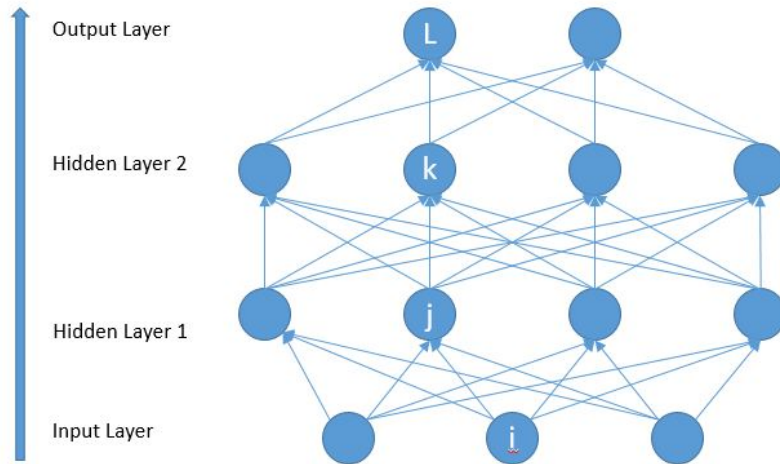


Figure 5: A typical ANN architecture with two hidden layers

data being passed on a typical ANN architecture which consists of an input, one or more hidden and one output layers as all units are connected to the upper and lower layer which describes a fully-connected network. Within each layer there are multiple neurons with their own weights and bias. Neuron output will also be passed on a threshold function/activation function to control the training. According to Lecun et al. LeCun et al. (2015) a two class classifier is capable of classifying two categories by separating half-space by a hyper plane which should be powerful enough for categorising two classes. According to Kröse et al. Kröse et al. (1993), more neurons will enable the network to adjust the weights towards desired hyperplane while filtering unhelpful information. This was demonstrated in CNN however should hold for ANN as well. Though this reviewing paper mainly illustrates examples in CNN, the content still could support the concept of this thesis. Although with the typical architecture shown in [Figure 36](#), the selection of the number of neurons and hidden layers remains as "art" especially with increasing depth of network. However the following paragraph provides certain tricks of achieving effective network structure.

Baum (1988) provided the proof of the simplest solution of a one layer neuron network of recognizing the desired function. It was discovered by Papert et al. (1961) that $N-1$ number of neurons in one hidden layer are capable of recognizing the arbitrary function of N points. Furthermore, as indicated by Cover (1965) a net with M weights has 50 percent probability of implementing a random function with $2(M + 1)$ vectors while the probability will infinitely approach 100% with increased weights and less vectors. Based on that Baum proposed that any net with one hidden layer with N/d neurons should be capable of realizing arbitrary function with set of N inputs with d dimensions. Discoveries mentioned in this paragraph should serve well as the lower bound or the least number of neurons and layers required to recognize the function in this project. If the example of arbitrary dichotomy is adapted into our problem Baum (1988), we can treat the positive points as positions of cracks while negative points be where the specimen is intact. The parallel line segment will serve the purpose of recognizing the potential function of voltage data and conductivity vector while separating the crack from the background in a binary manner. Hence the basic theory can support the aim of this thesis to treat the reconstruction inverse problem as a classification task in multilayer neural network aiming at finding the correlation between voltage experimental measurement as input and output which is the conductivity distribution derived from FEA model. By implementing the theories mentioned above, we can establish a starting point of constructing the network structure.

Furthermore Lecun et al. (2012) also offered some insights into achieving more accurate outputs. However before reviewing, note that any tricks mentioned is not a universal or ideal adjustment for any network, since problems are unique for instance the level of non-linearity for different patterns.

Firstly, instead of conventional batch learning we could try stochastic learning where a random sample is chosen at each epoch. Stochastic learning generally trains faster on large redundant samples since one batch of small sample is sufficient of descending the gradient. However the samples are chosen randomly in stochastic learning hence the learning curve is

noisy. Though with the obvious time cost advantage it is still extremely hard to quantify 'redundant' training samples in this case.

Secondly, training samples can be pre-processed to optimize the training process. If applying stochastic learning, we could shuffle samples to include different classes in excessive epoch since network learns faster in this way. To be specific, we could offer training samples which leads to larger errors in objective functions hence deliberately feeds the network with unexpected samples.

Thirdly, we could also normalize the training samples. By shifting the average of input to near zero, we could avoid the weights descending in a zigzag way for instance in a all positive training samples. Furthermore, training samples can also be scaled to have the same covariance as shown below which leads to faster convergence due to learning rates of neurons are more balanced.

$$C_i = \frac{1}{P} \sum_{p=1}^P (m_i^P)^2 \quad (9)$$

P represents the number of training samples, m_i^P represent the i^{th} component of the p^{th} training example. Also, since correlated inputs could keep the gradient on a straight line. If inputs are linearly correlated results unnecessary extra dimension will be created for network to learn. Hence decorrelate the input in advance would also speed up the training process.

Lecun et al. LeCun et al. (2012) also mentioned a typical sigmoid activation function to use which could potentially increase the convergence time however this is in conflict with Karlik et al. Karlik & Olgac (2011) and Glorot et al. Glorot et al. (2011) results where rectifier activation function is suggested. This aspect is discussed in detail in chapter 2.3.5.

3.1.5 Convolutional Neural Network

CNNs are a powerful NN architecture which take integrated information from raw data and feed them into a ANN mentioned above aiming at recognizing more features of the data hence solving more complex problems. Typically CNN is applied to image, handwriting recognition where image inputs are often involved. Images are incorporated to software in a matrix manner where black and white image as 2D matrix and coloured image as 3D image (RGB). Each entry within a matrix will be a real number between 0-255 represent the scale of each pixel where 0 represents black and 255 represents white. An CNN architecture generally includes five operation which are Convolutional Layer, Relu Activation Layer, Max Pooling, Flattening and ANN Wu (2017).

In the convolutional layers, a matrix is constructed named Feature Detector of which will be applied on the initial raw image matrix while moving along the whole space of the matrix. In each operation, dot product of each entries is taken and recorded to a new matrix which is called the Feature Map where the information are convolved as shown in [Figure 37](#). Entries in the feature map represents how close of each mini-matrix from input image is similar to the feature detector hence larger the number means a certain feature is extracted by the detector. Edge Detector for example is a common Feature Detector which only outlines the boundary of contents in the input image. During the training, different weights can be given to different feature detectors aiming to decide the essential ones hence resulting in group of feature maps which is called the convolutional layer shown in [Figure 38](#). By doing this operation we could significantly reduce the size of the problem as can be observed in [Figure 37](#) as well as preserving the most important features.

However by applying the feature detector we risk the potential chance of creating the linearity, hence we need to apply an extra ReLU layer to increase the non-linearity since most input images has highly non-linear features.

The third operation is Max Pooling. The main aim of max pooling is to introduce the spacial invariance into the network since in real practice a certain feature that is necessary

for recognizing might appear in different locations of the input image or be distorted to some extent, the network should still be able to pick that up. Hence a smaller size of matrix (2×2 in the example below) could be applied onto the convolutional layer where only the maximum number in the small matrix is extracted and recorded in a new matrix called Pooled Feature Map. An example of Max Pooling is shown in Figure 39. As we can observe that if number 5 changes its geographic location to top-right of the feature map, it will still be extracted and recorded in the pooled feature map which is also known as down sampling.

The fourth operation is to simply flatten the pooled feature map to a vector which will be regarded as the input layer of the following ANN. Hence the next operation will be a similar ANN architecture mentioned in clause 2.3.2 where the flattened vectors is trained.

One essential difference needs mentioning is that instead of using Mean Squared Error (MSE) function to calculate error during training, a cross-entropy function is preferred in CNN. A typical cross-entropy function is listed in equation (32), where p represents the real data while q is the predicted value. One of the main advantage of using cross-entropy loss function rather than MSE is that cross-entropy function could be pick up the improvement of the network if the predicted value is relatively much smaller than the actual value due to the logarithm operation in the equation.

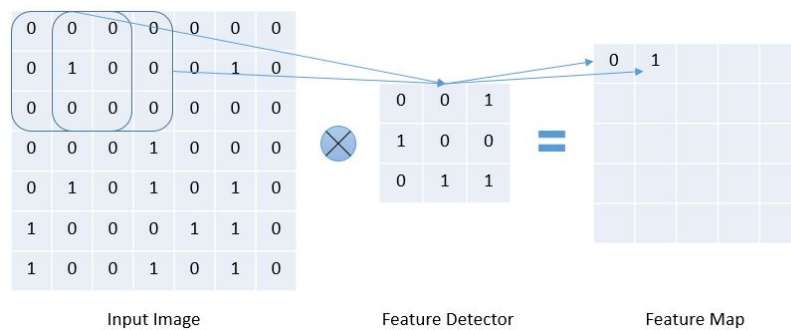


Figure 6: Feature detection operation of input image in CNN

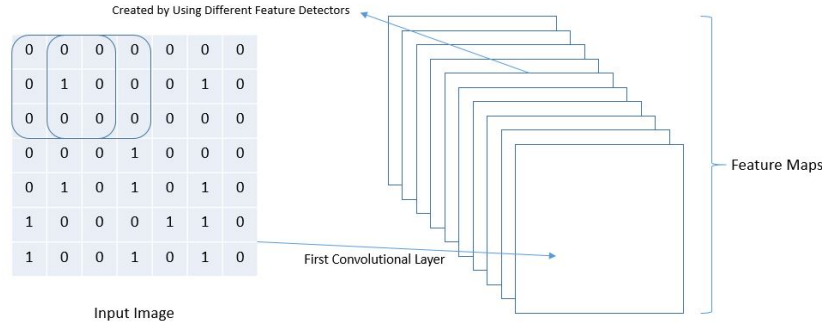


Figure 7: Construction of convolutional layer in CNN

Figure 8: Max pooling operation to construct pooled feature map in CNN

$$R(p, q) = - \sum_{x_1} p(x_1) \log q(x_1) \tag{10}$$

3.1.6 Activation Function

As mentioned in previous chapter, activation function serves within each neuron and acts as a valve which controls the output data which will be fed to the next hidden or output layer. Activation functions can be categorised to be binary step, linear and non-linear functions. According to different patterns and layer structures its essential that the most efficient activation function is chosen and tailored to the pattern.

A typical binary step function is shown as below where the input value is below or above the threshold value, this function will produce a binary outcome which is suitable for simple binary classification problems. However this will not be able to learn any non-linear patterns.

Any linear activation function could help recognizing a linear pattern but most likely the problems needs the implementation of Neural Network is highly non-linear.

Hence non-linear activation functions are the most common ones in NNs. Reviews were done on few conventional activation functions below with comments. Firstly, sigmoid function is one of the most popular due to its smoothness in transition while restraining the

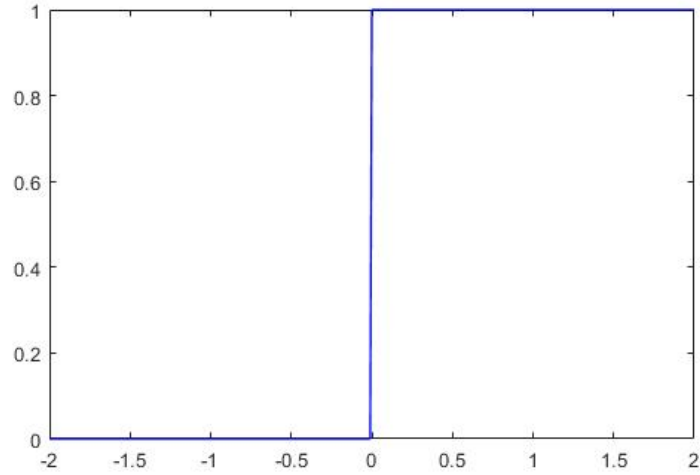


Figure 9: Plot of a typical binary step function giving output of 1 and 0 output value between finite value. This is consistent with Lecun’s suggestion of keep average of training samples around zero LeCun et al. (2012). Common sigmoid functions are Unipolar shown in equation (33) and Figure 41 and Bipolar equation (34) and Figure 42. According to Karlik Karlik & Olgac (2011), these two sigmoid functions is stretched along x-direction with upper and lower value hence is distinguishable which results in minimizing the computational cost.

$$g(t) = \frac{1}{1 + e^{-t}} \quad (11)$$

$$g(t) = \frac{1 - e^{-t}}{1 + e^{-t}} \quad (12)$$

Hyper Tangent Function is a similar function to sigmoid functions mentioned above however with much steeper gradient around zero whose equation is shown below. Typical plot is shown in Figure 43

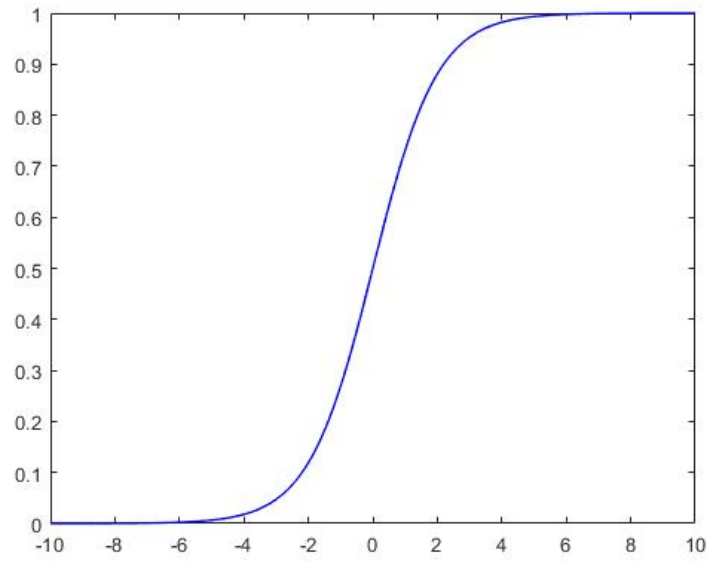


Figure 10: Plot of unipolar sigmoid function spanning between (0,1)

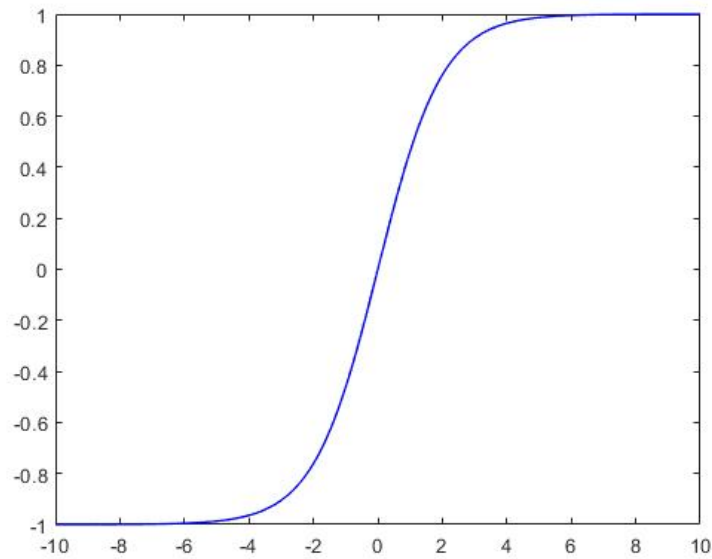


Figure 11: Plot of bipolar sigmoid function spanning between (-1,1)

$$g(t) = \frac{e^t - e^{-t}}{e^t + e^{-t}} \quad (13)$$

Performance analysis with 10 neurons and 40 neurons both shows Tanh activation function with minimum error and highest accuracy at 100 , 500 iterations respectively. However the

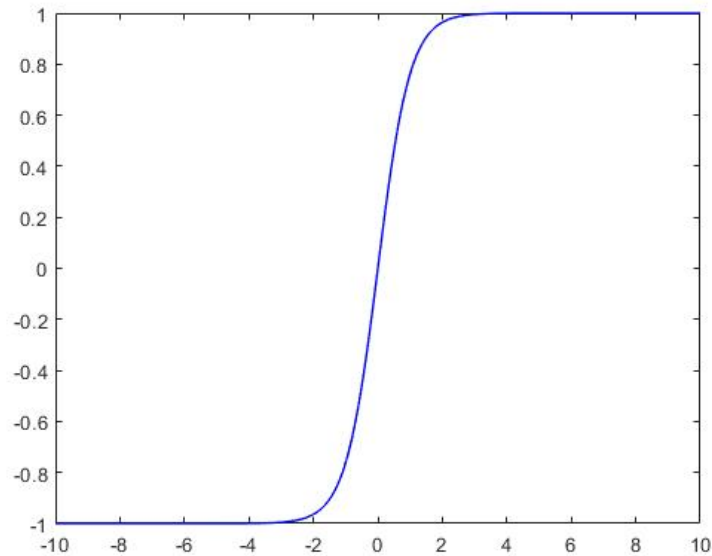


Figure 12: Plot of hyperbolic tangent function shows steeper gradient around origin simulation itself is not well presented in the paper, hence it is impossible to know what kind of problems the NN was trying to train on Karlik & Olgac (2011).

Another effective activation function is known as rectifier function (ReLU), typical plot is shown in [Figure 44](#) where the difference is the smoothness of transition. Rectifier function has the advantage of controlling specific neuron to be active while deactivate other neurons of which weights are low. Since mentioned in chapter 2.3.1, NN is merely trying to mimic the biological neuron process, according to Lennie Lennie (2003) only 1-4% of neurons are active at the same time which indicates the biological neuron process in a sparse way. Hence by deactivating certain neuron in NN mimics that feature well since certain number of neurons will not be contributing to the gradient decent during training process. Glorot et al. Glorot et al. (2011) also indicated that due to the one side nature of ReLU functions, matrices appearing during training process will be fairly sparse. The advantages of sparse matrices in neural network is firstly disentangle the information where small change in input value could be matched to the non-zero features Bengio (2009). Secondly it could also increase the chances of separating datasets in a linear manner. However too much sparse space could also lead to insufficient information being fed to NN which makes the training harder, hence this become a trade-off problem which need detailing implementation during practice.

There are also other different activation functions that can be chosen from freely hence

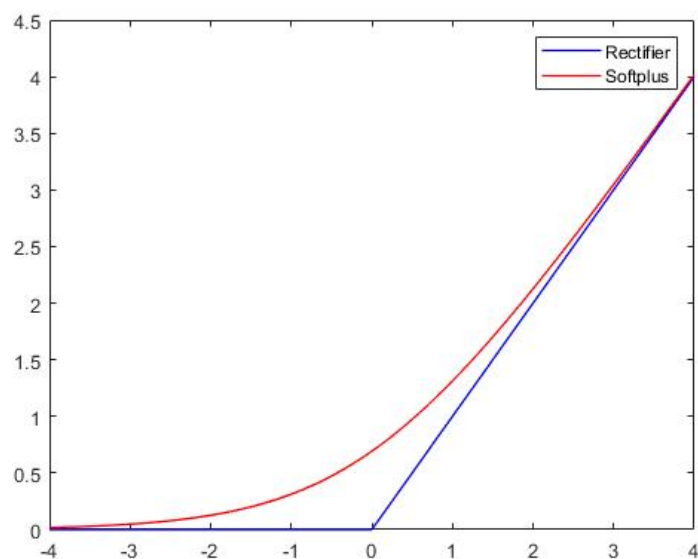


Figure 13: Plot of softplus and rectifier function shows their smooth transition difference for the clarity of this report, review was not done on each one of them and although there is no solid rule for selecting activation function, the best principle is to simply understand its aim as a function and tailor to the actual problem. (For example, is the output binary or can have infinite increasing range?).

3.1.7 Training of Neural Network

As mentioned in chapter 2.3.1, training process of NNs aims at finding the expected function between input and output. Hence generalization of the network will dominate the training performance. As described by Lecun et al. LeCun et al. (2012), bias and variance can be the representation of generalization for a certain network. Bias represents the average error of output from the desire function while variance is defined as the variance of output between datasets. Hence at the start of a training, bias should be high while variance remains low and when reaching the end of a training, bias should be minimal while variance remains appropriate since a high variance may be the indication that network is over-trained. A lost function is introduced here to quantify the training process. Though there are choices of such functions, a MSE function is the most common which is expressed below.

$$E^p = \frac{1}{2}(d^p - M(z^p, o))^2 \quad (14)$$

$M(z^p, w)$ represents the function while z^p stands for the p-th input, o represent all the parameter within the network. d^p represents the desired output in terms of the p-th function. Hence E^p represents the MSE of the whole network and aim of our training will be to minimize E^p . During training, weightings of each neuron will be adjusted through back propagation and gradient decent which will be discussed in detail in 2.3.6 along with other learning algorithm. By adjusting the weighting on different neurons network has the possibility to minimize the loss function until it converges to minimal. If consider data passing from neuron β to γ , we can describe this process in a mathematical form as below.

$$y_\gamma = F_\gamma(w_{\beta\gamma}, y_\beta) \quad (15)$$

y_β and y_γ represents the output value from neuron β and γ , $w_{\beta\gamma}$ represents the weighting of γ from β . F_γ represents the activation function at neuron γ . For future convenience we could call the weighting matrix at iterative t as $S_\gamma(t)$ and expressed as below

$$S_\gamma(t) = \sum_{\beta} w_{\beta\gamma}(t)y_\beta(t) + \theta_\gamma(t) \quad (16)$$

$\theta(t)$ represents the bias of the network which can be seen as an extra linear term. Hence substituting to equation (37) we can have the following expression in terms of the activation function.

$$y_\gamma(t + 1) = F_\gamma\left(\sum_{\beta} w_{\beta\gamma}(t)y_\beta(t) + \theta_\gamma(t)\right) \quad (17)$$

Equation (39) forms the basic mechanism about how information are passed from one neuron to one another.

3.1.8 Back-propagation

In this section, the mathematical mechanism of back-propagation will be explained along with the other developments. Main aim of implementing back-propagation is to further minimize the error function by adjusting corresponding weights following the reversed direction. Hence it is essential for the algorithm to locate the minimum of the weight space. For example, a sagging point for a 2D problem. However since the complex dimensionality of this project, we require more solid expression of how back-propagating works. Explained by Rumelhart, Hinton and Williams Rumelhart et al. (1986), in order to find the minimal point at weight space using gradient decent, partial derivative of the error function with respect to each weights in the network needs to be computed.

Two phases are required before the back-propagation which combined can be seen as the whole forward propagation process. An simple sigmoid function is chosen an expressed as below

$$y_\gamma = \frac{1}{1 + e^{-x_\gamma}} \quad (18)$$

x_γ represents the input of neuron γ and training sample is passed on equation (40) to become the output y_γ .

$$x_\gamma = \sum_{\eta} y_\eta w_{\gamma\eta} \quad (19)$$

$w_{\gamma\eta}$ represents the weight of neuron η to neuron γ . It is simply a linear summation of multiplication of each weights. In this case bias of neuron was ignored for convenience of explanation. Furthermore we can simplify equation (36) by leaving out the mean square error feature.

$$E = \frac{1}{2} \sum_l \sum_{\gamma} (y_{\gamma,l} - d_{\gamma,l})^2 \quad (20)$$

l represents a certain training sample, while γ is an output neuron. $y_{\gamma,l}$ represents the training output of neuron γ from training sample l while $d_{\gamma,l}$ stands for the desired output. The halved and squared form is providing mathematical convenience. By computing equation (40-42), the forward propagating process is finished hence in order to keep gradient descenting in back-propagation, partial derivative of E with respect to weights needs to be computed. If only one training sample is considered hence ignore l in equation (42) and take its partial derivative with respect to y_{γ} , we have

$$\frac{\partial E}{\partial y_{\gamma}} = y_{\gamma} - d_{\gamma} \quad (21)$$

Then further pushing process backwards, we can compute the form of partial derivative with respect to the input of neuron γ .

$$\frac{\partial E}{\partial x_{\gamma}} = \frac{\partial E}{\partial y_{\gamma}} \frac{dy_{\gamma}}{dx_{\gamma}} \quad (22)$$

By differentiating equation (40) , we could have

$$\frac{dy_\gamma}{dx_\gamma} = y_\gamma(1 - y_\gamma) \quad (23)$$

By substituting equation (45) to equation (44), we could have

$$\frac{\partial E}{\partial x_\gamma} = \frac{\partial E}{\partial y_\gamma} y_\gamma(1 - y_\gamma) \quad (24)$$

Furthermore the link between weights and error function needs to be computed as following

$$\frac{\partial E}{\partial w_{\gamma\eta}} = \frac{\partial E}{\partial x_\gamma} \frac{\partial x_\gamma}{\partial w_{\gamma\eta}} \quad (25)$$

By differentiating equation (41) with respect to $w_{\gamma\eta}$ we would have y_η while substituting to equation (47) we have following:

$$\frac{\partial E}{\partial w_{\gamma\eta}} = \frac{\partial E}{\partial x_\gamma} y_\eta \quad (26)$$

Equation (48) gives the possibility of computing relationship of partial derivative of E and weight which passes data from neuron η to γ and its previous neuron output. Hence by differentiating equation (41) with respect to y_η we obtain:

$$\frac{\partial E}{\partial x_\gamma} \frac{\partial x_\gamma}{\partial y_\eta} = \frac{\partial E}{\partial x_\gamma} w_{\gamma\eta} \quad (27)$$

From equation (49) we have:

$$\frac{\partial E}{\partial y_\eta} = \frac{\partial E}{\partial x_\gamma} w_{\gamma\eta} \quad (28)$$

Equation (48) and (49) shows the process of back propagation of the output value of neuron γ to input and its weighting from previous neuron. By following equation (48) and (49), we could properly back propagating and compute $\frac{\partial E}{\partial w}$ along the way. Both Rumelhart et al. (1986) and Lecun et al. (2012) have proposed and explained the ways of updating weights in back propagation with further analysis linked to practical training tricks. Firstly two ways of updating weights proposed by Rumelhart et al. (1986) is introduced and followed by Lecun's LeCun et al. (2012) analysis on its practical applications. First way to update the weights is to compute $\frac{\partial E}{\partial w}$ for each training sample which is close to the definition of Lecun's stochastic learning, and the second way is to accumulate computation of $\frac{\partial E}{\partial w}$ for all training samples before updating the weights. Lecun stated that firstly stochastic learning is quicker than batch learning in most case due to its noisy decent nature and secondly as for the same reason, stochastic learning may lead to better results since it has more possibility to jump in deep localised minima basin in weight space. Thirdly, Lecun indicated a faster convergence speed with redundant training sample, however logic behind this point is solid, it is not a practical finding since all training samples are made to be as random as possible. A common way of adjusting the weight is as following:

$$\Delta w = -\varepsilon \frac{\partial E}{\partial w} \quad (29)$$

where ε is a scalar which determine the learning rate, equation (51) can also be improved by adding an simple terms such as following:

$$\Delta w(t) = -\varepsilon \frac{\partial E}{\partial w(t)} + \zeta \Delta w(t-1) \quad (30)$$

where ζ is an exponential decay factor between 0 and 1, while t represents the number of epoch Rumelhart et al. (1986). According to Rumelhart, this could more accurately and quickly adjust the descending speed and direction of the point in weight space rather than its position only. Although Rumelhart lacks further exploration with the updating factor, Lecun gave more analysis in terms of the updating of weights.

According to Lecun ε is only considered as a scalar constant in the simplest scenario. Implementing more complex updating methods, ε may be treated as a variable or an estimation of the cost function's inverse Hessian matrix. Choosing of ε will have a great impact on gradient descent hence the whole training process.

This is a publication based thesis and I firstly introduce the aims of this thesis followed by the connections between three publications as well as my contribution to these papers. I then present the contents of these publications and finalize the thesis in the conclusion section.

3.2 Aim of the thesis

The primary aim of this thesis is as following: 1) conduct feasibility studies on solving ERT inverse problems directly with deep learned ERT frameworks and 2) reduce the computational costs of obtaining numerical solutions from low-fidelity data. Since SHM methodologies are widely applied in civil and aerospace industry, I aim to explore the feasibility of implementing the proposed deep learned ERT frameworks in both fields. As a result, I set up the secondary aims as following: 1) conduct the feasibility study of the proposed deep learned ERT frameworks on detecting cracks considering cement-based materials, 2) explore the feasibility of the proposed deep learned ERT frameworks on monitoring structural status considering aerospace materials under loadings and finally 3) explore the feasibility of using NNs to potentially superresolve low-fidelity data. The connections between these aims are presented in the following section.

3.3 Connections between the published papers

In this section the research connections behind the three publications are presented. I firstly utilized the NNs to replace the computational expensive algorithms for solving ERT inverse problems and secondly validated the deep learned framework using experimental and simulation data considering cement-based material. This research showed the potential of using NNs to predict the probabilistic location/sizing of the cracks, however this approach did not offer the reconstruction of the global strain/stress fields in the domain. As a result, this study can only offer reconstructions when local cracks have already occurred. The work associated with the above is shown in Section *Probabilistic Cracking Prediction via Deep Learned Electrical Tomography*. For SHM purposes, it might be more insightful if the proposed deep learned framework can offer reconstructions of the real-time strain/stress fields. In the following paper, as a continuation of the prior work, I utilized a function that maps the internal conductivity distribution to strain/stress field has been developed and studied on nanocomposites by utilizing their piezoresistive properties. Such a function is known as a piezoresistivity model, which enables researchers to develop self-sensing frameworks on nanocomposites (Tallman, Gungor, Wang & Bakis 2015, Thomas, Kim, Tallman & Bakis 2019, Gallo & Thostenson 2016, 2015, Baltopoulos, Polydorides, Pambaguian, Vavouliotis & Kostopoulos 2015, Tallman & Smyl 2020). Since nanocomposites are applied in aerospace engineering, it is reasonable to conduct further research in applying the proposed deep learned ERT framework in imaging strain/stress distributions. The detailed work associated with this is provided in Section *Predicting strain and stress fields in self-sensing nanocomposites using deep learned electrical tomography*.

By using NNs to directly solve ERT inverse problems, I can significantly reduce the computational costs, however, in pragmatic applications, the computational processing power can occasionally be limited due to various reasons. Herein, one can reduce the computational cost if numerical solutions can be obtained with low-fidelity data which often have less entries. I proposed to explore the feasibility of data-driven superresolution applications using NNs and validated them on FEM simulation studies as well as on upsampling experimental ERT voltage measurements. Work associated with superresolution is presented in Section

Data-driven superresolution of numerical simulations and experimental measurements. By following the research logic mentioned above, the first two paper has been published while the final paper has been submitted subjected to further review.

3.4 Contribution to the publications

In this section, I list out my contribution concisely in terms of the three publications included in this thesis. It is worth commenting that then literature review has been excluded from this section. For more detailed literature review conducted for the relevant studies, readers should refer to the corresponding sections.

Paper One:

1. I integrated the FEM and the complete electric model (CEM) based on the experimental domain for simulating flexural cracks.
2. A similar integrated model was then established on an discretized domain for simulating shear cracks;
3. Then, I programmed both models to simulate the progression of the cracks on both discretized FEM domains.
4. In addition, further programmings were done for the two integrated models to generate sufficient number of training samples for the NNs.
5. After that, the training samples were reformatted to binary vectors where zeros were assigned to the background and ones were assigned to the crack locations.
6. Then, a fully connected NN was then constructed to solve the ERT inverse problems directly aiming at reconstructing the probabilistic of the flexural crack locations. A convolutional NN was then established aiming at reconstructing the probabilistic of the shear crack locations.
7. Architectures and hyper-parameters of both networks were repeatably adjusted based on validation performances against simulation and experimental results.

8. Finally the results were compiled in the paper along with the discussions.
9. D.S was involved in formulation of overarching research goals and aims, helped with the overall data analysis as well as the critical review, commentary and revision at pre-publication stages. D.S also offered oversight and leadership responsibility for the research activity planning and execution. S.S.H and D.L helped with the analyzing of the obtained data as well as the revision at pre-publication stages. G.A helped conceptualization with the revision at pre-publication stages.

Paper Two:

1. I firstly established an integrated model consists of CEM, Piezoresistivity model and FEM which mapped the boundary voltage measurements to strain/stress fields on nanocomposites.
2. After that, the integrated model was then programmed to generate sufficient number of training samples for the NNs.
3. Then, training samples were then pre-processed ahead of training to reduce the modelling error as well as increasing the variance of the training data.
4. In addition, two fully connected NNs were then established aiming at reconstructing strain and stress fields respectively.
5. Architectures and hyper-parameters of both networks were then adjusted based on validation performances against simulation and experimental results.
6. In addition, predicted strain and stress fields were then compared with the experimental digital image correlation (DIC) images.
7. Finally, results were compiled in the paper with the discussions.
8. D.S was involved in formulation of overarching research goals and aims, helped with the overall data analysis as well as the critical review, commentary and revision at pre-publication stages. D.S and TN.N also offered oversight and leadership responsibility

for the research activity planning and execution. TN.N and H.H provided the previous research output regarding self-sensing nanocomposites. S.S.H helped with the analyzing of the obtained data as well as the revision at pre-publication stages.

Paper Three:

1. I firstly established two FEMs meshed with lower and higher order elements respectively for the mechanical simulations studies.
2. These two FEMs were then programmed to generate numbers of training samples consist of displacement vectors;
3. Then, two fully connected NNs were developed to superresolute the displacement vectors computed from FEM with lower order elements on x and y directions respectively. Random simulation results were then selected to validate this approach.
4. In addition, I adapted the domain of an experimental ERT inverse problem. An integrated model with FEM and CEM was then established based on the experimental domain and then programmed to generate high fidelity boundary voltage measurements based on 16 electrodes which were then down-sampled to measurements based on 8 electrodes.
5. After that, a fully connected NN was developed to learn the mapping between the low-fidelity and high-fidelity voltage measurements.
6. After the training, the ERT inverse problem was solved using the conventional Total Variation (TV) prior regularization algorithm.
7. In the end, the superresolution results were compared with reconstructions from low and high fidelity data and the paper was finalized by discussions.
8. D.S was involved in formulation of overarching research goals and aims, helped with the overall data analysis as well as the critical review, commentary and revision at pre-publication stages. D.S also offered oversight and leadership responsibility for the research activity planning and execution. S.S.H and D.L helped with the analyzing of the obtained data as well as the revision at pre-publication stages.

4 Novelty of the publications

In this section, I will briefly list the novelty of the following three publications. In Paper One, I utilized neural networks to directly solve the ERT inverse problem to offer probabilistic binary cracking predictions on cement-based materials. Feed-forward neural networks and convolutional neural networks were used to study the feasibility of this deep-learning approach for both flexural and shear cracks. In Paper Two, I developed a deep-learning framework with neural networks to directly reconstruct the strain and stress distribution on nanocomposites. This proposed work can significantly reduce the computational time compared to conventional algorithms, which could reduce lag in data processing when used in practical applications. In Paper Three, I explored the feasibility of a superresolution approach that could potentially map low-fidelity data to high-fidelity data. A mechanical simulation study and an ERT inversion experimental study were used for the feasibility study. These research outputs could potentially allow for on-site data processing with reduced computational requirements.

5 Probabilistic Cracking Prediction via Deep Learned Electrical Tomography

Authorship: Liang Chen, Adrien Gallet, Shan-Shan Huang, Dong Liu and Danny Smyl

Published Journal: Structural Health Monitoring Volume 21, Issue 4

DOI: <https://orcid.org/0000-0002-9645-7683>

5.1 Abstract

In recent years, Electrical Tomography, namely Electrical Resistance Tomography (ERT), has emerged as a viable approach to detecting, localizing and reconstructing structural cracking patterns in concrete structures. High-fidelity ERT reconstructions, however, often require computationally-expensive optimization regimes and complex constraining and regularization schemes, which impedes pragmatic implementation in Structural Health Monitoring frameworks. To address this challenge, this paper proposes the use of predictive deep Neural Networks to directly and rapidly solve an analogous ERT inverse problem. Specifically, the use of cross-entropy loss is used in optimizing networks forming a nonlinear mapping from ERT voltage measurements to binary probabilistic spatial crack distributions (cracked/not cracked). In this effort, Artificial Neural Networks and Convolutional Neural Networks are first trained using simulated electrical data. Following, the feasibility of the predictive networks is tested and affirmed using experimental and simulated data considering flexural and shear cracking patterns observed from reinforced concrete elements.

5.2 Introduction

5.2.1 Background

Structural health monitoring (SHM), in a broad sense, aims to assess the integrity, condition and/or damage state of target structures (Balageas, Fritzen & Güemes 2010). Respectively, SHM frameworks have proposed clear hierarchies including, for example, aspects such as detection, localization, classification, assessment, and prediction which serve as facets for monitoring (Farrar & Worden 2012). For such hierarchies to be satisfied, SHM modalities should therefore include systematic, automatic and continuous data acquisition followed by accurate post-processing and analysis. To address the latter needs, specifically rapid and accurate damage assessment of structural concrete elements, this work focuses on rapid probabilistic crack prediction and localization enabled by machine learned models.

Prediction and localization of cracking in concrete elements is well documented in the field of non-destructive testing (NDT) literature. Various traditional approaches include ultrasonic, magnetic, electromagnetic, radiographic, photographic, and infrared modalities (Gholizadeh 2016, Mutlib, Baharom, El-Shafie & Nuawi 2016, Montinaro, Cerniglia & Pitarresi 2018, Kong & Li 2018, Ma & Li 2018). In contrast to these well-established methods, electrical-based modalities have recently shown promise in non-destructive testing and evaluation of cement-based materials and structures (Smyl 2020). For example, in their seminal work, Karhunen et al. (Karhunen, Seppänen, Lehikoinen, Monteiro & Kaipio 2010) demonstrated industrial applicability of electrical modalities for assessing the degree of cracking, localization of reinforcement, corrosion state and depth of the cover in concrete elements. Additionally, previous studies have shown that electric impedance spectroscopy (EIS) is relatively inexpensive and can be applied on concrete elements to detect cracks to include their width/depth, reinforcement, and internal moisture (Pour-Ghaz, Niemuth & Weiss 2013, McCarter & Garvin 1989). On the other hand, Electrical Tomography, more specifically Electrical Resistance Tomography (ERT, a specific Electrical Tomography modality), has been recently demonstrated as an effective modality for detecting simple and complex cracking patterns in concrete elements (Karhunen, Seppänen, Lehikoinen, Monteiro & Kaipio 2010, Zhou, Bhat, Ouyang & Yu 2017, Smyl, Pour-Ghaz & Seppänen 2018, Shi, Lu & Guan 2019); meanwhile, ERT has low

experimental costs, energy consumption, fast data collection, high temporal resolution and potential of continuous spatial monitoring (Liu, Smyl & Du 2020). However, the potential disadvantages of ERT include its lower spatial resolution compared with other contemporary modalities and (traditionally) high computational cost (Smyl, Bossuyt, Ahmad, Vavilov & Liu 2020).

In assessing the former realizations regarding ERT, relatively low spatial resolution may be sufficient in terms of localizing cracks – especially in large members (Rashetnia, Alla, Gonzalez-Berrios, Seppanen & Pour-Ghaz 2018). Furthermore, the high computational cost that traditionally arises in ERT stems from solving the ill-posed inverse problem. Though previous research has demonstrated that incorporating non-iterative reconstruction methods can reduce the computational time at a significant cost to spatial resolution (often overly smooth), computational demand and interpretability of reconstructions remain factors inhibiting implementation of ERT in field applications. As such, a new methodology promoting rapid and accurate cracking prediction from ERT data sets is needed. To address this issue, the following paper proposes and investigates the implementation of Neural Networks (NN) to directly solve an analogous ERT inverse problem affording (a) massive reduction in computing demand and prediction time relative to high-fidelity ERT reconstruction frameworks and (b) improved interpretability of (predicted) cracking patterns.

5.2.2 Machine learning and damage prediction

The concept of using NNs for pattern recognition and parameter space mapping originated in mid-20th century (Kröse, Krose, van der Smagt & Smagt 1993) and has drawn large research interest since the discovery of back-propagation while computational power has been increasing exponentially. In fact, previous studies have indicated that a well-trained network with two neurons is sufficient to recognize any linear functions between the input and output data sets theoretically (Papert 1961). However, realistically, a deeper network with non-linear activation functions is required to predict more complex representations (Papert 1961). For this reason, we investigate the use of supervised deep learned NNs for mapping input data to desired output parameters, as detailed in the following.

Feed-forward Artificial Neural Networks (ANNs) have architectures consisting of at least one hidden and one output layer. In a pioneering work, Baum (Baum 1988) proved that a simple one-layer network can recognize a linear pattern. Following, work by Papert et al (Papert 1961) discovered that an ANN network with $N - 1$ neurons should be sufficient to learn an arbitrary function with N data points. Subsequent early research also indicated that networks having $M \ll N - 1$ weights has approximately 50% probability of successfully predicting a random function (Bishop et al. 1995). Later, Lecun et al. (LeCun, Bengio & Hinton 2015) identified that a well trained binary classifier is capable of linearly separating the error space by a hyper-plane. This enabling feature is key in the ability of NNs to recognize highly non-linear patterns. However, despite tremendous research progress in ANN research, tailoring ANN parameterizations still remains an “art” in practice.

In contrast to ANNs, Convolutional Neural Networks (CNNs) are NN architectures first trained with back-propagation by Lecun et al. and inspired by human ventral visual stream (LeCun, Boser, Denker, Henderson, Howard, Hubbard & Jackel 1989, Luo, Roads & Love 2021). CNNs are widely used for handwriting, image, and voice classification – along with other recognition applications (LeCun, Bengio et al. 1995). A typical CNN’s functionality depends on four basic layers which are input layer, convolutional layer, pooling layer and fully-connected layer (O’Shea & Nash 2015). Firstly, in the input layer, CNNs take input information via an image matrix where (broadly speaking) each entry is either a continuous entry or assigned a whole number varying from 0 – 255 representing the scale of each pixel from black to white. Secondly, within the convolutional layers, learnable kernels are glided through the raw input while the scalar products are calculated for each entries in the kernels, the output of this convolution operation are referred as feature maps. Each kernel has its corresponding feature map which is stacked along the depth of the input (Goodfellow, Bengio, Courville & Bengio 2016). Kernels can help the network to extract more characteristic information from input data (O’Shea & Nash 2015). The convolution operation is mainly governed by the following three hyperparameters: 1. depth of the convolutional layer, 2. stride of the kernels and 3. padding (Albawi, Mohammed & Al-Zawi 2017). Reducing the depth of the convolutional layers can lead to a significant decrease in network’s recognition

capability. Meanwhile, stride controls the overlap when kernels are glided through the input data, by reducing the stride, one can reduce the output volumes however at the risk of missing potential features. In addition, the use of zero padding ensures that features at the extents of the image input can be efficiently extracted. Furthermore, parameter sharing can be used to reduce the number of parameters in the network by constraining the learned feature maps to have the same weight and bias (O’Shea & Nash 2015). Thirdly, a pooling layer aims to further down-sample convolved data. For example, a max-pooling layer is applied on the feature maps and only returns the maximum value within the region. Finally, data are propagated to a fully-connected layer which has a similar structure to a typical ANN. Of importance here, the inputs of the (first) fully-connected layer are the outputs of the last pooling layer which are subsequently propagated through the remaining fully-connected layers during the training (Goodfellow, Bengio, Courville & Bengio 2016).

Specifically, we are interested in direct classification of spatially-distributed damage (cracking) which is assigned a binary form (0 or 1). As such, the use of probabilistic cross-entropy classification is most appropriate given the binary nature of the information to be mapped (i.e. classical regression is not appropriate). Therefore, we select the binary cross-entropy function as the loss functional to be minimized in the network training, written as follows

$$\mathcal{L} = -\frac{1}{N} \sum_{t=1}^N [y_t \log(p_t) + (1 - y_t) \log(1 - p_t)]. \quad (31)$$

In Equation (31), \mathcal{L} represents the binary cross-entropy loss taking predictions p_t and binary sample labels y_t across $t \in N$ training samples (Saxe & Berlin 2015). The interpretation of minimizing Equation (31), in the learning process, may be viewed as gradually improving the probability \mathbf{P} that predictions p_t match the true distributions y_t . As it pertains to this work, this corresponds to learning the underlying patterns governing the predictions of cracks where, using relaxed notation, $\mathbf{P} = 1$ and $\mathbf{P} = 0$ respectively correspond to cracked and not cracked locally. Pragmatically speaking, however, minimizing Equation (31) may lead to over-fitting and reduced generalizability. Therefore, L_2 regularization is herein utilized to address the former by writing

$$\mathcal{L} = -\frac{1}{N} \sum_{t=1}^N [y_t \log(p_t) + (1 - y_t) \log(1 - p_t)] + \lambda \|w\|^2 \quad (32)$$

where λ is a scalar regularization hyperparameter and w are the network weights.

Generally speaking (and herein), Equation (32) is minimized by implementing gradient descent and back-propagation via locating the minimum point within the loss space. It is worth noting that, despite developments of, e.g. the Hopfield Network and Boltzmen Machine which offer new insight of training networks with statistical mechanics (Hopfield 1982, Ackley, Hinton & Sejnowski 1985), many modern networks still rely on gradient descent and back-propagation. Moreover, while local minima can be reached by adjusting the weights of individual neurons in the network iteratively, there exist studies indicating a global minimum could be attained providing a deep neural network with non-convex objective function (Du, Lee, Li, Wang & Zhai 2019), although the evidence supporting that is not substantial. Therefore, for the purposes of this initial work, a local minimum can be assumed to yield results deemed sufficient for the purposes of damage detection.

It is worth highlighting that, in the context of contemporary SHM research, machine learning has been successfully used in damage detection applications. For example, Bao et al. (Bao, Guo & Li 2020) utilized neural networks for optimization considering non-convex sparse time-frequency analysis and consequently achieved more accurate instantaneous frequency identification. Moreover, Mousavi et al. (Mousavi, Varahram, Ettefagh, Sadeghi & Razavi 2020) trained deep neural networks to extract damage-sensitive features from vibration data. In addition, Convolutional Neural Networks were also explored to retrieve missing strain data due to sensor fault by Oh et al. (Oh, Glisic, Kim & Park 2020) while Mohtasham used CNNs to detect cracks on gas turbines with filtered figures/paper3 (Mohtasham Khani, Vahidnia, Ghasemzadeh, Ozturk, Yuvalaklioglu, Akin & Ure 2020). Inspired by such works, in this paper, neural networks are also utilized for the intended purposes of SHM.

5.2.3 Paper structure

This paper first reviews the historical development and application of ERT as well as a conventional solution to the ill-posed ERT problem. Then, the deep learned direct inversion

framework is proposed. Thereafter, the data acquisition and training methodology consisting of the training data generation, neural network architecture as well as the training process are detailed. Following, predictive results for experimental and simulated crack patterns are reported and discussed considering both their advantages and drawbacks. Lastly, conclusions are provided.

5.3 Electrical Resistance Tomography and Direct Inversion

ERT is a modality which aims to reconstruct internal conductivity distributions from boundary electrode measurement. To achieve this, a prescribed number of electrodes are installed on the boundary of the specimen, from which electrode potentials are measured and electric currents are injected into. Resultingly, potential differences are taken between one pair of electrodes for each injection. As a whole, the measurement protocol should be planned in a systematic manner to ensure sufficient data can be collected during each injection.

Historically speaking, ERT was initially developed and utilised for medical imaging by classifying organs based their different conductivities (Henderson & Webster 1978), later considering capacitive and inductive tomographies (Yang & York 1999). In the recent years, ERT has been the source of significant research interest in the NDT/SHM community. For this, ERT has been coupled with sensing skins to detect damage in reinforced concrete (Hallaji, Seppänen & Pour-Ghaz 2014, Smyl, Pour-Ghaz & Seppänen 2018, Smyl & Liu 2019*a*) as well as imaging damage, strain and stress fields in a broad suite of composite materials (Loh, Kim, Lynch, Kam & Kotov 2007, Loh, Hou, Lynch & Kotov 2009, Loyola, Briggs, Arronche, Loh, La Saponara, O'Bryan & Skinner 2013, Lestari, Pinto, La Saponara, Yasui & Loh 2016, Tallman, Gungor, Koo & Bakis 2017, Tallman, Gungor, Wang & Bakis 2014, Tallman & Smyl 2020, Hassan & Tallman 2020*b*). Previous related studies also demonstrate that ERT is capable of imaging internal moisture flow within cement-based material in both 2D and 3D settings (Hallaji, Seppänen & Pour-Ghaz 2015, Smyl 2020).

Until recently, high-fidelity solutions to the ERT reconstruction problem have generally required solving an optimization problem using conventional iterative regularized computational methods (readers are referred to (Smyl, Bossuyt, Ahmad, Vavilov & Liu 2020) for a

comprehensive review of ERT inversion methods used in NDT). However, as earlier alluded to, such methods can be demanding and pragmatically inhibiting. On the other hand, linearized difference imaging schemes offer much faster solutions at the cost of spatial resolution (Liu, Smyl, Gu & Du 2020a). As such, we herein take a different approach to the ERT inversion problem by utilizing direct inversion enabled by trained NNs in order to attain rapid high fidelity predictions. Related work has, e.g. aimed at using NNs for solving the continuous ERT problem (Fan & Ying 2020). Additional research has shown that CNNs are capable of reconstructing ERT figures (Tan, Lv, Dong & Takei 2018, Hamilton & Hauptmann 2018) however not for detecting cracking in structural applications. Recently, researchers in (Smyl & Liu 2020) also used NNs to optimize the electrode locations in ERT measurement aiming at achieving more efficient data acquisition. In the following section, written for contextualization, we will first discuss the forward problem underlying ERT physics (and used for generating training data), then discuss the conventional ERT inverse problem, and finally propose the analogous ERT direct inversion framework.

5.3.1 The ERT inverse problem

The traditional nonlinear ERT inverse problem can be conceptually characterized by the following observation model

$$V = U(\sigma) \tag{33}$$

where U is the finite element forward model mapping σ to measured voltages V . Such a model implies that when the measurements and the forward model match exactly, the inverse problem is solved (i.e. when the L_2 norm of the data fidelity term is minimized: $\|V - U(\sigma)\|^2 = 0$). In reality, however, such a case is an unrealistic idealization as measurement noise e is always present, resulting in the noise-modified observation model written as

$$V = U(\sigma) + e. \tag{34}$$

Unfortunately, due to the presence of noise, numerical modelling error, nonlinearity of $U(\sigma)$, and ill-conditioning of resulting ERT matrices used in solving the inverse optimization problem, there are infinite solutions to Equation 75. Thus, we require advanced regularization to incorporate biasing prior information and, often, physical constraints in optimizing/solving the nonlinear (absolute imaging) inverse problem. In order to avoid such complexities, the observation model may be linearized in order to obtain solutions with less up-front computational demand/complexity (Liu, Smyl & Du 2019).

Linearized ERT, or simply difference imaging as we will herein refer to it, is a framework which aims to reconstruct the difference of internal conductivity $\Delta\sigma$ based on differences of boundary voltage measurements ΔV from two different states (subscripts 1 and 2 representing *baseline* and *damaged* states, respectively) expressed in the following

$$\Delta V = V_2 - V_1 \tag{35}$$

$$\Delta\sigma = \sigma_2 - \sigma_1. \tag{36}$$

As a consequence, the following linearized observation model can be written

$$\Delta V = J\Delta\sigma + \Delta e \tag{37}$$

where $J = \frac{\partial U(\sigma_1)}{\partial \sigma_1}$ is the Jacobian matrix computed at the linearization point σ_1 and Δe is the difference in measurement noise between states 1 and 2.

Based on the observation model in Equation 76, the ERT reconstruction problem is generally facilitated by a one-step least squares solution minimizing the following objective function

$$\Delta\hat{\sigma} = \|L_{\Delta e}(\Delta V - J\Delta\sigma)\|^2 + \alpha\|L_R\Delta\sigma\|^2 \tag{38}$$

where $L_{\Delta e}$ and L_R are Cholesky factorized noise weighting and regularization matrices, respectively. The use of regularization, the magnitude of which is largely controlled by the hyperparameter $\alpha > 0$, is required to stabilize solutions and incorporate prior information into the least squares minimizer described below

$$\Delta\hat{\sigma} = (J^T W J + \alpha L_R^T L_R)^{-1} J^T W \Delta V \quad (39)$$

where W is a diagonal noise weighting matrix.

The advantages in adopting linearized schemes, such as the difference imaging approach described previously, are numerous. Firstly, since one-step optimization is used, inverse solutions are significantly less computationally demanding than nonlinear absolute imaging solutions. Secondly, and of principal importance to this work, the use of difference data ΔV results in subtraction of systematic errors. Therefore, in cases where measurements are simulated for use in training data, a significant portion of modelling errors are subtracted – thereby reducing the influence of modelling error corruption in training. In the following subsection, we will detail the incorporation of difference data into the learned direct inversion scheme analogous to the traditional linearized scheme previously described.

5.4 Training Data Acquisition and Training Methodology

5.4.1 Overview

Training data was generated using the CEM equipped with quadratic triangular discretizations. A set of training samples herein consists of simulated electrode potential differences generated using sampled conductivity distributions and complimentary binary crack distributions described in the previous subsection. Regarding the potential measurements more specifically, each simulated difference measurement set results from subtracting baseline (undamaged) ERT measurements V_1 from ERT measurements V_2 generated from a cracked configuration.

In this work, two cracking phenomena are studied: flexure-induced cracking and shear-induced cracking. In total, 40,000 sets of training samples were generated for both flexural

and shear cracks configurations. For validation purposes, geometries of the domains where flexural and shear cracks developed were chosen considering differing geometries. Domain geometry and experimental data for flexural cracking were adapted from the experimental ERT study (Smyl, Pour-Ghaz & Seppänen 2018) while the domain geometry for shear crack was adapted from (Ma & Li 2018). However, since raw ERT experimental data was not obtained during the shear testing, the shear cracking investigation uses simulated data generated from randomized shear crack distributions. Parameters of the domains that are developing both types of cracking are provided in Tables 14 and 2. We note that the use of simulated data also facilitates quantitative assessment with respect to true cracking patterns.

Table 1: Geometry and mesh details for the flexural cracking investigation.

| Parameter | Value |
|-----------------------------------|--------------|
| Width | 18cm |
| Height | 4.3cm |
| Horizontal Electrodes (Each Side) | 12 |
| Horizontal Spacing | 1.5cm, 2cm |
| Vertical Electrodes (Each Side) | 2 |
| Vertical Spacing | 2.3cm |
| Electrode Width | 0.23cm |
| Electrode Depth | 0.15cm |

Table 2: Geometry and mesh details for the shear cracking investigation.

| Parameter | Value |
|-----------------------------------|--------------|
| Width | 1.5m |
| Height | 1m |
| Horizontal Electrodes (Each Side) | 8 |
| Vertical Electrodes(Each Side) | 8 |
| Electrode Width | 0.055m |
| Electrode Depth | 0.055m |

The discretizations for both investigations are shown in Figures 14 and 15. Spacing and locations of electrodes can be seen in the meshes with reference to Tables 1 and 2. In all cases, internal conductivity distributions were mapped on the discretizations in order to form a continuous distribution within the domain. For this, prior Gaussian background conductivity information was incorporated when generating the samples. In generating homogeneous backgrounds, conductivities in the range of 8-10 mScm⁻¹ were assumed in order to mimic

realistic silver sensing skins (following (Seppänen, Hallaji & Pour-Ghaz 2017)) in the flexural case as well as incorporating isotropic smoothness with a correlating length of 4 cm to incorporate spatial inhomogeneity. In the case of shear cracking, homogeneous background of 0.1 mScm^{-1} was reasonably assumed in all instances to simulate potentially low-conductive large elements.

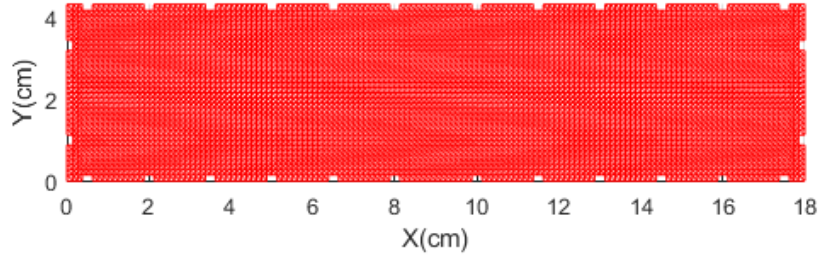


Figure 14: Domain discretization for the flexural cracking investigation consisting of 2557 nodes and 4896 elements.

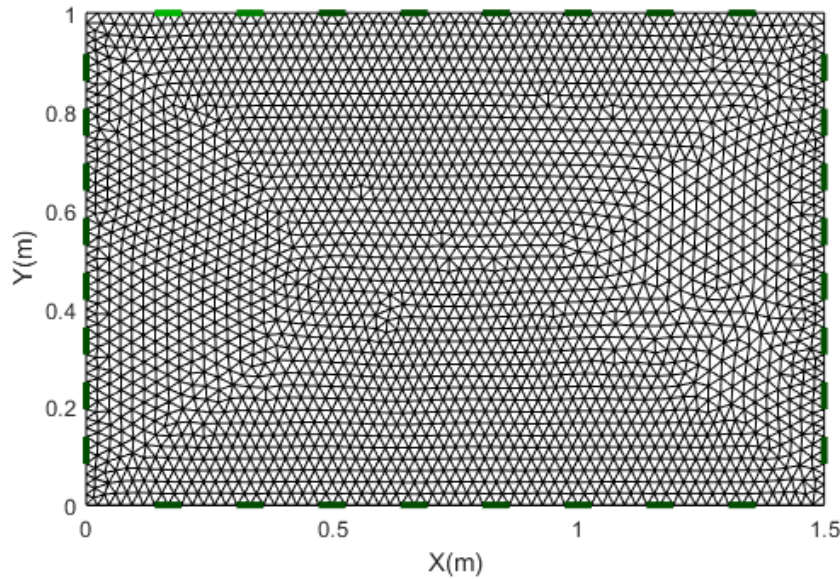


Figure 15: Domain discretization for the shear cracking investigation consisting of 5047 nodes and 9680 elements.

In order to simulate measurement data with the ERT forward model, we adopt opposite current injection patterns while voltage measurements were taken via adjacent electrode pairs. Each flexural crack training sample consists of 3024 voltage measurements and a corresponding conductivity vector with 5047 (nodal) entries. Downsampled flexural crack training sam-

ples consist of the same number of measurements, however the size of conductivity vector is reduced to 915 entries using bi-linear interpolation. Similarly, shear crack training samples consist of 196 voltage measurements (which are reshaped to the 14×14 input size for use in CNNs). Additionally, each shear crack training sample also contains a conductivity vector having 1148 entries. Lastly, 2% Gaussian noise was added to all voltage and conductivity training data sets to improve regularization, prevent over fitting and improve network generalizability (Bishop 1995, Poole, Sohl-Dickstein & Ganguli 2014, Neelakantan, Vilnis, Le, Sutskever, Kaiser, Kurach & Martens 2015).

5.4.2 Crack pattern generation

In order to train the NNs, artificial cracks need to be generated and incorporated into the training samples. For the flexural cracking training set generation, cracks were initialised at the bottom of the domain using prior knowledge of the loading and boundary conditions (i.e. three-point bending). For this, generators consisting of one or two cracks were initialized at different starting locations with various progressing directions. Cracks were simulated by random incremental steps of which the total number is randomized, leading to cracks that could reach arbitrary length within the boundary, such that a sufficient number of training samples were available. Meanwhile, shear cracks were initialised within the domain, while crack progression directions were controlled within a range of $0 - 45$ degrees resulting from the experimental shear testing boundary condition information. Representative internal conductivity distributions for both cracking mechanisms are shown in Figure 16 and Figure 17.

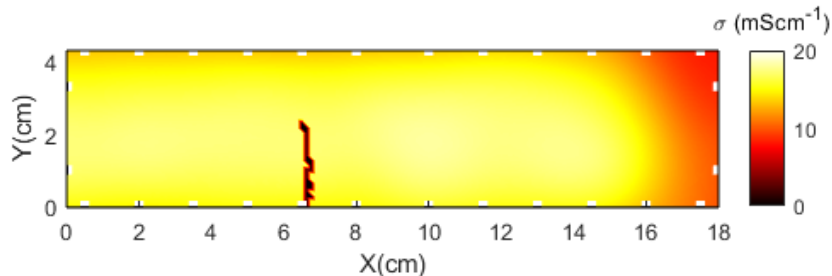


Figure 16: Sample conductivity distribution used in flexural cracking training data.

5.4.3 Data Processing and Training

As indicated previously, the aim of the network training process is to learn the nonlinear mapping between ERT difference measurements and binary crack distributions. To do this,

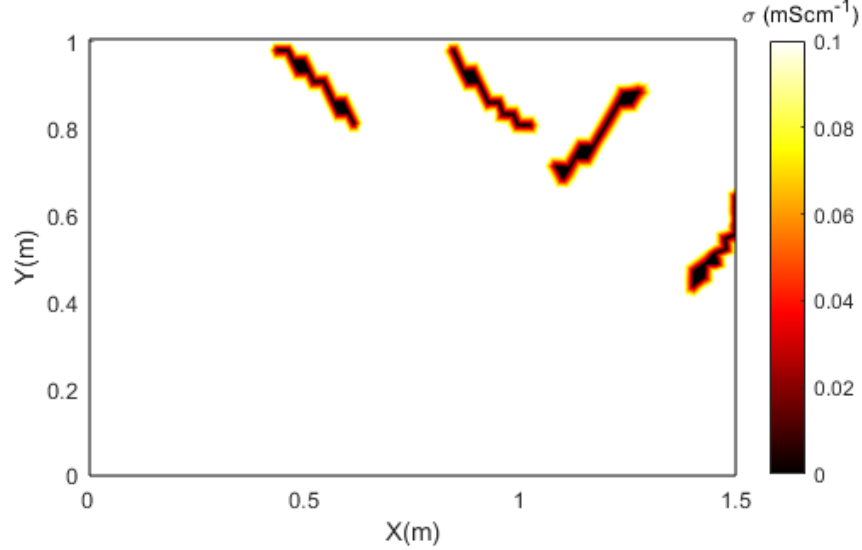


Figure 17: Sample conductivity distribution used in shear cracking training data.

Keras (Chollet 2015) is implemented in a Python environment for both generating NN architectures and training. In training an individual NN, \mathcal{A} , we utilize $t \in N$ training data comprising $\Delta\tilde{V}$ and \tilde{p}_σ where the tilde denotes training data. This process can be holistically written as

$$\mathcal{A}(\Delta\tilde{V}) \rightarrow \tilde{p}_\sigma. \quad (40)$$

Based on this information, we may now explicitly write the desired training loss function as follows

$$\mathcal{L} = -\frac{1}{N} \sum_{t=1}^N [\tilde{p}_{\sigma,t} \log(p_t) + (1 - \tilde{p}_{\sigma,t}) \log(1 - p_t)] + \lambda \|w\|^2. \quad (41)$$

The preceding loss function minimization is augmented with a dropout rate of 50%, effectively supplementing L_2 weight regularization and noise addition to data, to further improve network generalizability and prevent over fitting (Srivastava, Hinton, Krizhevsky, Sutskever & Salakhutdinov 2014).

Regarding the generated training data, the overall dimensionality of both inputs ($\Delta\tilde{V}$) and outputs (\tilde{p}_σ) is immense due to (a) the fine discretizations and (b) the large number of measurements used. Hence a spatially-interpolated downsampling step is additionally considered in order to map the high fidelity distributions of \tilde{p}_σ onto a smaller nodal space, thus aiming to reduce the overall dimensionality of this mapping task for the NN. Such a reduction is expected to result in a reduced error space during gradient descent process.

Owing to the fact that the dimensionality of $\Delta\tilde{V}$ is significantly smaller than \tilde{p}_σ (a common feature in ERT), the training process effectively stretches and amplifies information in $\Delta\tilde{V}$ via NN throughput of $\Delta\tilde{V} \rightarrow \tilde{p}_\sigma$. Therefore, given the dimensionality mismatches, the design of NN architectures is conducted via trial and error. To this end, an ANN is applied for both flexural and shear cracking applications while the use of a CNN is explored for reconstructing shear cracking alone. Regarding the latter, the central reason for not utilizing a CNN for flexural cracking predictions is owed to realizations made during preliminary trial and error processes – namely, that ANNs of basic architectural complexity were sufficient for flexural cracking predictions thereby negating the need for computationally-demanding CNN training. Schematic ANN and CNN architectures are provided in Figures 18 and 19, respectively.

The finalized ANN architecture used for flexural crack predictions is comprised of one input layer, two hidden layers each consisting of 2000 neurons equipped with ReLU activation functions, and an output layer consistent with the number of entries in an individual sample in \tilde{p}_σ . Additionally, the ANN architecture for shear cracking predictions includes three hidden layers of each consisting of 900 neurons with ELU activation functions followed by output layer with the same number of entries in an individual sample in \tilde{p}_σ . Procedurally, the ANN training processes are set to stop when the loss function for validation data consisting of 5000 independent samples exceeded a patience of 100 epochs.

Unlike in the straightforward implementation of ANNs where we map a vector to a vector, we utilize image-based CNNs. As such, we require a rectangular input; consequently, we choose to reshape the input data $\Delta\tilde{V}$ to a 14×14 matrix form. This information is then fed into one convolutional layer with 32 filters having a kernel size of 2×2 followed by a 1×1 max pooling

Table 3: Summary of the ANN architecture used for reconstructing flexural cracks.

| Neural Network input $\Delta\tilde{V}$ with size (1,3024) | | |
|---|--------------|---------------------|
| Layer(type) | Output Shape | Activation Function |
| Input Layer | (1, 3024) | ReLU |
| Hidden Layer 1 (Dense) | (1, 2000) | ReLU |
| Dropout (Dropout Rate: 0.5) | (1, 2000) | |
| Hidden Layer 2 (Dense) | (1, 2000) | ReLU |
| Dropout (Dropout Rate: 0.5) | (1, 2000) | |
| Output Layer (Dense) | (1, 915) | sigmoid |

Neural Network output \tilde{p}_σ with size (1,915)

Table 4: Summary of ANN architecture used for reconstructing shear cracks.

| Neural Network input $\Delta\tilde{V}$ with size (1,3024) | | |
|---|--------------|---------------------|
| Layer(type) | Output Shape | Activation Function |
| Input Layer | (1, 3024) | eLu |
| Hidden Layer 1 (Dense) | (1, 900) | eLu |
| Dropout (Dropout Rate: 0.5) | (1, 900) | |
| Hidden Layer 2 (Dense) | (1, 900) | eLu |
| Dropout (Dropout Rate: 0.5) | (1, 900) | |
| Output Layer (Dense) | (1, 1148) | sigmoid |

Neural Network output \tilde{p}_σ with size (1,1148)

layer. Secondly, the same sets of convolutional and max pooling layers were added. Then, a flatten layer was added before a fully connected ANN structure consisting of three hidden layers with 4500 neurons each. ReLU activation functions were used in hidden layers while sigmoid functions were applied in the output layer. In training, 5000 samples were utilized and found to be sufficient to adequately train the network. However, in previous trial and error procedures, it was found that significant computational resources were needed in order to optimize the CNN parameters. This was owed to the lack of distinguishability in input voltage data corresponding to conductivity changes central region of the domain (a common sensitivity issue in ERT).

Based on the former preliminary realizations, we propose and investigate an alternate approach to CNN predictions where the conductivity vector is segmented to five pieces. As a result, five different NNs are trained and developed with reduced dimensionality aiming at

Table 5: Summary of CNN architecture used for reconstructing shear cracks.

| Neural Network input $\Delta\tilde{V}$ with size (1,14,14) | | |
|---|--------------|---------------------|
| Layer(type) | Output Shape | Activation Function |
| Input Layer | (1, 14, 14) | |
| Convolutional Layer 1 (Conv2D) | (7, 7, 32) | |
| Max Pooling Layer 1 (Max Pooling) | (7, 7, 32) | |
| Convolutional Layer 2 (Conv2D) | (6, 6, 32) | |
| Max Pooling Layer 2 (Max Pooling) | (6, 6, 32) | |
| Flatten Layer (Flatten) | (1, 1152) | |
| Hidden Layer 1 (Dense) | (1, 4500) | ReLu |
| Dropout (Dropout Rate: 0.5) | (1, 4500) | |
| Hidden Layer 2 (Dense) | (1, 4500) | ReLu |
| Dropout (Dropout Rate: 0.5) | (1, 4500) | |
| Hidden Layer 3 (Dense) | (1, 4500) | ReLu |
| Dropout (Dropout Rate: 0.5) | (1, 4500) | |
| Output Layer | (1, 1148) | sigmoid |
| Neural Network output \tilde{p}_σ with size (1,1148) | | |

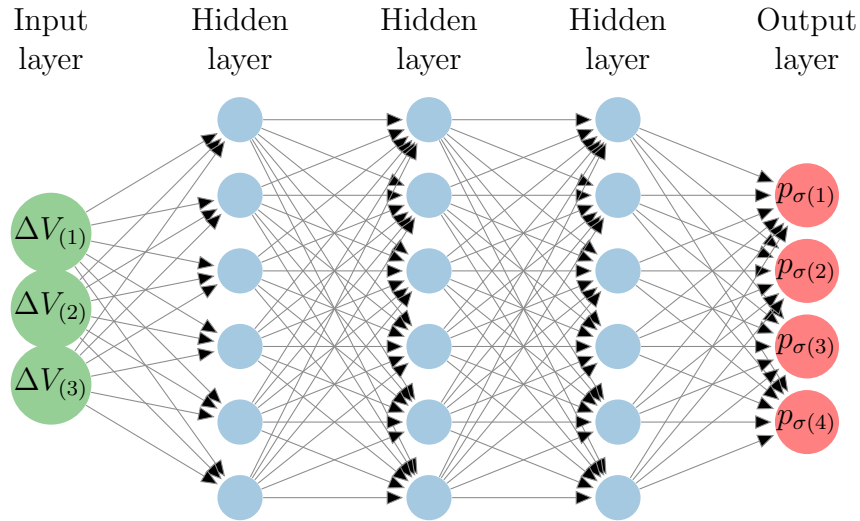


Figure 18: Schematic trained ANN architecture.

improving prediction accuracy for individual segments and overall domain predictions after the final assembly of segments. Another advantage of this methodology relates to regions where information is poor – especially the central region – where (a) more training samples can be added or (b) other parameters could be adjusted to improve the training performance avoiding the need to retrain a large (entire domain) CNN.

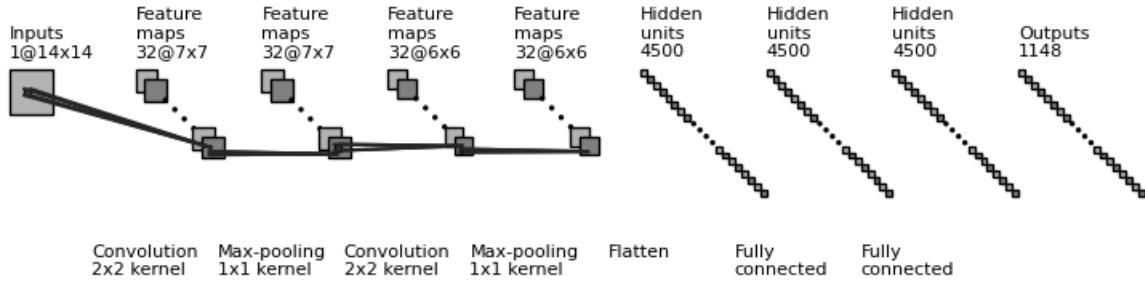


Figure 19: Schematic trained CNN architecture.

Lastly, to provide more detailed information on network training, figures 20 and 21 show the training processes for two typical NNs. In these figures, we observe a near immediate reduction in the loss indicating rapid learning. Following this initial phase, a gradual decrease in the loss function is observed, characterized by fine-tuning of the network weights and biases. It is worth noting here that, since different network architectures and training samples are used in this work, the number of epochs varies needed to reach respective stopping criteria varies significantly.

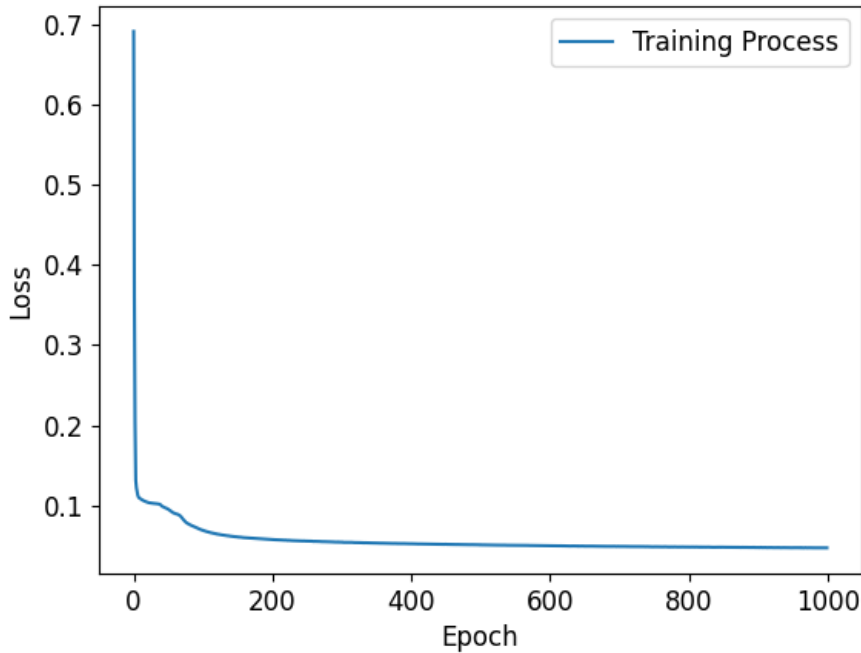


Figure 20: Loss function minimization for an ANN used in this work.

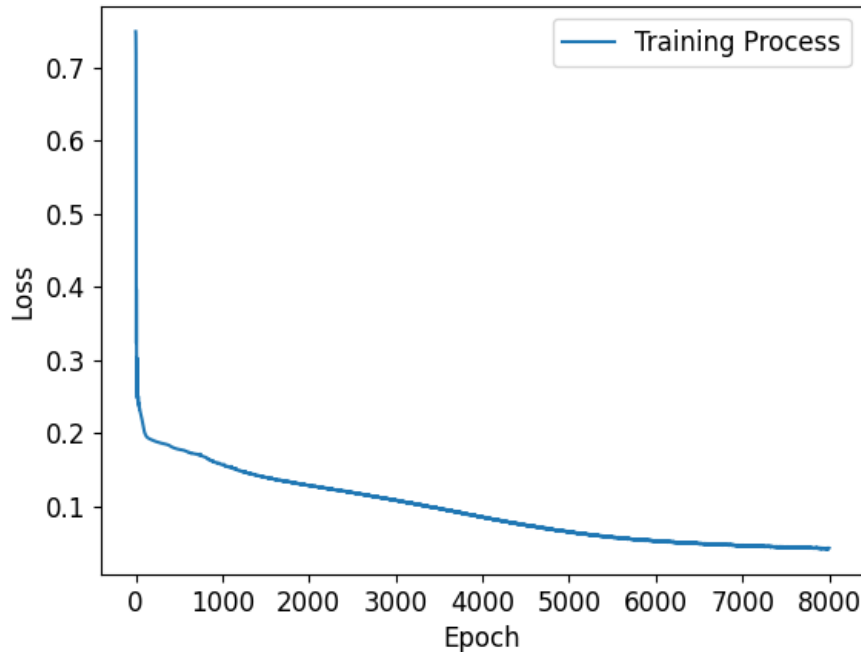


Figure 21: Loss function minimization for an CNN used in this work (non-segmented data).

5.5 Results and Discussion

In this section, we report and discuss cracking predictions from experimental flexural and simulated shear testing campaigns. Tabulated images showing these cracking predictions are reported in Figures 22 and 23. In the spatial mappings reported, color bars represent the probability of cracks existing at a nodal location. For the purpose of quantitative comparison, the mean square error (MSE) metric, measured between the predictive results and simulated results, for shear cracks are summarized in Table 6. In the forthcoming subsection, we will detail results for flexural testing, followed by a subsection detailing shear testing predictions, and lastly discussion will be provided.

5.6 Flexural Crack Reconstruction

Flexural cracking predictions are shown in Figure 22 alongside experimental photographs with highlighted crack. Column *a* shows the experimental photographs, column *b* shows the crack predictions based on full conductivity sampling, and column *c* reports predictions using based on downsampled conductivity. Generally speaking, NN predictions correctly localize the initial crack topology (top row) in comparison to the experimental photographs

as observed in a_1 , b_1 and c_1 . In addition, crack growth can be observed in b_2 and c_2 for both data types while the downsampled data prediction visually outperforms the full data prediction in terms of the actual length of the growing crack. In b_3 and c_3 , only a single crack can be observed, which matches the left crack shown in a_3 . Further, in b_4 and c_4 , both the full and downsampled predictions accurately capture both cracks.

As a whole, we observe improved predictions when utilizing downsampled data. It is worth nothing, however, that this qualitative observation comes at a loss of spatial resolution in predictions p_σ . It can also be observed that in predictions b_3 and v_3 , the reconstructions do not capture the right crack, irrespective of sampling fidelity, this drawback can be potentially explained by the presence of the left crack, which effectively shields electric fields and leads to a reduction in measurement information needed in resolving the right crack (Smyl, Pour-Ghaz & Seppänen 2018). In addition, the inability to accurately predict the right crack in the third row could also be due to the relatively large width to depth ratio of this domain, where electric fields flowing horizontally are, in as rough sense, more constrained than in geometries having aspect ratios approaching 1:1. Moreover, the presence of small artifacts can be observed in c_3 and c_4 which result from NN predictive errors (a function of, e.g. measurement noise and geometrical discretization error), however these errors are small relative to topological crack prediction errors and do not significantly corrupt the overall assessment of crack predictions.

5.6.1 Shear Crack Reconstruction

ANN and CNN shear cracking predictions based on downsampled data are reported in Figure 23. Column a shows the true cracking binary representation. Column b reports ANN predictions for the entire domain. Column c reports CNN predictions results for the entire domain. Lastly, column d reports segmented CNN predictions. In addition, consolidating five segmented networks. In total, four differing cracking patterns of increasing complexity are considered (least complexity in the top row and most complexity in the bottom row).

Generally speaking, for simple crack patterns (i.e. the first and second rows), both the ANNs and CNNs provide valid predictions in terms of crack lengths and locations. However, when observed in closer detail, the ANN visually outperforms the CNN predictions slightly as in b_1 and b_2 where the length of cracks are more accurately predicted. For more complex crack

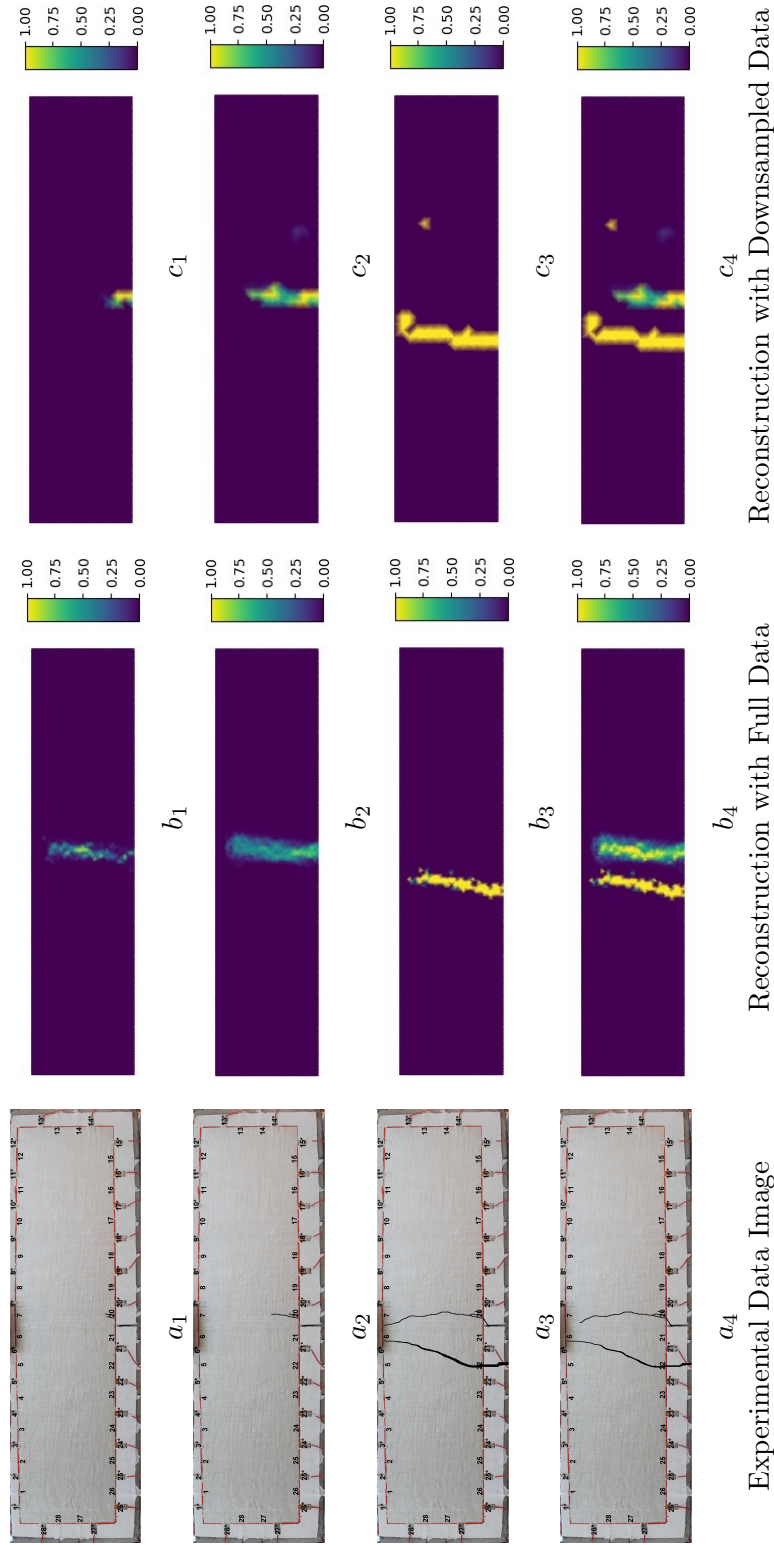


Figure 22: NN predictions of experimental flexural cracking patterns.

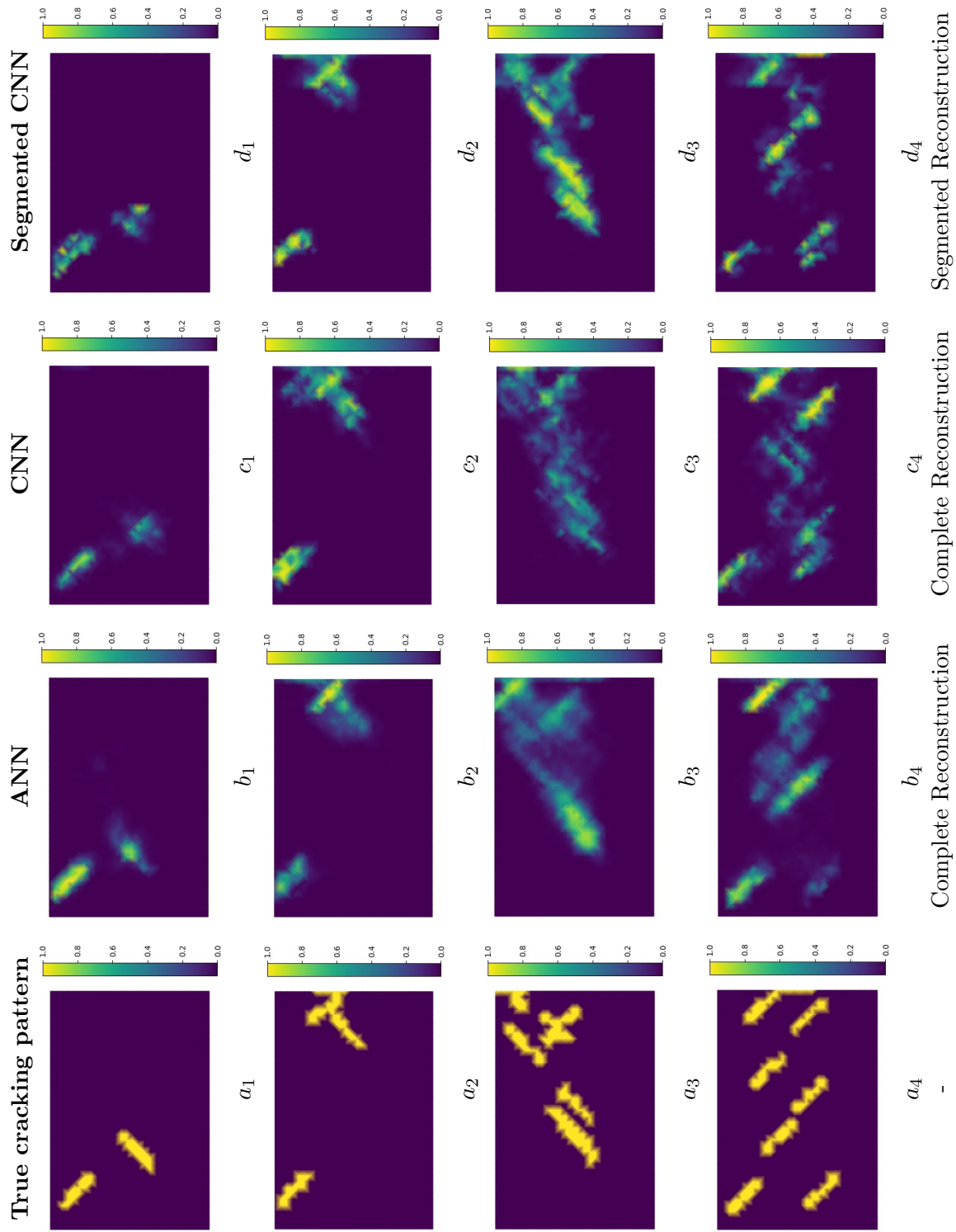


Figure 23: NN predictions of simulated shear cracking patterns.

patterns (i.e. the third and fourth rows), all NN cracking predictions are satisfactory near the domain boundaries. On the other hand, near the center of the domains (the area of least sensitivity), CNNs appear to localize and separate complex cracks better than ANNs as observed from c_3 , d_3 , c_4 , and d_4 . Furthermore, segmented CNN predictions consistently show improved qualitative results in comparison to the conventional CNN network.

In totality, both the ANNs and CNNs predict less accurately towards the central region of the domain relative to the boundary. This is likely caused by the diffusive nature of electricity and is also a common feature of ERT (Hallaji, Seppänen & Pour-Ghaz 2014). However, despite the generally better qualitative results predicted by CNNs, we require a quantitative metric to more closely assess predictions. For this, we utilise the MSE metric, effectively comparing true and predicted images; these metrics are reported in Table 6.

In contrast to visual observations, assessment of MSEs reported in Table 6 (information in Table 6 can be read in accordance with Figure 23) indicate that ANNs generally perform quantitatively slightly better than CNNs – with the notable exception of one cracking pattern. This could potentially be due to fact that the CNNs’ architecture and data processing adds additional nonlinearity in the training and prediction process. While this initially seems counterintuitive, as CNNs are commonly regarded as more powerful predictive tools than ANNs, additional discussion is required to attain a more full picture of the realizations made in this subsection. Such discussion will be provided henceforth.

5.6.2 Discussion

The feasibility of NNs for probabilistically predicting cracking patterns was qualitatively and quantitatively affirmed in the preceding subsections using experimental and simulated data. Generally speaking, the networks were able to localize binary crack representations with regional certainty exceeding 50% – with the notable exception of cases where measurement quality was impeded by crack shielding. As alluded to, the use of NNs for predicting cracks using boundary voltage measurements is analogous to ERT, with the caveat that the learned methodology proposed herein *predicts binary cracking representations* rather than reconstructing continuous conductivity distributions. Interestingly, the proposed NN crack prediction framework also exhibits similar susceptibilities present in ERT; the primary weak-

Table 6: Mean square errors for shear crack predictions.

| Network Type | Crack Pattern | MSE |
|--------------------------|----------------------|------------|
| ANN | Complex Pattern 1 | 0.057 |
| | Complex Pattern 2 | 0.046 |
| | Simple Pattern 1 | 0.019 |
| | Simple Pattern 2 | 0.022 |
| CNN with Complete Figure | Complex Pattern 1 | 0.097 |
| | Complex Pattern 2 | 0.065 |
| | Simple Pattern 1 | 0.022 |
| | Simple Pattern 2 | 0.015 |
| Segmented CNN | Complex Pattern 1 | 0.088 |
| | Complex Pattern 2 | 0.067 |
| | Simple Pattern 1 | 0.025 |
| | Simple Pattern 2 | 0.021 |

nesses include (a) insensitivity to the central region of the prediction domain and (b) low spatial resolution. Conversely, and again similar to ERT, the NN prediction framework also has analogous advantages including (i) high sensitivity near the boundaries and high temporal resolution. In contrast to ERT, however, the NN prediction framework enables substantial computational speedups and simpler representation of cracking topology relative to conventional ERT.

Despite the noted advantages, two observations made in the results subsections remain yet to be explained. Realizations from these observations have key implications on the potential use of predictive networks for probabilistic crack assessment in future work. Firstly, the use of spatial downsampling proved highly effective and generally improved prediction quality. Secondly, the use of CNNs, commonly considered a more powerful classification network, only outperformed ANNs in one case considered.

In response to the first observation, we need to first investigate the general structure of input and output data sets used herein. We note that, when binary crack representation data (output) is not downsampled, the output dimensionality is an order of magnitude larger

than input measurement data. As such, information stemming from measurements is significantly diffused and stretched before reaching the outputs. This is similar to the process of decoding, i.e. mapping low dimensional information to high dimensional information, as commonly adopted in autoencoder applications (An & Cho 2015, Lee & Carlberg 2020). A primary challenge presented in the decoding process lies in the preservation of information transferred from input to output. Potential for corruption in decoding, however, can be reduced by optimizing the NN architecture and decreasing discrepancy between input/output data size. Regarding the latter, downsampling of the outputs (as used herein) is an effective method for matching data sizing discrepancies and therefore underscores the effectiveness of downsampling in crack prediction quality observed.

Responding to the second observation, regarding the reduced effectiveness of CNN cracking predictions in comparison to those of ANNs, we would like to remark that this was an unexpected result. Nowadays, applications of CNNs range from image processing to inverse problems. Recent scholarly work has even investigated the “unreasonable effectiveness of CNNs” (Hauptmann & Adler 2020). Yet, like many machine learning tools, the use of specific architectures and data processing techniques should be considered with respect to the application and underlying data structure(s).

In this work, the input data (potential differences) may have a positive or negative sign and the magnitude can vary significantly, depending on the cracking pattern, domain geometry, electrode configuration, and measurement/stimulation protocol. In turn, reshaping such data into a rectangular “voltage image” unquestionably represents a much more complex data structure than if it were, for example, a black and white image consisting of positive integer values ranging from 0 to 255. Therefore, the use of convolutional operations in comparison to feedforward (ANN) operations may not be ideal in many cases. Such a realization may contribute to the fact that CNNs performed less favorably than ANNs in predicting all but one cracking representation.

The former deduction is not a general conclusion of this work, however, as CNNs (and fully-connected networks) offer opportunities for deeper data representation. For example,

derivative operations have equivalencies to convolution operations (Simoncelli 1994, Chen & Pock 2016) meaning that higher order data representations are possible using CNNs. Therefore, the use of deeper non-fully connected networks highly tailored to data and prediction may, in eventuality, lead to substantially improved predictions of cracking representations than those reported herein and this is the source of ongoing research.

5.7 Conclusions

In this paper, fast Neural Network driven direct inversion frameworks were proposed to predict binary cracking distributions in concrete elements. The aim of the proposed framework was to map boundary electrical measurements to probabilistic binary crack distributions. The purpose for choosing a binary cracking representation was to simplify the interpretability of damage predictions. To test the feasibility of the approach, experimental flexural cracking representations were successfully predicted with using ANNs. To facilitate quantitative evaluation of networks' efficacy, simulated shear cracking representations were predicted using ANNs and CNNs. Simulation results generally indicated that ANNs slightly outperformed CNNs quantitatively, while both architectures showed the potential to accurately reconstruct simple and complex crack patterns. In summary, the feasibility of the proposed learned frameworks was affirmed and discussion was provided to offer guidance on the potential for improving network predictions.

5.8 Acknowledgements

DS acknowledges Professor Moe Pour-Ghaz (North Carolina State University), Professor Aku Seppänen (University of Eastern Finland) and Dr. Milad Hallaji (Fernandez & Associates) for providing experimental data. DS was supported by Engineering and Physical Sciences Research Council Project EP/V007025/1. DL was supported by the National Natural Science Foundation of China under Grant 61871356.

6 Predicting strain and stress fields in self-sensing nanocomposites using deep learned electrical tomography

Authorship: Liang Chen, Hashim Hassan, Tyler N Tallman, Shan-Shan Huang and Danny Smyl

Published Journal: Smart Materials and Structures, Volume 31, Number 4

DOI: 10.1088/1361-665X/ac585f

6.1 Abstract

Conductive nanocomposites, enabled by their piezoresistivity, have emerged as a new instrument in structural health monitoring. To this end, studies have recently found that electrical resistance tomography (ERT), a non-destructive conductivity imaging technique, can be utilized with piezoresistive nanocomposites to detect and localize damage. Furthermore, by incorporating complementary optimization protocols, the mechanical state of the nanocomposites can also be determined. In many cases, however, such approaches may be associated with high computational cost. To address this, we develop deep learned frameworks using neural networks to directly predict strain and stress distributions – thereby bypassing the need to solve the ERT inverse problem or execute an optimization protocol to assess mechanical state. The feasibility of the learned frameworks is validated using simulated and experimental data considering a carbon nanofiber plate in tension. Results show that the learned frameworks are capable of directly and reliably predicting strain and stress distributions based on ERT voltage measurements.

6.2 Introduction

6.2.1 Background and context

Composite materials are widely applied in civil, automotive and aerospace industries due to their advanced mechanical properties and applicability for bespoke implementation (Mangalgi 1999, Hassan & Tallman 2020*b*). Structural health monitoring (SHM) of composite structures is, therefore, a subject of increasing importance, owing to their rising prevalence. In SHM practices, traditional non-destructive testing (NDT) approaches such as magnetic,

radiographic, acoustic, ultrasonic and photographic testings have already shown promises in monitoring the structure's conditions (Gholizadeh 2016, Mutlib, Baharom, El-Shafie & Nuawi 2016, Montinaro, Cerniglia & Pitarresi 2018, Kong & Li 2018). However, locations of (potential) damages are often required as *a priori* for traditional NDT modalities (Farrar & Worden 2012), since localized methods are often associated with higher sensitivities in terms of detecting the damage. As a result, their pragmatic applications for large domains are limited. On the other hand, Electrical Resistance Tomography (ERT) is an imaging modality, which aims at reconstructing conductivity distributions from boundary voltage measurements. It has advantages such as low energy cost, rapid data collection and efficacy to offer spatial monitoring over large areas (Chen, Gallet, Huang, Liu & Smyl 0). To this point, recent studies have shown ERT's benefits for monitoring and evaluation of cement-based materials (Karhunen, Seppänen, Lehtikoinen, Monteiro & Kaipio 2010, Smyl 2020), reconstructing simple and complex crack patterns on concrete elements (Smyl, Pour-Ghaz & Seppänen 2018).

In addition to cementitious materials, work has also been done to develop self-sensing polymeric composite materials by incorporating conductive nano-scale phases, such as carbon nanofibers (CNFs) and carbon nanotubes (CNTs). In these materials, electrical transport is a consequence of percolation – electrical current propagates from filler-to-filler through the material. Deformations that alter the connectivity of this network or damage that severs the connection between fillers, therefore, manifest as a conductivity change. Thus, the material is self-sensing via the piezoresistive effect. Unlike traditional point-based sensors, the self-sensing nature of these materials could potentially enable a spatially continuous SHM approach. ERT is, therefore, a natural complement to these materials since it allows for spatially continuous mapping of conductivity changes. The application of ERT to self-sensing polymers has received considerable attention to date (Tallman, Gungor, Wang & Bakis 2015, Thomas, Kim, Tallman & Bakis 2019, Gallo & Thostenson 2016, 2015, Baltopoulos, Polydorides, Pambaguian, Vavouliotis & Kostopoulos 2015, Tallman & Smyl 2020).

Despite the seemingly high potential of combining self-sensing materials with ERT, some limitations of this approach exist. For example, due to the complexities associated with solv-

ing ERT inverse problems, ERT reconstructions often show lower fidelity results compared with some traditional NDT modalities (Smyl, Bossuyt, Ahmad, Vavilov & Liu 2020). Efforts have been made to increase the spatial resolution by incorporating prior structural information into the inverse model (Smyl, Pour-Ghaz & Seppänen 2018). Moreover, introducing non-iterative reconstruction methods could reduce the computational time, but at the risk of decreasing the spatial resolution (Ferreira & Novotny 2017). In addition to these limitations, ERT also does not directly show mechanical effects such as stress or strain. That is, ERT maps electrical conductivity. Even though conductivity is directly dependent on strain in piezoresistive materials, SHM and NDT practitioners would much rather know the strain field directly. To address this limitation, Tallman and colleagues introduced the concept of piezoresistive inversion (Tallman & Wang 2016, Tallman, Gungor, Koo & Bakis 2017). The goal of piezoresistive inversion is to invert the observed conductivity distribution in order to recover the underlying displacement field (and in turn the strain field via kinematic relations and the stress field via elastic constitutive relations). This necessarily requires a suitable macroscale piezoresistivity model that is amenable to general deformations (as opposed to simple uni-axial piezoresistivity models) (Tallman & Wang 2013, Koo & Tallman 2020). Initial work in this area was done using analytical inversion methods (Tallman & Wang 2016, Tallman, Gungor, Koo & Bakis 2017); however, it was soon found that these methods can fail to converge to physically meaningful solutions if the strain field is complex. Therefore, metaheuristic methods such as genetic algorithms (GAs), particle swarm optimization, and simulated annealing were next explored (Hassan & Tallman 2020*b,a*). Even though these methods were successful in recovering the strain field from conductivity data, they are limited by their computational expense.

In light of the preceding discussion, we can see that there is considerable potential in truly full-field stress/strain mapping via self-sensing materials plus ERT, but existing frameworks for solving this inverse problem have important limitations (i.e. convergence to non-physical solutions and computational cost). We therefore propose to advance the state of the art by applying machine learning techniques to solve this inverse problem with high accuracy and substantially reduced computational cost. The novelty of this work is the development

of deep learned frameworks that directly map boundary voltage measurements to the first principal strain and stress distributions via neural networks (NNs) with the aim of achieving continuous and accurate monitoring of self-sensing composites. The proposed frameworks utilize piezoresistive properties of nanocomposites as well as the mapping capabilities of deep learned neural networks to predict the first principal strain and stress fields over the entire domain based on absolute boundary voltage measurements.

6.2.2 Machine learning and neural networks

Machine learning originated as a research subject in the 1950s for pattern and shape recognition tasks (Kröse, Krose, van der Smagt & Smagt 1993, Rosenblatt 1958). The concept of perceptrons (Binary classifiers) was initially proposed by Frank Rosenblatt which was later then developed to multi-layer perceptrons (MLP) (Rosenblatt 1958). With the discovery of back-propagation and the developments of advanced computer infrastructures, machine learning began to draw larger research interest. By increasing the number of perceptrons and layers with expanded training data sets, deep neural networks were later developed and implemented for increasingly complex applications by recognizing non-linear patterns (Goodfellow, Bengio, Courville & Bengio 2016, LeCun, Bengio & Hinton 2015). In initial studies about perceptrons, it was found that a single layer perceptron network was sufficient for recognizing any linear patterns theoretically (Papert 1961, Baum 1988), while the probability of recognizing the desired patterns was directly proportional to the increasing number of perceptrons/neurons (LeCun, Bengio & Hinton 2015, Bishop et al. 1995).

In this paper, we are interested in applying NNs to solve two regression problems aiming to map boundary voltage measurements (V) to the first principal strain and stress spatial distributions (ϵ_p and σ_p), respectively. For this purpose, the mean absolute error (MAE) function with regularization is used as the loss function to train the NNs. The MAE is formulated as follows:

$$\mathcal{L} = -\frac{1}{N} \sum_{i=1}^N |y_i - Y(x_i)| + \lambda \|w\|^2 \quad (42)$$

In Equation (42), \mathcal{L} represents the loss function which needs to be minimized during the training process. The average of absolute error between i^{th} desired output (y_i) and predicted output ($Y(x_i)$) is calculated across all training samples. N represents the total number of training samples. In addition, an extra L_2 norm is added on all network weights (w) with λ representing the regularization parameter used to avoid over-fitting (Ying 2019). In minimizing Equation (42), the proposed NNs are, in essence, generating functions which produce the least error between desired and predicted outputs. Namely, after sufficient training epochs, Y represents the regression mapping from $V \rightarrow \epsilon_p$ or $V \rightarrow \sigma_p$.

Minimization of the loss function is generally achieved by applying a gradient descent algorithm and back-propagation during training (LeCun, Boser, Denker, Henderson, Howard, Hubbard & Jackel 1989). Other machine learning methodologies such as Hopfield Network and Boltzman Machine based on statistical mechanics can be implemented to minimize the loss function, they are however less applied in pragmatic fields (Hopfield 1982, Ackley, Hinton & Sejnowski 1985). principals of applying machine learning in the SHM field are well laid out by Farrar and Worden (Farrar & Worden 2012) for the reader’s reference. Furthermore, in recent studies, Tibaduiz et al. have shown machine learning can serve as a new damage classification approach (Tibaduiza, Torres-Arredondo, Vitola, Anaya & Pozo 2018). Mousavi et al. has utilized NNs to denoise vibration data for extracting more damage-sensitive features (Mousavi, Varahram, Ettefagh, Sadeghi & Razavi 2020). In this work, since the implementation of the SHM modality often requires big data collection and rapid data processing to achieve continuous monitoring, it is worth remarking that machine learning as a data driven methodology may have great potential when implemented with SHM modalities.

6.2.3 Paper structure

This paper firstly reviews the historical SHM applications of ERT. Furthermore, this paper discusses the traditional solution to an ERT inverse problem. The experimental data acquisition process for obtaining the absolute voltage measurements on CNF with ERT is introduced in the subsequent section followed by the proposed machine learning methodology. Moreover, we present the formulation of a integrated model (consisting of a elastic mechanical model, complete electrical model and the piezoresistivity model) that is used for generating training

data as well as the architectures of the proposed NNs. In the following sections, predictive strain and stress distributions based on simulation and experimental measurements are reported followed by discussions in terms of (a) training data processing, (b) the advantages and disadvantages of the proposed approach and (c) potential future research interests. This paper is then finalized by a conclusion section.

6.3 Electrical Resistance Tomography

ERT is a diffusive imaging modality which aims to reconstruct the conductivity distribution of a domain from boundary voltage measurements. In the context of ERT data collection, electrodes are installed on the boundary of the domain and then currents are injected into electrodes while potential differences between two electrodes are recorded. Pioneering ERT research was initially developed for medical imaging based on differences between organ conductivities and was then applied on capacities and inductive topographies (Henderson & Webster 1978, Yang & York 1999). During recent research, deep learning methodology has been implemented with ERT in the field of medical imaging. For example, Seo et al. successfully applied a deep learning based method to reconstruct simulated CT scans of lungs (Seo, Kim, Jargal, Lee & Harrach 2019) and Duan et al. managed to use electrical impedance tomography (EIT) and deep learning to reconstruct real time touch sensing (Duan, Taurand & Soleimani 2019). More recently, engineers and scientists have studied ERT as a SHM and NDT modality. ERT was, in this context, explored to detect damage and visualize strain fields in composite materials (Hassan & Tallman 2020*b*, Tallman & Smyl 2020, Tallman, Gungor, Koo & Bakis 2017, Loh, Kim, Lynch, Kam & Kotov 2007, Loh, Hou, Lynch & Kotov 2009, Loyola, Briggs, Arronche, Loh, La Saponara, O'Bryan & Skinner 2013, Lestari, Pinto, La Saponara, Yasui & Loh 2016, Tallman, Gungor, Wang & Bakis 2014). Previous studies have also shown that ERT is a valid modality for detecting crack patterns and reconstructing moisture in cement-based materials (Smyl & Liu 2019*a*, Hallaji, Seppänen & Pour-Ghaz 2015, Smyl, Bossuyt, Ahmad, Vavilov & Liu 2020). As alluded to previous sections, high fidelity solutions for ERT inverse problems are usually computationally demanding. Therefore, for the aim of achieving condition monitoring systems based on ERT, recent research has implemented machine learning with ERT. For example, Smyl and Liu explored the optimization

of electrodes' locations using deep learning to collect more informative measurements (Smyl & Liu 2020). In addition, Hamilton and Hauptmann used deep neural networks to reconstruct ERT images (Hamilton & Hauptmann 2018). Chen et al. incorporated NNs to directly reconstruct crack patterns on concrete materials (Chen, Gallet, Huang, Liu & Smyl 0). In addition, researchers explored different deep learning schemes to reconstruct images based on EIT data. For example, Ren et al. utilized a two-stage deep learning method (TSDL) to reconstruct simulated CT scans with high accuracy (Ren, Sun, Tan & Dong 2019). Wei et al. used a dominant current deep learning scheme to reconstruct challenging inclusion shapes with a convolutional neural network (CNN) trained with circle or ellipse training data (Wei, Liu & Chen 2019). Furthermore, Wang et al. developed the error-constraint deep learning scheme (Ec-Net) aiming at yielding more robust and accurate reconstruction via mapping the image and error (Wang, Zhang, Li, Duan, Wang, Zhang, Zhang, Ma, Wang & Jia 2021). In the following sections, we introduce the ERT forward model and the conventional solution to ERT inverse problem, followed by the proposed deep learned framework.

6.3.1 Forward model

In order to solve the ERT inverse problem, a forward model which calculates boundary voltages from conductivity distributions and known measurement/stimulation patterns needs to be formulated alongside physical boundary conditions. Herein, we utilize the Complete Electrical Model (CEM) developed by Cheng et al. (Cheng, Isaacson, Newell & Gisser 1989) which is written as shown in the following equations:

$$\nabla \cdot (\gamma \nabla u) = 0, x \in \Omega \quad (43)$$

$$\int_{e_l} \gamma \frac{\partial u}{\partial n} dS = I_l, l = 1, \dots, L \quad (44)$$

$$\gamma \frac{\partial u}{\partial n} = 0, x \in \partial\Omega \setminus \cup_{l=1}^L e_l \quad (45)$$

$$u + z_l \gamma \frac{\partial u}{\partial n} = U_l, l = 1, \dots, L. \quad (46)$$

Equation (43) describes steady-state diffusion without internal electricity sources where γ represents the conductivity and u represents the potential distribution within domain Ω . In the CEM, x represents the Cartesian coordinates within Ω . In order to solve Equation (43) and formulate a realistic electrical model, boundary conditions need to be applied as expressed in Equations (44) to (46). I_l represents the injected current on electrodes. Meanwhile, L is the total number of electrodes and e_l represents the l^{th} electrode. In addition, n represents the normal vector on the surface dS on Ω . Equation (46) takes the electrodes' contact impedance into account while calculating the voltage measurement U_l on l^{th} electrode for more accurate modeling. z_l represents the contact impedance between the electrodes and the domain.

$$\sum_{l=1}^L I_l = 0 \quad (47)$$

$$\sum_{l=1}^L U_l = 0. \quad (48)$$

By enforcing Equations (47) and (48) on the aforementioned equations, we can force the model to obey the current conservation law with fixed potential reference level (Tallman & Smyl 2020, Vauhkonen, Vadasz, Karjalainen, Somersalo & Kaipio 1998). The CEM can be discretized for FE analysis. However, in pragmatic (inverse) applications, we are interested in reconstructing the conductivity distributions which are often unknown from boundary voltage measurements. Herein, a unique solution needs to be obtained for an estimation of this ill-posed ERT inverse problem. The traditional solution to an ERT inverse problem is discussed in the following section.

6.3.2 ERT inverse problem

In this subsection, we discuss the ERT inverse problem to highlight some of the underlying technical aspects of the modality and associated challenges our proposed methodology aims to circumvent. However, before addressing the inverse problem, we would like to emphasize that the ill-posed nature of an ERT inverse problem is mainly resultant from the following factors: (a) measurement noise from data acquisition, (b) the diffusive nature of electric current, (c) ill-conditioned derivative matrices used in conventional optimization algorithms and (d) numerical modeling errors (e.g. discretization errors in FE implementations). There are two well developed imaging schemes which are absolute and difference imaging. Absolute imaging estimates the conductivity distribution based on voltage measurement from one state. On the other hand, difference imaging estimates the conductivity distribution variation based on voltage measurements from two states. Since we use absolute imaging in this paper, the conventional solution to such scheme is presented in the following paragraph. A typical ERT inverse problem is often first formulated as an observation model by writing

$$V = F(\gamma) \tag{49}$$

where F represents the discretized CEM model. However, due to the existence of measurement and modeling errors, the observation model should be modified as following

$$V = F(\gamma) + e \tag{50}$$

where e represents all potential errors within the inverse problem. The process of solving an ERT inverse problem can then be defined in a least-squares (LS) manner

$$\hat{\gamma} = \{\|V - F(\gamma)\|^2\} \quad (51)$$

where $\hat{\gamma}$ represents the conductivity solution. However due to the ill-posed nature of this inverse problem, an unique solution is not guaranteed (Sarvas 1987) using conventional LS methods. As an alternative, we can obtain an unique solution ($\hat{\gamma}$) by adding a regularization term to Equation (51) as follows (Smyl, Hallaji, Seppänen & Pour-Ghaz 2016)

$$\hat{\gamma} = \{\|L_e(V - F(\gamma))\|^2 + \alpha\|L_\gamma\gamma\|^2\} \quad (52)$$

where α is a scalar that controls regularization between data fit and smoothness. L_e and L_γ are Cholesky factorized noise weighting and regularization matrices used to weigh uncertainty due to expected measurement noise. Herein, this LS based inverse problem can therefore be solved iteratively by incorporating a Gauss-Newton minimizer formulated as follows

$$\delta\hat{\gamma} = (J^T W J + \alpha L_\gamma^T L_\gamma)^{-1} J^T W (V - F(\gamma)) \quad (53)$$

where $\delta\hat{\gamma}$ is the LS minimizer. The term $J^T W J$ estimates the Hessian matrix while W represents the (non-Cholesky factorized) noise model term. The ill condition of J is, as alluded to earlier, stabilised by the regularization matrix $\alpha L_\gamma^T L_\gamma$. Moreover, studies suggest that by including the noise model term W , we may obtain more accurate solutions by weighing based on noise level (Smyl 2020). The above mathematical formulations conclude the traditional solution for an ERT inverse problem in the absolute imaging scheme. Previous research indicates that modeling error can be reduced during the subtraction operation by using difference imaging schemes, hence potentially obtaining more accurate reconstructions

(Smyl, Pour-Ghaz & Seppänen 2018). However, in this paper, we adapt the absolute imaging scheme primarily due to the measurement discrepancy between the simulated and experimental data. In order to compensate this modeling error, only absolute imaging data are valid for pre-processing before training. This pre-processing is further discussed in section 5.1. Although we can obtain an accurate estimation of $\hat{\gamma}$ using conventional optimization regimes, computational demands for solving such inverse problem can significantly increase with finer FE meshing and larger domains. Additional computational demands in iterative frameworks include (a) computation of Jacobian matrices and (b) iterative calculations from Newton-based algorithms (e.g. linesearch). Herein, we propose a deep learned framework via NNs to directly predict the first principal strain and stress fields of CNF-based structures without solving the ERT inverse problem using a conventional optimization framework.

6.4 Experiment Data Acquisition

6.4.1 CNF specimen and experiment set up

A rectangular CNF-modified epoxy specimen with a nanofiller weight fraction of 1.0% was manufactured for experimental testing. The specimen measured 196 mm \times 46.5 mm with a thickness of 4 mm, and had a central hole of diameter 12.7 mm. Grip tabs were bonded to the specimen using epoxy adhesive to prevent damage due to the gripping pressure of the load frame. The gauge section of the specimen measured 81.1 mm \times 46.5 mm. Electrodes were attached to opposite edges of the gauge section by first painting equally spaced colloidal silver patches and then applying copper tape with extended tabs to the silver patches. Strips of masking tape were applied on top of the copper tape to ensure good contact between the electrodes and the specimen. The fully prepared specimen is shown in Figure 24.

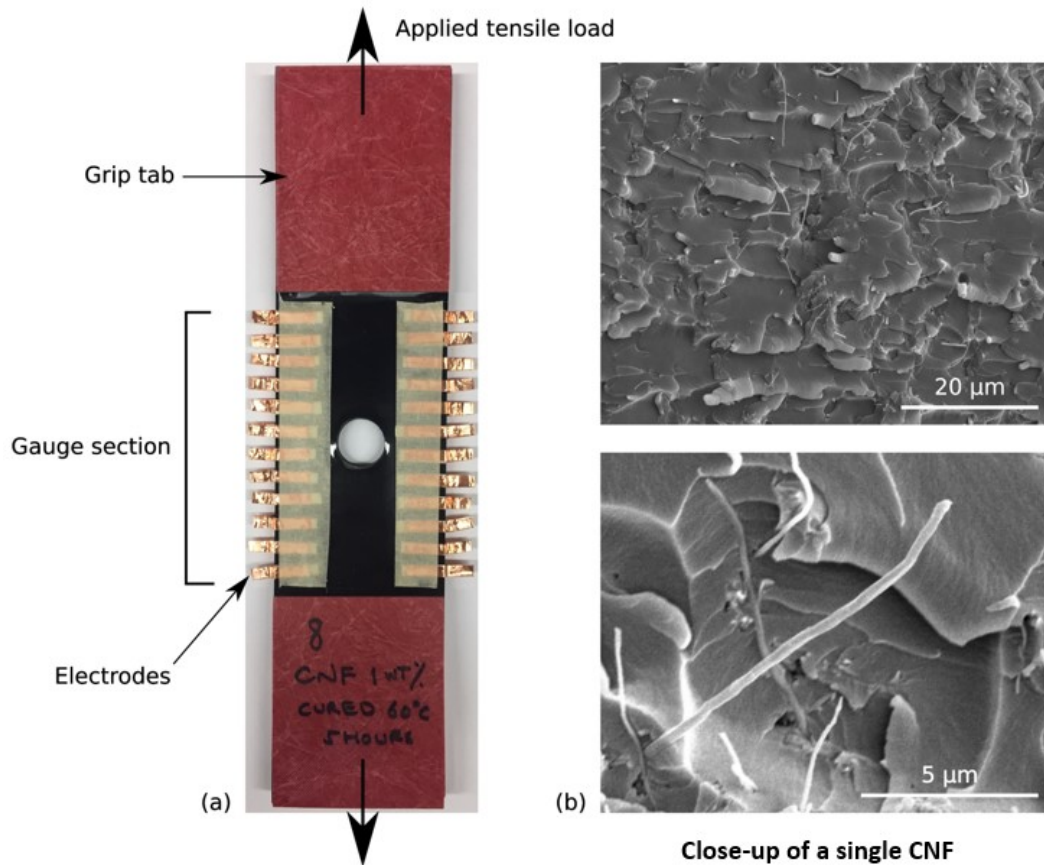


Figure 24: a) Photograph of experimental specimen with electrodes, grip tabs, and gauge section shown. b) SEM images of the underlying CNF network including a close-up of a single CNF.

The specimen was then mounted onto an Instron 8801 load frame and the tabbed portions were fully gripped. The electrodes were connected to a Keithley 6221 current source and a National Instruments PXIe-6368 DAQ to measure the electrode voltages. An ‘across’ scheme was used for the injections, where current was injected between the first pair of opposing electrodes and voltage differences were measured between the remaining opposing electrode pairs. The current injection was then moved to the next opposing electrode pair and voltage differences between the remaining opposing electrode pairs were again measured. This was repeated until all opposing electrode pairs on the gauge section had received one current injection. This scheme was used to collect one set of voltages from the specimen in its undeformed configuration using a current magnitude of $10 \mu\text{A}$. Tensile displacements of $d = 0.25 \text{ mm}$, 0.50 mm , and 0.75 mm were then applied to the specimen and voltages

were collected in each deformed configuration using the same injection scheme and current magnitude.

The specimen was then dismantled from the load frame and the electrode connections were removed. The gauge section was sprayed with white paint and a dotted speckle pattern was applied using a roller dipped in black ink. The specimen was then mounted onto the load frame again and the tabbed portions were full gripped. A Correlated Solutions digital image correlation (DIC) camera system with a 5 MP resolution was set up and the cameras were focused on the gauge section. DIC data was collected as the specimen was loaded in tension at a constant rate of 1.5 mm/s until failure occurred in the gauge section.

6.4.2 Piezoresistivity model

As mentioned previously, the piezoresistive inversion process requires a suitable piezoresistivity model. That is, the goal of the inversion process is to find a strain field that, when supplied to the piezoresistivity model, gives rise to the same boundary voltage-current response as observed experimentally. For this, we make use of an analytical piezoresistivity model that was originally developed by Tallman and Wang (Tallman & Wang 2013). In this model, the conductivity of a nanocomposite is predicted by Equation (54) as shown below and based on the model of Takeda et al. (Takeda, Shindo, Kuronuma & Narita 2011).

$$\gamma_c = \gamma_m + \frac{4Pv_f l_f}{3\pi\lambda_1^2 d_f^2 \left(\frac{4l_f}{\pi d_f^2 \gamma_f} + \frac{h^2 t}{Ae^2 \sqrt{2m\phi}} \exp\left\{ \frac{4\pi t}{h} \sqrt{2m\phi} \right\} \right)} \quad (54)$$

Above, γ_c is the composite conductivity, γ_m is the matrix conductivity, γ_f is the nanofiller conductivity, P is the percolation probability, v_f is the nanofiller volume fraction, l_f is the nanofiller length, d_f is the nanofiller diameter, λ is the nanofiller waviness ratio, h is Planck's constant, e is the charge of an electron, m is the mass of an electron, ϕ is the potential barrier height felt by a tunneling electron, and t is the average inter-nanofiller separation distance. Conductivity changes are predicted by expressing these model parameters as a function of the infinitesimal strain tensor which is done via excluded volume theory of percolation. Thus,

for a given and arbitrary strain state (i.e. given any strain tensor), the new conductivity of the nanocomposite can be predicted. This model was later modified by Tallman and Wang (Tallman & Wang 2016) to ensure differentiability.

6.5 Deep learned ERT tomography framework

6.5.1 Overview

In this section, we firstly introduce the formulation of deep learned frameworks utilizing NNs followed by providing the rationale of selecting NNs for this investigation. These frameworks aim at directly mapping absolute boundary voltage measurements (V) to first principal strain (ϵ_p) and stress (σ_p) distributions. We select the first principal strain and stress because they are good metrics of material failure for the CNF/epoxy material system. To more clearly distinguish the proposed NN framework from existent genetic algorithm (GA)-based methods of piezoresistive inversion (Hassan & Tallman 2020*b*), Figure 45 shows the flowchart of determining the mechanical states of the structures via solving the inverse ERT problem and computing GA and figure 26 shows the proposed deep learned framework. The proposed deep learned framework can therefore be succinctly written as

$$N_\epsilon(V) \rightarrow \epsilon_p \tag{55}$$

$$N_\sigma(V) \rightarrow \sigma_p \tag{56}$$

where $N_\epsilon(V)$ and $N_\sigma(V)$ represent the learned NN operators used for predicting ϵ_p and σ_p distributions, respectively. In order to train NNs and learn the embedded mechanical relationships within Equations (55) and (56), an integrated mechanical model needs to be included to generate appropriate training data. This model is introduced in Section 5.1.

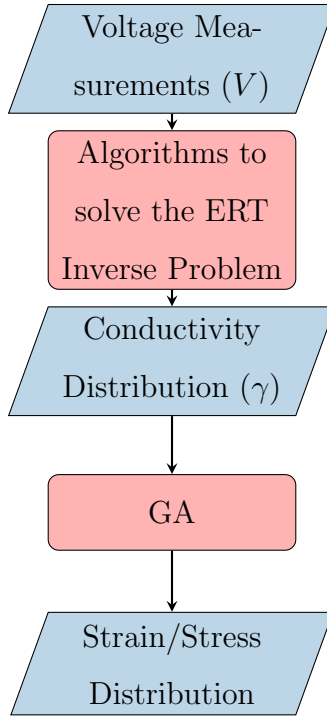


Figure 25: Flowchart of determining the mechanical states via ERT and a GA.

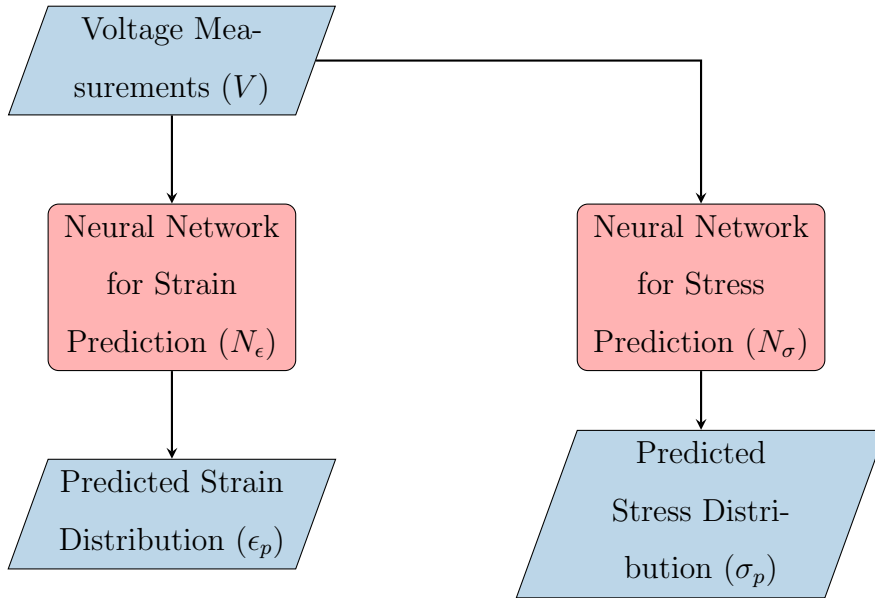


Figure 26: Flowchart of the proposed deep learned framework.

6.5.2 Selection of regression based machine learning approaches

In this subsection, we discuss the rationale behind the selection of the proposed (NN) framework. In a machine learning context, the pattern recognition tasks in this paper are categorized as regression tasks. There are several approaches which are suitable for regression

tasks such as following: (a) linear regression algorithm, (b) logic-based regression models such as boosted decision tree (BRT) regression and random forest (RF) regression, (c) support vector machines (SVMs) and (d) feed-forward artificial neural networks. Linear regression algorithms primarily aim to recognize linear relationships between inputs and outputs based on mean value distributions (Maulud & Abdulazeez 2020). However, the patterns in Equations (55) and (56) are highly non-linear, hence linear regression algorithms are inappropriate for this work. In addition, linear regression algorithms have been outperformed by other regression techniques when evaluated on other regression tasks (Baharvand, Joza-ghi, Fatahi-Alkouhi, Karimzadeh, Nasiri & Lashkar-Ara 2020, Smoliński & Radtke 2017). For logic-based approaches such as BRT and RF, the accuracy of such algorithms has been proven to be affected by the discretization in the input feature (An & Cercone 1999). However in our proposed framework, discretization of the voltage measurements might not be the most suitable approach.

Additional studies have shown that SVMs and ANNs can both yield accurate results when being validated against different datasets while SVMs shows more robust performance than ANNs (Niu, Feng, Feng, Min, Cheng & Zhou 2019, Shirzad, Tabesh & Farmani 2014). However, SVM’s computational cost increases quadratically with increasing data sizes due to solving quadratic programming problems during training (Ertekin & Hopper 2006). This drawback remains as a factor inhibiting SVMs from pragmatic applications. Furthermore, implementations can use early stopping, network-reduction and regularization to prevent over-fitting during NNs’ training to improve their generalisation performance (Ying 2019). Taken the analysis above together, we select NNs for the regression tasks herein, namely for attaining $N_\epsilon(V)$ and $N_\sigma(V)$ due to their overall accuracy, improved generalisation and large numbers of well-established training tools/toolboxes.

6.6 Training Data Acquisition and Neural Network Methodology

In this section, we first introduce the integration of the mechanical elastic FE model, CEM and piezoresistivity model used for training data generation. Then, samples of first principal strain and stress distributions used for training are shown. After that, we present the NNs’ architectures, training hyper-parameters and the training error curves for both trained NNs.

6.6.1 Integration of the elastic FE model, CEM and piezoresistivity model

In this work, we aim to recognize the pattern between boundary voltage measurements (V) and first principal strain distributions (ϵ_p) or stress distributions (σ_p) using NNs. For this, we integrated an elastic FE model, CEM and the piezoresistivity model to generate the training data for NNs. The geometry of the domain was adopted from (Hassan & Tallman 2020*b*). The elastic FE model discretized the experimental specimen without the top and bottom tabs with reference to Table 7. Figure 28 shows the flowchart of the training data generation. Meanwhile, sample first principal strain and stress distributions for training are shown in Figure 29 and 30. The formulation of the FE model is described as follows:

1. The geometry of the experimental domain was discretized using 1576 triangular elements and 870 nodes. 24 electrodes were positioned on both vertical sides of the specimen with uniform spacings. The parameters of the domain adopted for discretization are shown in Table 7. Figure 27(a) shows the mesh discretization of the adapted CNF domain where positions of electrodes are highlighted with reference to Table 7.

Table 7: Geometry and mesh details for the adapted CNF specimen domain.

| Parameter | Value |
|-------------------------|----------|
| Width | 46.5 mm |
| Height | 81.1 mm |
| Electrode spacing | 6.2 mm |
| Electrode width | 9.3 mm |
| Electrode height | 3.175 mm |
| Radius of central notch | 6.2 mm |

2. With FE meshes generated, we adapted CNF material properties from (Hassan & Tallman 2020*b*) with elastic modulus (E) assigned as 2.534 GPa and Poisson ratio (ν) as 0.35. Furthermore, in order to increase the generalisation performance of NNs for predicting the first principal strain and stress fields on CNF materials, the elastic modulus was distributed randomly within the domain. The homogeneous (mean) value of the elastic modulus was assumed to be 2.534 GPa and the elastic modulus was distributed randomly within the range where $0.6E_h < E < 1.4E_h$. The variance coefficients were selected such that the simulated first principal stress and strain distributions have

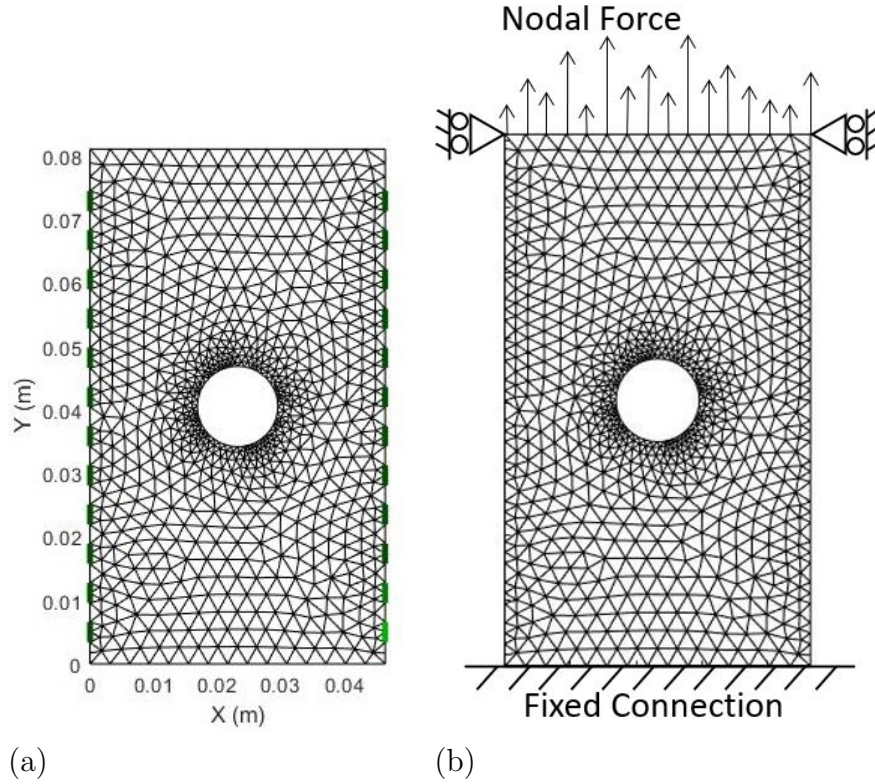


Figure 27: Discretized domain that is used in the integrated model: a) Domain discretization of the gauge section of the CNF/epoxy specimen consisting of 1576 elements and 870 nodes; b) Boundary conditions that are implemented in the elastic FE model. The domain is fixed in x and y directions at the bottom. Displacements are allowed in y-direction on top layer nodes.

larger variance while remaining physically realistic. As a result, E data had blob-like Gaussian randomized spatial distributions, which effectively increased the variance of voltage measurements and the corresponding strain/stress distributions within the training sets.

3. In the elastic FE model, nodal forces were increased incrementally and randomly on top of the domain. The reasons for doing this are as follows: (a) to simulate the plate under incremental tensile forces corresponding to the experiments and (b) to increase the variance of stress/strain distributions within the training sets. Corresponding boundary condition details are shown in Figure 27(b). Forces were applied on the top nodes acting upwards while constrained in the x-direction. Nodes on the bottom of the mesh were fixed in the x and y directions. The maximum forces used in generating the training

data corresponding to the failure displacement in the y-direction adopted from the experiment which was approximately 0.8 mm (Hassan & Tallman 2020*b*).

4. Strain and stress distributions were computed assuming elemental strains and stresses are related using a linear elastic constitutive law. The elemental first principal strains and stresses were then calculated and recorded. After that, the piezoresistivity model developed in (Tallman & Wang 2013) and summarized in Equation 54 was used to calculate the conductivity distributions (γ) based on strain distributions (ϵ). Finally, the conductivity distributions (γ) were inputted to CEM to compute the corresponding voltage outputs (V).

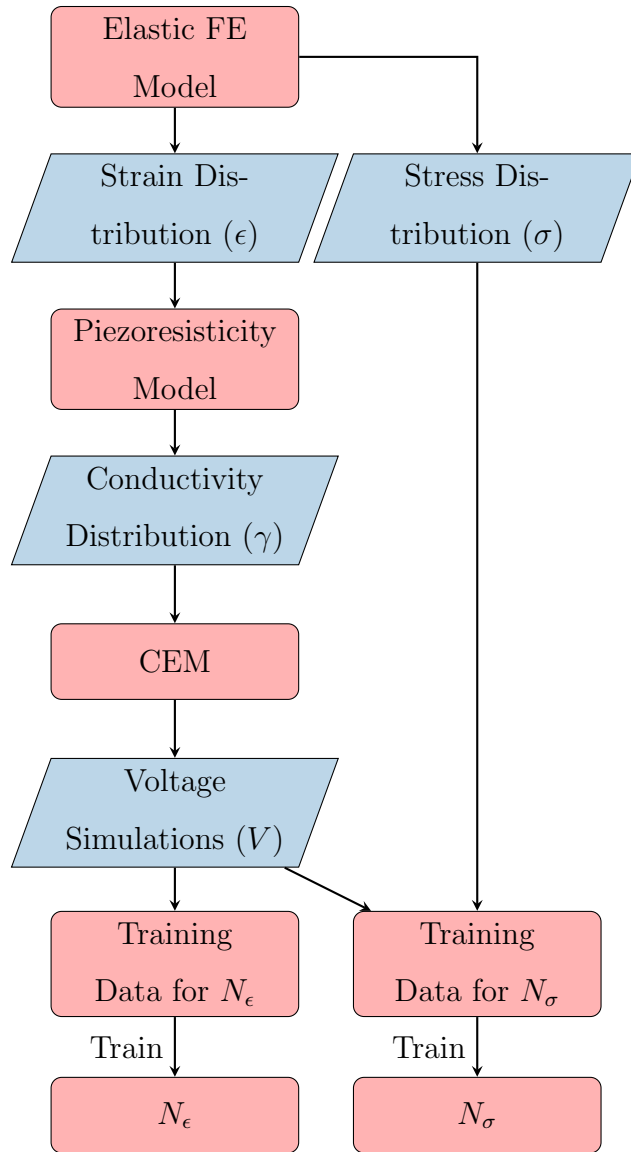


Figure 28: Flowchart of the training data generation path.

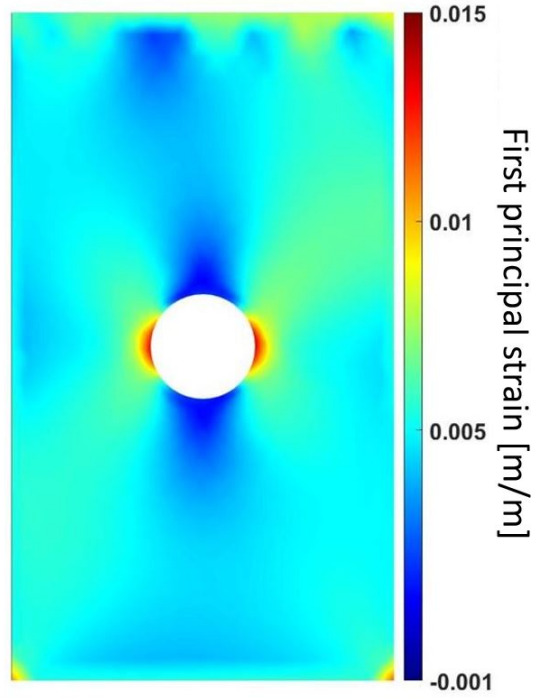


Figure 29: Sample strain distribution within N_ϵ training data.

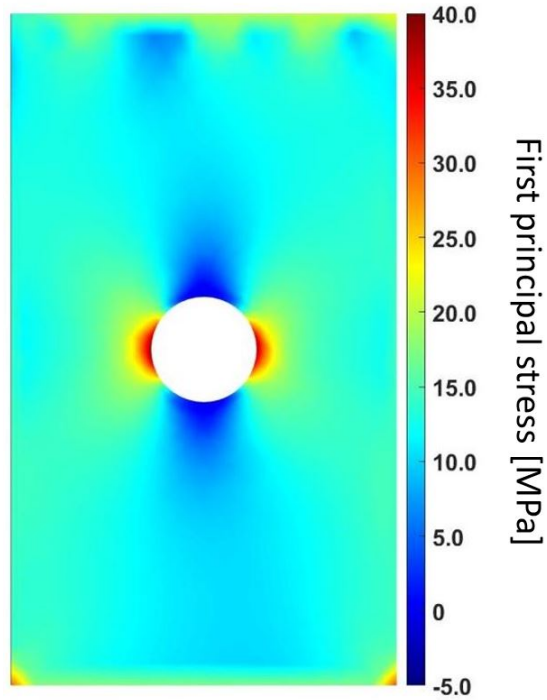


Figure 30: Sample stress distribution within N_σ training data.

6.6.2 Neural network architecture and training

In this section, we present the NNs' architectures and hyperparameters. From the generation of training data, we obtained two sets of training samples which consist of (a) absolute boundary voltage measurements (V) corresponding to first principal strain distributions (ϵ_p) and (b) absolute boundary voltage measurements (V) corresponding to first principal stress distributions (σ_p). Input data used in training the NNs consist of vectors of size 132×1 while the output data are 1576×1 as shown in Table 8 and 9.

In order to increase the performance of NNs' training (and the accuracy of predictions), the training data was pre-processed prior to training. Namely, in order to reduce the modeling error within the training samples, the following error correction methodology was implemented:

$$e_{model} = V_h - V_0 \quad (57)$$

where e_{model} represents the modeling error, V_h are the CEM voltage simulations from an assumed homogeneous and unstressed sample, and V_0 are the experimental voltage measurements taken from the unstressed reference state. The modeling error was calculated independently as the difference between each index in V_h and V_0 , to be more specific, from the first entry to the 132nd entry of both these measurement vectors. Homogeneous assignment of the domain's conductivity was made based on prior experimental information where γ_0 is 4.857×10^{-4} S/m. Then, we subtracted e_{model} from voltage simulations in the training data regardless of the forces perturbations to correct and, correspondingly, reduce the modeling error within the samples. As a result, the training samples were better fitted with the experimental measurements.

After correcting model errors, we pre-processed the training samples by eliminating superfluous samples consisting of only zero strain/stress entries. In this way, we can prevent the NNs from being heavily biased towards non-displacement cases. Thirdly, we designed the NNs' architecture and chose the hyper-parameters which yielded the most accurate predictions on the validation sets. Summaries of training sets for N_ϵ and N_σ , number of training samples,

architectures and training hyperparameters are shown in Table 8 and 9. The finalized N_ϵ was comprised of one input layer and three fully connected layers with 100 neurons each followed by three dropout layers, respectively. Hyperbolic tangent (Tanh) activation functions were applied on all layers to take advantage of their smooth mapping capabilities. Meanwhile, the finalized N_σ network has the same architecture and activation functions as N_ϵ , however with increased number of neurons to 500 per hidden layer. The reason that N_σ was designed with more neurons than N_ϵ reflects the discrepancy in input to output mapping sizes.

Table 8: Summary of the ANN architecture (N_ϵ) for predicting strain distributions.

| Input of V with size (132,1) | | | |
|---|-------------|-------------------|---------------------|
| Total number of training samples: 5000 | | | |
| Layer (Type) | Activations | Learnable Weights | Activation Function |
| Input layer | 132 | - | - |
| Fully connected layer | 100 | 13200 | Hyperbolic tangent |
| Dropout (dropout rate : 50%) | 100 | - | - |
| Fully connected hidden layer | 100 | 13200 | Hyperbolic tangent |
| Dropout (dropout rate : 50%) | 100 | - | - |
| Fully connected hidden layer | 100 | 13200 | Hyperbolic tangent |
| Dropout (dropout rate : 50%) | 100 | - | - |
| Output layer | 1576 | 157600 | Hyperbolic tangent |
| Output of ϵ with size (1576,1) | | | |

Table 9: Summary of the ANN architecture (N_σ) for predicting stress distributions.

| Input of V with size (132,1) | | | |
|---|-------------|-------------------|---------------------|
| Total number of training samples: 10000 | | | |
| Layer (Type) | Activations | Learnable Weights | Activation Function |
| Input layer | 132 | - | - |
| Fully connected layer | 500 | 66000 | Hyperbolic tangent |
| Dropout (dropout rate : 50%) | 500 | - | - |
| Fully connected hidden layer | 500 | 250000 | Hyperbolic tangent |
| Dropout (dropout rate : 50%) | 500 | - | - |
| Fully connected hidden layer | 500 | 250000 | Hyperbolic tangent |
| Dropout (dropout rate : 50%) | 500 | - | - |
| Output layer | 1576 | 788000 | Hyperbolic tangent |
| Output of σ with size (1576,1) | | | |

To more comprehensively inform on the training process, training was terminated when the loss function ceased to decrease more than 10% within 500 epochs. The former indicates that gradient descent algorithm has satisfactorily minimized the loss described in Equation (42). This selection was made based on the realization that training after this point may result in over-fitting the data. The minimization of the loss functions for N_ϵ and N_σ are shown in Figures 31 and 32. In these plots, we observe significant loss at the start of the training followed by sharp reduction and finally reached a steady state. In the following section, we will provide results and discussion on predictions made by the trained networks.

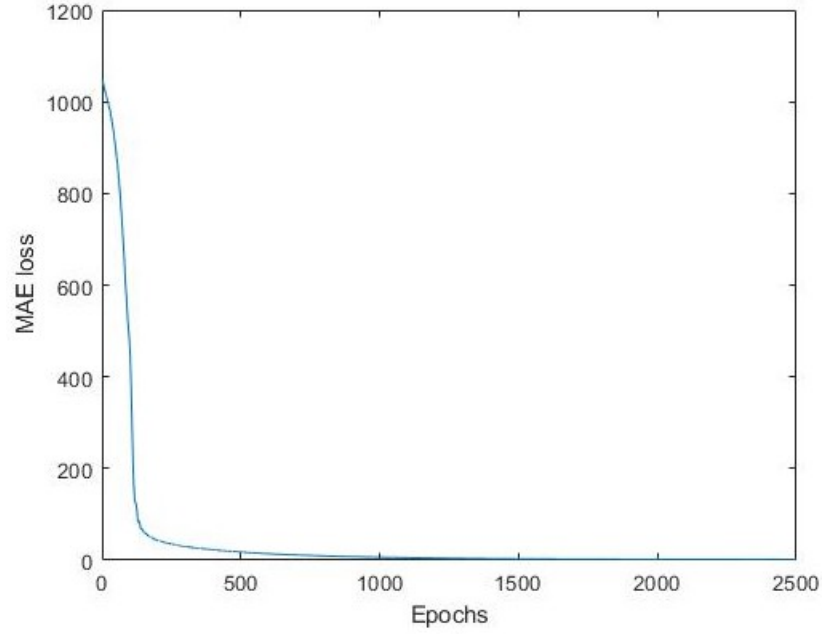


Figure 31: Loss function minimization for the predictor N_ϵ .

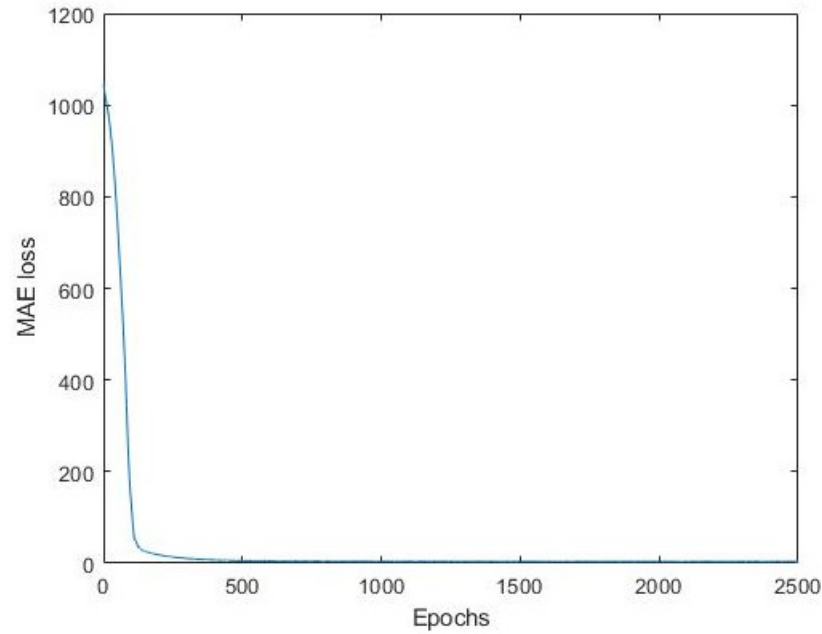


Figure 32: Loss function minimization for the predictor N_σ .

6.7 Results and Discussion

In this section, we begin by assessing the feasibility of the trained NNs for predicting stress and strain fields. This is first tested using simulated data followed with experimental data.

Following, we analyze the results, provide a discussion and lastly consider potential future research.

6.7.1 Results

The predictive results from N_ϵ and N_σ are shown in Figure 33(a) and (c). The corresponding simulated principal strain and stress distribution are shown in Figure 33(b) and (d). These two results was chosen randomly from the datasets which was not used to train the corresponding NNs, the force and elastic applied was randomized as explained in section 6.6.1. We first observe strain and stress concentrations on top of the domains which are caused by the excess incremental nodal forces during the data generation process. As a whole, the predicted results show similar strain and stress distributions in comparison to the simulated data. However, it can be seen that N_ϵ overpredicts the strain concentration near the circular notch while predictions from N_σ underpredicts the stress concentration on the left-top side of the domain. This can be caused by (a) minimization of the MAE loss function with regularization is highly unlikely to reach zero, hence the prediction error are always present in the results and (b) lower elastic modulus values on nodes due to the random generation of elastic modulus distributions.

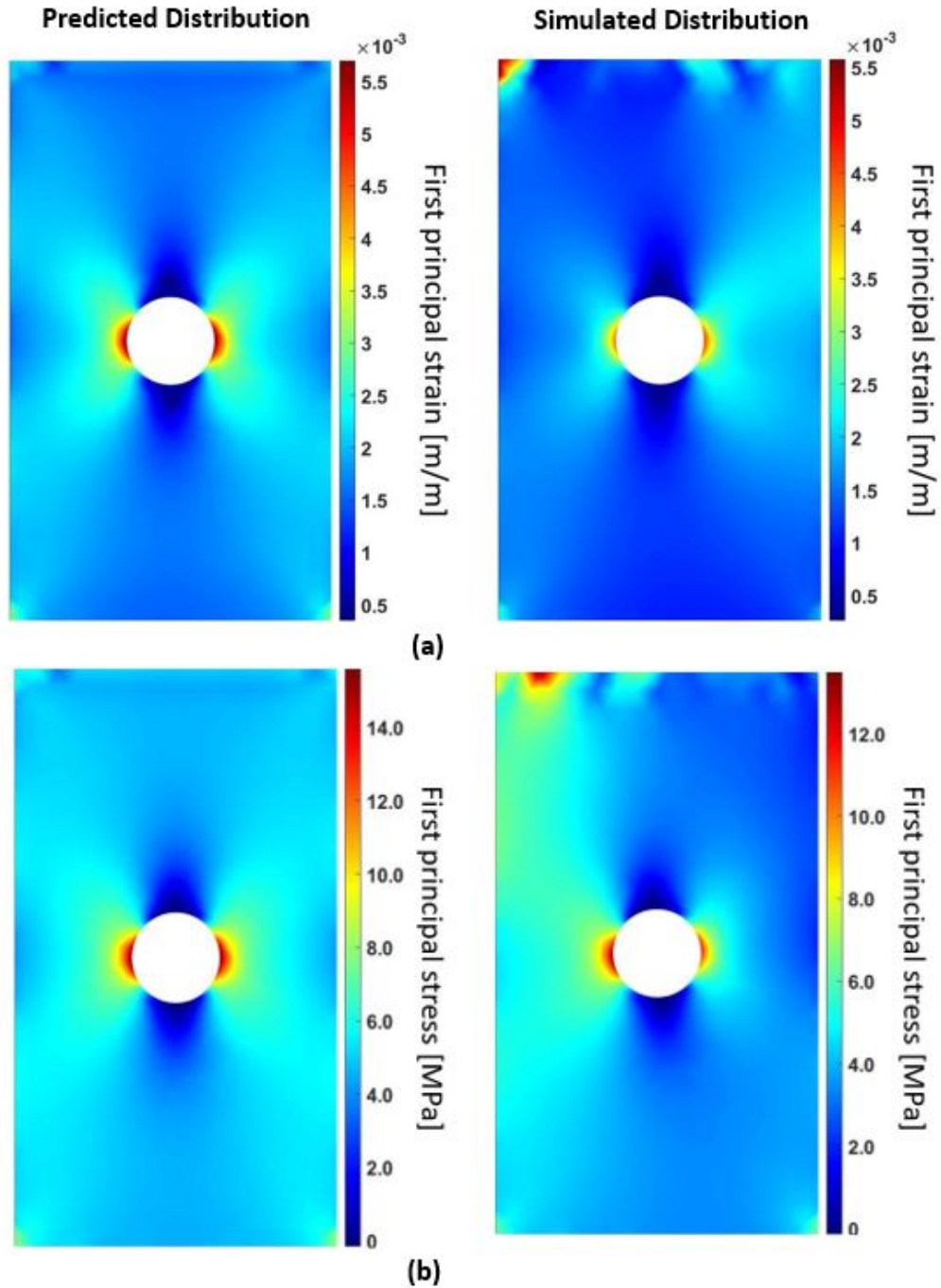


Figure 33: Comparison between the predicted strain and stress distributions and their corresponding simulation samples: a) Prediction of the strain field (left) and simulated strain field from the integrated model (right); b) Prediction of the stress field (left) and simulated stress field from the integrated model (right).

We then validate the NNs predictive performances on the experimental data. The NNs' strain and stress predictions are shown in Figure 34. To corroborate the predictions, Figure 34 also shows the DIC reconstructions from the experiments considering different axial displacements. In this qualitative feasibility study, we observe that the NNs' predictions exhibit similar strain and stress distributions compared with DIC reconstructions. Strain and stress concentrations can also be observed around the notch which are consistent with the DIC results. In addition, it is worth noting that NNs' predictions show correct rate of growth of strain and stress distributions corresponding to different loading stages. Closer inspection of the predictive results show symmetrical first principal strain and stress distribution patterns which are expected based on the applied boundary conditions. Quantitatively speaking, the maximum predictive first principal strain is 17.3% higher than DIC reconstructions while the maximum predictive first principal stress is 4.5% higher than DIC reconstructions. Discrepancy between the prediction and DIC results can potentially be reduced by optimizing the NNs' hyperparameters. Summarily, in taking the results together, we can observe that the proposed NNs can qualitatively predict the first principal strain and stress distributions directly without solving the ERT inverse problem. Quantitatively speaking, N_σ yields accurate predictions within 5% error margin while N_ϵ outputs less accurate results. The reasons that potentially caused this observation are discussed in the following section.

The computational time for predicting the strain/stress distribution via both methods are recorded in Table 10. We carry out four independent runtime tests via NNs and compare them with the runtimes via *ERTplusGA*. Significant computational time reduction can be observed from Table 10. In order to further compare the results of both methodologies. We record the average values of the first principal strain ($\bar{\epsilon}_p$) and stress ($\bar{\sigma}_p$) considering different displacement cases in Table 11. Firstly, results yielded via *ERTplusGA* are down-sampled and mapped on the same FEA meshes that are used for NNs' predictions. Secondly, average values are then computed based on the interpolated strain and stress vectors. The same process is followed when computing the L_2 norm of first principal strain ($\|\epsilon_p\|^2$) and stress vectors ($\|\sigma_p\|^2$) from both methodologies. Corresponding results are recorded in Table 12.

Table 10: Computation runtimes for predicting strain and stress distributions using NNs and ERT plus GA considering different displacement cases.

| - | Runtimes via NNs (s) | | | | Runtimes via ERT plus GA (s) | | | |
|---------------------|-----------------------------|---------------|---------------|---------------|-------------------------------------|---------------|---------------|---------------|
| Displacement | Test 1 | Test 2 | Test 3 | Test 4 | Test 1 | Test 2 | Test 3 | Test 4 |
| 0.25mm | 0.073 | 0.084 | 0.056 | 0.030 | 4440 | 3480 | 3300 | 3300 |
| 0.50mm | 0.029 | 0.028 | 0.031 | 0.029 | 4680 | 3840 | 3600 | 3540 |
| 0.75mm | 0.028 | 0.031 | 0.031 | 0.028 | 4500 | 4200 | 4080 | 4080 |

Table 11: The average first principal strain ($\bar{\epsilon}_p$) and stress distribution ($\bar{\sigma}_p$) obtained via NNs and ERT plus GA considering different displacement cases (d).

| - | $\bar{\epsilon}_p$ considering different cases | | | $\bar{\sigma}_p$ considering different cases (MPa) | | |
|--------------------|--|---------|---------|--|---------|---------|
| Methodology | 0.25 mm | 0.50 mm | 0.75 mm | 0.25 mm | 0.50 mm | 0.75 mm |
| NNs | 0.0027 | 0.0043 | 0.0064 | 4.46 | 9.24 | 14.63 |
| ERT plus GA | 0.0061 | 0.0043 | 0.0077 | 15.82 | 11.38 | 21.39 |

Table 12: The L_2 norm of first principal strain ($\|\epsilon_p\|^2$) and stress distribution ($\|\sigma_p\|^2$) obtained via NNs and ERT plus GA considering different displacement cases (d).

| - | $\ \epsilon_p\ ^2$ considering different cases | | | $\ \sigma_p\ ^2$ considering different cases (MPa) | | |
|--------------------|--|---------|---------|--|---------|---------|
| Methodology | 0.25 mm | 0.50 mm | 0.75 mm | 0.25 mm | 0.50 mm | 0.75 mm |
| NNs | 0.0848 | 0.1357 | 0.2027 | 144 | 297 | 470 |
| ERT plus GA | 0.2664 | 0.1314 | 0.2419 | 712 | 357 | 692 |

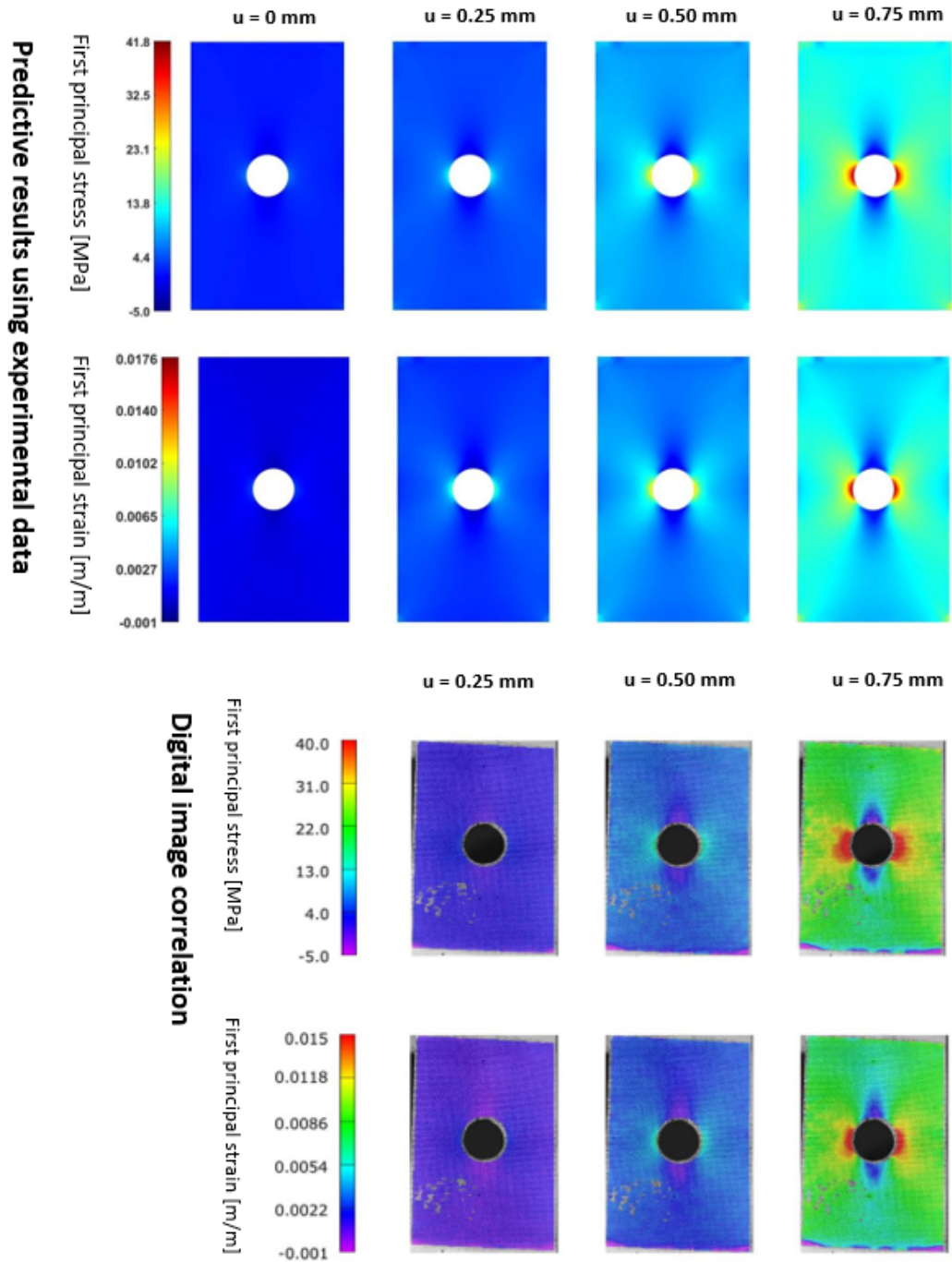


Figure 34: Neural network predictions of experimental data (top two rows) and the DIC reconstructions (bottom two rows) considering different displacement states (Hassan & Tallman 2020b).

6.7.2 Discussion

This paper conducts the feasibility study of the proposed methodology which is affirmed qualitatively and quantitatively via simulation and experimental data in the preceding sections. Indeed, as corroborated in the previous subsection, we can observe the efficacy of using NNs in directly predicting the first principal strain and stress fields based on ERT voltages measured from CNF materials. The main advantages of the proposed methodology are as follows: (a) reduction in computational costs, having applications in continuous monitoring in pragmatic monitoring frameworks and (b) no prior information such as forces, boundary conditions of the members are required as inputs for NN prediction. Similar features could enable this methodology to be applied in complex environmental and operational conditions. For example, by considering elements that are subjected to varying atmospheric conditions during simulations. To more closely investigate the feasibility of NNs, we will begin by evaluating findings during data processing and network training which improve the accuracy and generalisation of the proposed NNs followed by the insight for future research.

Firstly, we want to address the error correction methodology used to reduce the modeling error prior to training. As shown in Figure 35, we can observe discrepancies between the simulated voltage measurements of homogeneous background estimation and the experimental measurements of the reference state. These discrepancies mainly result from (a) geometrical electrode modeling errors and (b) the elastic FE modeling errors. It is worth noting, regarding (a), that the locations of electrodes are assumed to be stationary regardless of the specimen's elongation. However, in experimental conditions, the locations of electrodes change proportional to the CNF plate displacement. As we can observe from Figure 36, this modeling error correction process mitigates the discrepancies which could increase the accuracy of NNs' predictions when validating experimental results.

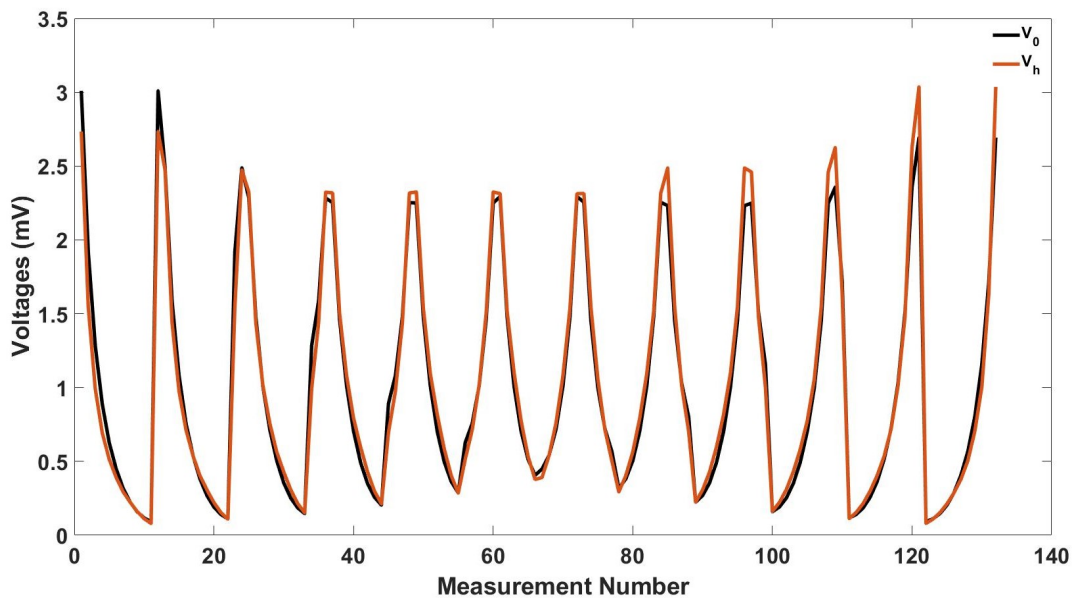


Figure 35: Simulated homogeneous voltages and experimental voltage measurements prior to error correction.

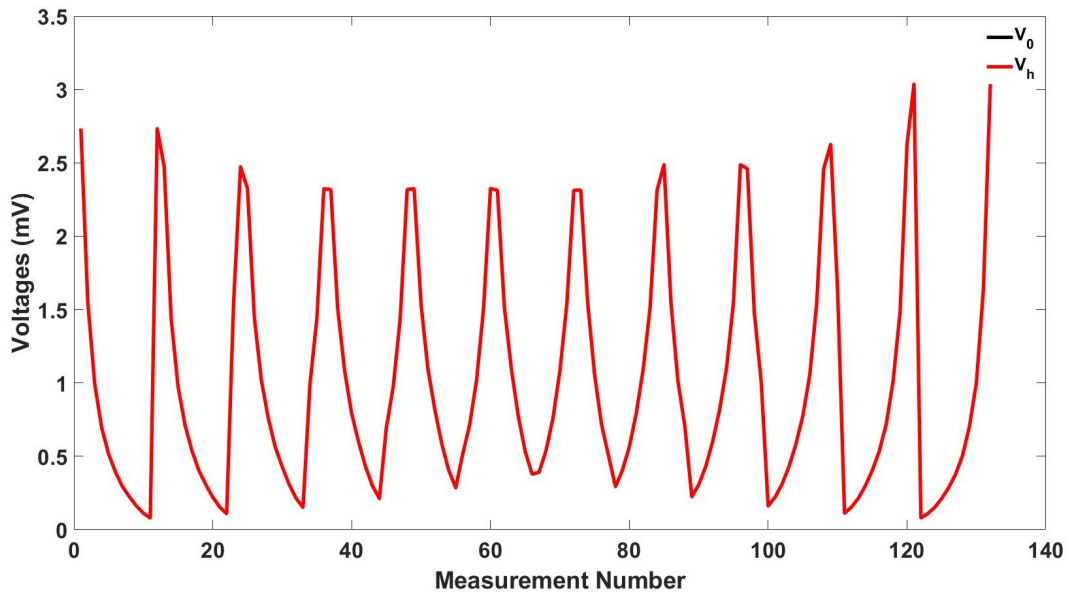


Figure 36: Simulated homogeneous voltages and experimental voltage measurements after error correction.

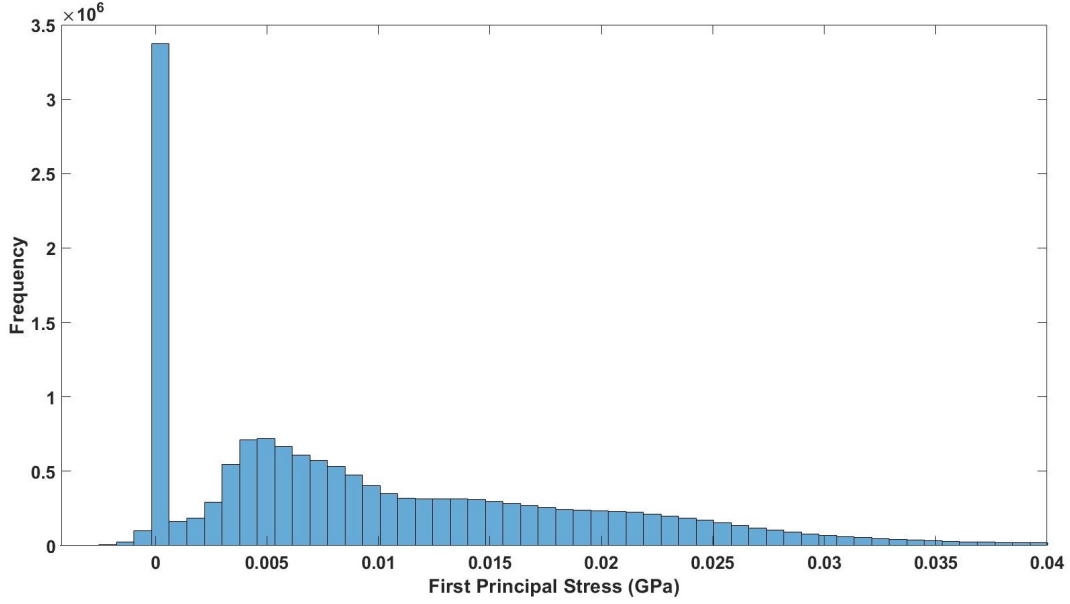


Figure 37: Histogram plot of stress training samples prior to data processing.

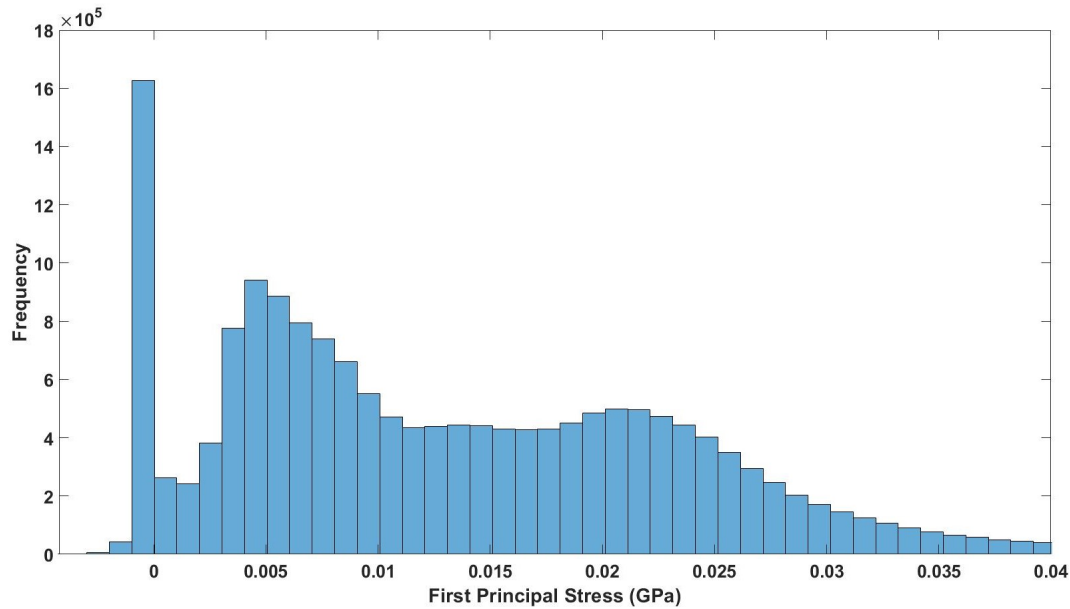


Figure 38: Histogram plot of stress training samples posterior to data processing.

Furthermore, as previously noted, we pre-process the training samples prior to the training process. As shown in Figure 37, training samples are heavily biased towards the ‘zero-displacement’ cases. This is caused by the generation of training samples originating incrementally from the ‘zero-displacement’ cases where no or minimal forces are applied on the

model. Hence the entries in strain and stress matrices consist of near-zero entries. Herein, we pre-process the training samples by decreasing the total number of ‘zero-displacement’ samples with trial and error. Frequency on y-axis represents the number of occurrences of each number within the whole training data set. As a result, Figure 38 shows the histogram plot after processing. Although the spike on zero is still present, we can observe the training samples are now less biased towards ‘zero displacement’ cases compared to Figure 37. This process proves to be effective during training and yielding more accurate results, however excess elimination of ‘zero displacement’ samples may result in poor generalization of the NNs.

However, despite the advantages stated above, the performance of NNs is not always satisfactory against certain simulation samples and N_σ yields more accurate results than N_ϵ when validating against experimental data. To explain this, we first note that better performance from N_σ results from the fact that N_σ has more learnable weights than N_ϵ . Though theoretically by increasing the model complexity of N_ϵ , we could obtain a network that yields more accurate predictions, we are at the risk of over-fitting the data. This trade-off between the generalisation and accuracy of the corresponding NNs also caused the errors when predicting on simulated measurements. Hence a rigorous methodology to find the balance point between the generalisation and accuracy for simulated and experimental data at the same time could be a point of potential research interests. The predictive results from simulations show larger error on domain boundaries. This is mainly due to the FEA model used in this paper to generate training samples has high sensitivity to error at top and corner boundary locations as shown in Figure 33. In further research, an efficient posterior error estimation technique can be applied on the FEA model to reduce the error in FEA solutions (Ainsworth & Oden 1997). As a result, we could have samples with reduced boundary modeling error which could increase the accuracy of predictive results at the boundaries.

To directly compare the computational cost of proposed and reference methodology, we can observe the significant reduction of runtimes of predicting the strain and stress distribution via NNs than *ERTplusGA* in Table 10. This reduction could enable a well-trained neural network to potentially provide real time strain/stress reconstructions under the specific

boundary conditions that is trained on. Furthermore, we could observe that NNs yield lower average and L_2 norm values than the *ERTplusGA* methodology as shown in Table 11 and 12. In addition, both average and L_2 norm values shows larger difference when displacement is at 0.25 mm. This could partially be due to the error produces while interpolating the *GAplusERT* results. We want to address that Table 11 and 12 only provide the direct comparison between two methodologies but not indicate the accuracy of either methods.

In addition, the proposed methodology is application specific. Namely, that the methodology, at present, can only be applied on smart materials which have known piezoresistivity properties since the mapping between conductivity and strain distributions rely on the piezoresistivity model. Herein, potential research can aim at conducting feasibility studies on other smart materials following the proposed methodology. In addition, since the same boundary conditions are applied on all training samples, NNs in this paper can only yield accurate strain/stress distributions under those specific boundary conditions. In further research, one could either train different NNs based on the expected boundary conditions or adding training samples with different boundary conditions to utilize the advantages of the proposed methodology.

Lastly, since the experimental data were collected in a controlled lab environment, the environmental and operational conditions of this system are assumed to be stable. As a result, the changes in the input data are assumed to be directly associated with the changes of the strain distributions. However, when SHM is applied in field applications, it is imperative for the proposed framework to incorporate any measurement changes caused by the environmental and operational conditions. Hence, future research will be focused on handling robust conditions using advanced data processing approaches (e.g. filtering, cleansing, normalizing, etc.) for measurements used in training stress/strain predictive networks.

6.8 Conclusion

This paper sets out to assess the feasibility of incorporating neural networks for directly predicting the first principal strain and stress distributions from ERT voltages measured from CNF materials. The findings indicate that the proposed framework can qualitatively

predict the principal strain and stress distribution predictions on various experimental voltage measurements. More importantly, the proposed framework may be used to significantly reduce the computational time for the predictions of strain and stress distributions. This advantage may lead to much lower operational costs in pragmatic applications. However, the current study is limited by the absence of approaches to rigorously optimize the trade-off between generalisation and accuracy. Further work needs to be done to research NNs which could yield more quantitatively accurate results on experimental data. In conclusion, the feasibility of proposed framework was affirmed qualitatively with simulation and experimental data. Discussion and future research interests were proposed for further development of the proposed methodology.

6.9 Acknowledgement

The authors gratefully thank Professor RB Pipes, Dr. Benjamin Denos and Dr. Rebecca Cutting for their assistance with DIC performed at the Composites Manufacturing and Simulation Center at Purdue University. Dr. Christopher Gilpin in the Purdue Electron Microscopy Facility is also thanked for performing the SEM imaging. Thanks to Adrien Gallet for insightful discussions on this paper.

7 Data-driven superresolution of numerical simulations and experimental measurements

Authorship: Liang Chen, Shan-Shan Huang, Dong Liu, and Danny Smyl

Submitted Journal: Inverse Problem

7.1 Abstract

In situations where time or computing resources are limited, implementation of reduced order numerical models remains attractive in engineering. Unfortunately, this pursuit is generally associated with an unavoidable trade-offs in accuracy, resolution, and/or information. Herein, we address this issue by proposing the use of data-driven fully connected neural networks for increasing the fidelity of numerical solutions – a process henceforth referred to as learned superresolution (SR). In the examples tested, the feasibility of using trained fully connected networks to conduct SR (using reduced order finite element solutions to simulate higher-order *hp* solutions) is demonstrated. For this, trained SR networks are first tested computationally in the context of mechanical simulations and later in the context of (inversion-based) experimental nondestructive evaluation. Results indicate the potential feasibility of using proposed SR approach to obtain numerical solution with low fidelity data. Potential uses and paths forward for network-based SR of numerical simulations in engineering and inverse problems are discussed.

7.2 Introduction

Over the past 30 plus years, significant advances in computational science and engineering have been realized (Hughes 2012, Simos 2011). Among the numerical approaches used to simulate physical problems in engineering, the finite element method (FEM) remains pervasive. This is largely owed to FEM’s ability to, for example, approximate differential equations in domains of arbitrary geometry (Reddy 2019), handle complex boundary conditions (Surana & Reddy 2016), and readily incorporate computer aided design (CAD) model topology (Foucault, Cuillière, François, Léon & Maranzana 2008). It is then no surprise that the FEM has become (and still is) a highly active research area. Among the numerous advances emerging

from this field, the ability to improve FEM approximations via discretization and/or refinement has proven invaluable from a pragmatic point of view (Zhang, Gain & Norato 2020, Areias, Reinoso, Camanho, De Sá & Rabczuk 2018, Yu & Bui 2018, Hartmann, Held, Leicht & Prill 2010, Azócar, Elgueta & Rivara 2010). Especially, the development of discretization size (h), order of approximation polynomial (p), and hp refinement has enabled highly accurate modeling of physical problems (Bagwell, Ledger, Gil, Mallett & Kruip 2017, Bell & Surana 1994, Paszyński, Kurtz & Demkowicz 2006, Houston, Schwab & Süli 2002, Oden, Duarte & Zienkiewicz 1998). In a similar vein, the field of (physical model-based) inverse problems has also benefited from implementations of improved accuracy hp -adaptive FEM models via the abatement of modeling errors (Yeo, Hwang, Liu & Kalagnanam 2019, Smyl & Liu 2019b, Hakula, Hyvönen & Tuominen 2012, Ledger 2012).

The crux of adopting increasingly accurate numerical models in engineering and as forward models in inverse problems is the increased computational expense. This observation is closely related to the so-called “curse of dimensionality” that has plagued (conventional) numerical solution approaches to partial differential equations (Grohs, Hornung, Jentzen & Von Wurstemberger 2018). To complicate matters more, recent works in physical model-based inverse problems have shown that there may exist a “Goldilocks Zone” whereby the most suitable forward model is neither overly accurate nor inaccurate (Burger, Korolev & Rasch 2019, Smyl & Liu 2019b). Practically, a solution to the former issues might be efficiently addressed using reduced-order numerical models, which are designed to be both fast and *sufficiently* accurate for the problem at hand (Nouy 2010, Benner, Gugercin & Willcox 2015, Amsallem & Farhat 2008). However, in many cases, reduced order models are used when insufficient computing resources and/or time dictate model accuracy. In such situations, the unfortunate trade-off is simply to reduce model complexity (e.g. reducing nodes and elements in a FEM discretization); thus, systematically tailoring model accuracy is infeasible in these circumstances. FEM analysis which is a common practice for mechanical modelling also suffers from the “curse of dimensionality”; in an ideal world, a FE model with desired spatial resolution and accuracy could be selected independent of computational resources and time. However, in constrained environments where highly accurate FE models are needed,

avoiding the “curse of dimensionality” using conventional FE approaches may be unavoidable. As such, a practical solution to this problem is needed.

In this work, we are inspired by recent works utilizing neural networks (NNs) to circumvent the aforementioned challenges related to numerical computation, complexity, and dimensionality (Jentzen, Salimova & Welti 2018, Grohs, Hornung, Jentzen & Von Wurstemberger 2018). Herein, we address these challenges by proposing the use of data-driven NN mappings from reduced order FE solutions to higher order solutions. Owing to similarities in learned superresolution (SR) frameworks already developed in imaging contexts (e.g. (Jiang, Wang, Yi & Jiang 2020, Jiang, Wang, Yi, Wang, Lu & Jiang 2019, Molini, Valsesia, Fracastoro & Magli 2019)), we also categorize this approach within the family of SR. To this end, the overall aim of the proposed SR approach is to (a) “seed” NNs using low fidelity, yet physically-realistic, inputs and map to solutions containing higher resolution and accuracy and (b) enable ease of pragmatic application in engineering and inverse problems settings. In recent studies, Electrical Resistance Tomography (ERT) emerged as an imaging modality for non-destructive testing (NDT). However, high fidelity ERT reconstructions suffers from “curse of dimensionality” due to solving the ill-posed ERT inverse problem (Chen, Gallet, Huang, Liu & Smyl 2022). Herein, in this paper we aim to reduce the computational cost of applying pragmatic ERT applications using the proposed deep learned SR.

The paper is structured as follows. First, we introduce the background of superresolution along with the description of the mechanical study followed by introduction of the electrical resistance tomography (ERT) inverse problem, then we propose the learned SR approach as well as its implementation in the inverse problems, and then we detail the selection of the NN architectures used. Following, the proposed approach is tested numerically considering SR of mechanical simulations. Next, we trial the method using experimental data in the context of nondestructive evaluation. Finally, discussion and conclusions are presented.

7.3 Data-driven superresolution of reduced order models and implementation in inverse problems

In this section, we propose the data-driven SR approach used to improve the resolution and accuracy of reduced order numerical models. Following, we describe potential implementations of the SR approach in improving the FEM results with low fidelity data via a mechanical simulation study. Then we explore the feasibility of using SR to solve inverse problems. Lastly, the selection of NN architectures for SR is discussed.

7.3.1 Approach to superresolution of reduced order models

We are herein interested in developing data-driven mapping from reduced order numerical solutions to solutions with higher resolution and/or accuracy. Due to their pervasiveness in engineering and inverse problems, we firstly focus on applications of the FEM. In this contextualization, we first consider the following relationship between complimentary FE solutions having the same solution dimensionality

$$u_A = u_R + \epsilon_1 \tag{58}$$

where $u_A \in \mathbb{R}^N$ is an accurate FE solution, $u_R \in \mathbb{R}^N$ is a reduced order FE solution, N is the length of the FE solution vectors, and $\epsilon \in \mathbb{R}^N$ is a non-random model error term (Smyl, Tallman, Black, Hauptmann & Liu 2021).

Since a one aim of our SR approach is to increase the fidelity of simulations, however, we restrict ourselves to mapping solutions where the accurate solution is larger than or equal to the size of the reduced order solution, i.e. we have $u_A \in \mathbb{R}^{N_A}$ and $u_R \in \mathbb{R}^{N_R}$ where $N_A \geq N_R$. Given these, the aim of our data-driven SR approach is to learn the following mapping

$$S(u_R) \rightarrow u_A \tag{59}$$

where the learned function S is generally considered to be nonlinear – via the nonlinearity of the differential equation under consideration and/or the relation between potentially

inhomogeneous FE model parameters and solution. In recent studies, researchers have successfully utilized different types of NNs to achieve the aforementioned aim by learning through multi-fidelity data (Meng & Karniadakis 2020, Liu & Wang 2019, Chakraborty 2021, Raissi, Perdikaris & Karniadakis 2017, Chi, Zhang, Tang, Mirabella, Dalloro, Song & Paulino 2021). Black and Najafi specifically used Multi Fidelity Graph Neural Network (MFGNN) to learn FEM convergence behavior which improved the generalizability over traditional GNNs (?). In this paper, we propose to explore the feasibility of using fully connected neural networks to conduct SR on the 1) displacement data on lower order elements of an mechanical FEM, and 2) up-sample the voltage measurements based on reduced number of electrodes of an experimental ERT inversion problem.

7.3.2 Mechanical simulation study

In this section, we introduce the simulation set up of the discretized mechanical scenario with FEM to explore the feasibility of the proposed SR approach. Firstly, a square domain of $1m \times 1m$ with a quarter circle notch on the bottom left with radius equal to $0.2m$ was created with the boundary conditions shown in Figure 39. The 2D plate was fixed on the left boundary in both directions. A roller pinned connection was applied on the bottom right node to fix the displacement on y -direction.

Nodal forces were applied on the right side of the domain as shown in Figure 39 to introduce the displacements in both directions. Possion ratio (ν) of 0.28 was assigned to the domain with elastic modulus as 200 GPa. Then, the domain was firstly discretized with 231 lower order of approximation polynomial ($p = 1$) elements. After that, the same domain was discretized with 2521 higher order of approximation polynomial ($p = 2$) elements. Analogous to Equation 59, the SR approach is herein learning to map the following relationship:

$$S_x(x_{sim,p=1}) \rightarrow x_{sim,p=2} \quad (60)$$

$$S_y(y_{sim,p=1}) \rightarrow y_{sim,p=2} \quad (61)$$

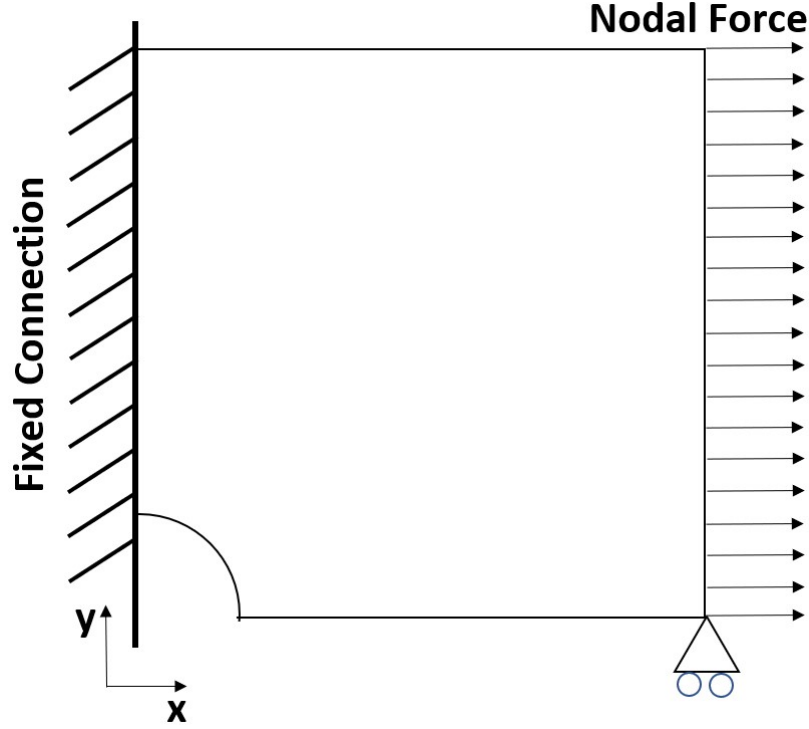


Figure 39: Boundary and loading condition of the domain used for the mechanical simulation study. The domain is fixed in x and y direction at the left boundary. Displacement in X direction are allowed on the right bottom node. Nodal forces are applied on the right boundary.

where S_x and S_y represent the NNs operators aiming to learn the mapping between displacements vectors computed from lower and higher order meshes on both directions. The aim of this proposed SR approach is to obtain more accurate results without computing on higher order elements which could lead to reduced computational cost. In order to train the NNs, a framework to generate sufficient training samples was necessary. Firstly, in order to increase the variance of the training data for the NNs, we randomized the total sum of the nodal forces using uniform distribution between 1 Newton to 50000 Newtons and secondly the mean value of the elastic modulus (E_h) was set to be 200GPa while the elastic modulus (E) were distributed randomly between $0.1E_h < E < 1.5E_h$ within the domain. Then, we established FEMs with aforementioned parameters to obtain two displacement fields modelled on lower and higher order elements. After that, we decomposed the displacements vectors to x and y directions. The reason for decomposing the displacement matrix to two directions was to have reduced number of trainable parameters of each NN. This could potentially enable the

learning process to more easily satisfy the Equation 60 and 61 with reduced architectures. The flowchart of the proposed methodology are shown in Figure 40, 41 and 42.

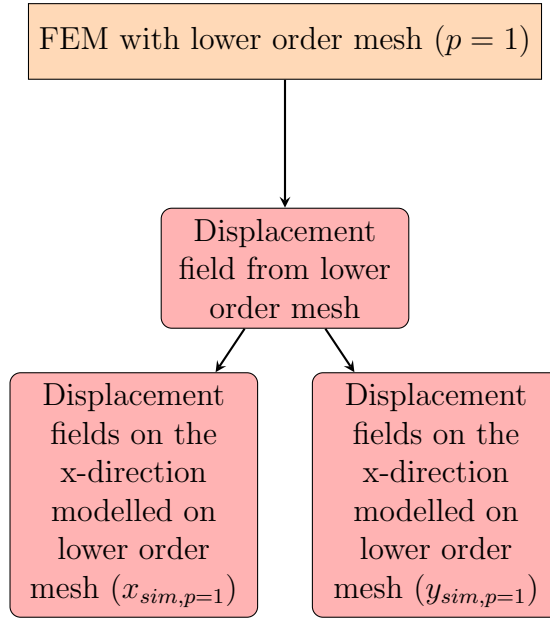


Figure 40: Flowchart of decomposing the displacement vectors modelled on lower order mesh ($p = 1$).

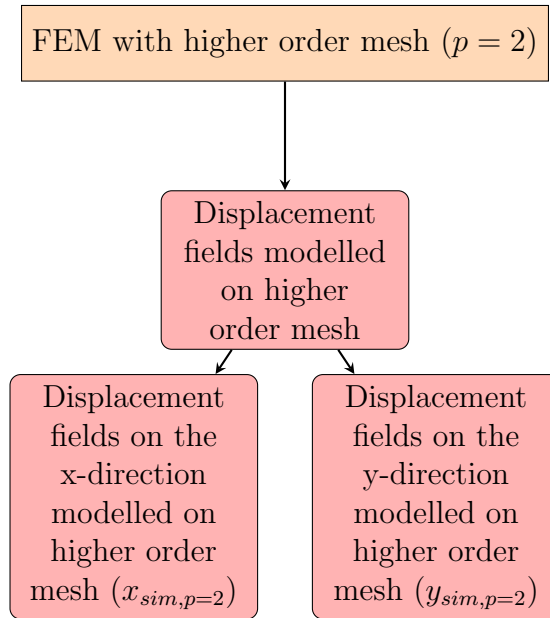


Figure 41: Flowchart of decomposing the displacement vectors modelled on lower order mesh ($p = 2$).

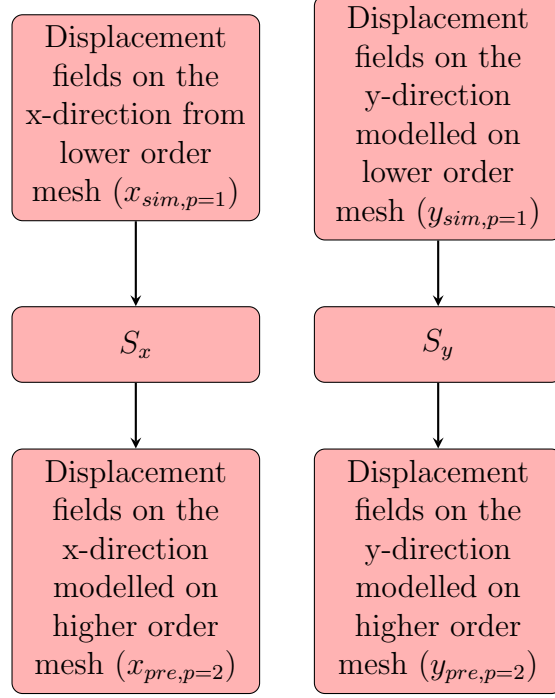


Figure 42: Flowchart of the training process of NNs S_x and S_y for the mechanical simulation study .

In order to demonstrate the feasibility of SR quantitatively, we utilized the following error functions¹ to quantify the accuracy of the proposed SR approach:

$$e_1 = (x_{sim,p=2} - x_{pre,p=2})^2 \quad (62)$$

$$e_2 = (x_{sim,p=2} - x_{sim,p=1})^2 \quad (63)$$

$$e_3 = \|(x_{sim,p=2} - x_{pre,p=2})\| \quad (64)$$

$$e_4 = \|(x_{sim,p=2} - x_{sim,p=1})\| \quad (65)$$

where $x_{sim,p=2}$ represents the simulated displacement fields of the x-direction modelled from $p = 2$ elements which were then interpolated on the $p = 1$ elements, $x_{pre,p=2}$ represents the predicted displacement fields of the x-direction by the NNs on the $p = 2$ elements which were

¹Note that the same error metrics are utilized for y-directional fields.

then interpolated on the $p = 1$ elements, while $x_{sim,p=1}$ represents the simulated displacement fields of the x-direction modelled on the $p = 1$ elements. Equation 62 and 63 expresses the mean squared error function (MSE) between those displacement vectors while Equation 64 and 65 describes the norm error function. Since we could assume more accurate results modelled from higher order approximation polynomial elements in FEMs, we could conclude that SR achieves better accuracy in the aforementioned mechanical simulation studies if it satisfies the following two equations:

$$e_2 - e_1 > 0 \tag{66}$$

$$e_3 - e_4 > 0 \tag{67}$$

The proposed SR approach was then validated against a random simulation sample using the criteria developed above. More detailed results are recorded in section 4.

7.4 Electrical Resistance Tomography Inversion

There are various NDT methodologies that could assess the structures condition locally and globally such as ultrasonic, electromagnetic, photographic, radiographic techniques (Gholizadeh 2016, Mutlib, Baharom, El-Shafie & Nuawi 2016, Montinaro, Cerniglia & Pitarresi 2018, Kong & Li 2018). However they often suffer from 1) high operational cost, 2) prior information of the potential damage location needed. Compared with traditional NDT approaches, ERT has the advantages such as rapid data collection, lower energy cost and can offer spatial monitoring on large areas (Chen, Hassan, Tallman, Huang & Smyl 2022). Furthermore, ERT is an imaging modality which can reconstruct 1) absolute internal conductivity distribution from boundary voltage measurements (Liu, Gu, Smyl, Khambampati, Deng & Du 2020) or 2) differences of internal conductivity distribution between the two different states from differences of the boundary voltage measurements (Liu, Smyl, Gu & Du 2020*b*). These two schemes are known as the absolute imaging and difference imaging, respectively. In most ERT experiments, in order to take the voltage measurements, we firstly attach numbers of electrodes on the boundary of the domain. Then currents are injected into the electrodes

in pairs, while the voltage measurements are taken from those injected electrodes. Different injection and measurement protocols can be implemented depend on the shape/dimensions of the domains aiming at obtaining the most sufficient measurement data.

ERT was initially implemented as an medical imaging technique to reconstruct organs owing to their different conductivity (Henderson & Webster 1978). Then, ERT was developed further in capacities and inductive topographies field (Yang & York 1999). In late studies, engineers successfully utilised ERT in structural health monitoring (SHM) as a non-destructive testing (NDT) modality. ERT was developed to detect damage in cement-based materials (Smyl, Pour-Ghaz & Seppänen 2018, Hallaji, Seppänen & Pour-Ghaz 2014, Smyl & Liu 2019a) as well as reconstructing stress and strain distribution on composite materials (Tallman, Gungor, Wang & Bakis 2014, Tallman, Gungor, Koo & Bakis 2017, Lestari, Pinto, La Saponara, Yasui & Loh 2016, Loyola, Briggs, Arronche, Loh, La Saponara, O’Bryan & Skinner 2013, Loh, Kim, Lynch, Kam & Kotov 2007, Loh, Hou, Lynch & Kotov 2009, Chen, Hassan, Tallman, Huang & Smyl 2022). Furthermore, researchers also used ERT to reconstruct internal moisture flow in cement materials (Hallaji, Seppänen & Pour-Ghaz 2015, Smyl 2020).

7.5 The ERT Forward Model

In order to solve the ERT inverse problem, we firstly need a forward model to map between the internal conductivity and voltage measurements. We herein adopt The Complete Electrical Model (CEM) which is utilized with FEM by discretizing the following equations:

$$\nabla \cdot (\sigma \nabla u) = 0, x \in \Omega \quad (68)$$

$$\int_{e_l} \sigma \frac{\partial u}{\partial n} dS = I_l, l = 1, \dots, L \quad (69)$$

$$\sigma \frac{\partial u}{\partial n} = 0, x \in \partial\Omega \setminus \cup_{l=1}^L e_l \quad (70)$$

$$u + z_l \sigma \frac{\partial u}{\partial n} = U_l, l = 1, \dots, L. \quad (71)$$

Equation 68 is an Laplace equation representing the steady-state current diffusion within the interested domain (Ω) while x representing the Cartesian coordinates within the domain. Equation 69 to 71 constrains the boundary conditions needed to solve Equation 68. I_l represents the current injected on the l^{th} electrode where L is the total number of electrodes. In addition, n represents the normal vector on the infinitesimal surface of Ω which is denoted as dS . Equation 71 then takes the impedance of the electrodes z_l into the CEM for more accurate modelling.

$$\sum_{l=1}^L I_l = 0 \quad (72)$$

$$\sum_{l=1}^L U_l = 0. \quad (73)$$

By enforcing Equation 72 and 73 on Equation 68, one can compute an unique solution by physically constraining the CEM to follow the current conservation law with a fixed potential reference level (Tallman & Smyl 2020). The CEM can be beneficial when it comes to generating training samples for the NNs, however in pragmatic situations, the internal conductivity is mostly likely to be the unknown which needs to be reconstructed based on the voltage measurements. We herein have an ERT inverse problem which needs an estimated but unique solution.

7.6 ERT Inverse Problem

This section presents the conventional methodology to solve an ERT inverse problem via Total Variation (TV) regularization . An regularization technique is needed to obtain an unique solution due to the ill-posed nature of the ERT inverse problem. The ill-condition is mainly due to 1) diffusive nature of the injected currents, 2) noisy experimental measurements, and 3) ill-conditioned matrices computed from solving the optimization problem. The ERT inverse problem can often be formulated as an observation model as follows:

$$V = U(\sigma) \quad (74)$$

where U represents the discretized CEM which maps σ to V . However, due to the existence of noise in measurements data, Equation 74 can be further modified as follows:

$$V = U(\sigma) + e \quad (75)$$

where e represents the sum of modelling and measurement error. Due to the aforementioned reasons, Equation 75 does not guarantee an unique solution. In order to estimate an unique solution and reduce the computational cost of the optimization algorithm, we can linearize the non-linear observation model as follows:

$$\Delta V = J\Delta\sigma + \Delta e \quad (76)$$

where Δe represents the difference in error between state 1 and 2, J represents the Jacobian matrix of one state. Detailed mathematical expressions of the terms in Equation 76 is shown in the following:

$$\Delta V = V_2 - V_1 \quad (77)$$

$$\Delta\sigma = \sigma_2 - \sigma_1. \quad (78)$$

$$J = \frac{\partial U(\sigma_1)}{\partial \sigma_1} \quad (79)$$

where ΔV and $\Delta\sigma$ represents the difference of voltage measurements and conductivity between two states. This linearized ERT observation model is the mathematical expression of the aforementioned difference imaging scheme. From Equation 76, a solution can be estimated by minimizing the following objective function:

$$\Delta\hat{\sigma} = \|L_{\Delta e}(\Delta V - J\Delta\sigma)\|^2 + \alpha\|L_R\Delta\sigma\|^2 \quad (80)$$

where $L_{\Delta e}$ and L_R represents the Cholesky factorized noise weighting and the regularization matrices respectively. In this paper, we adopt TV regularization which is known to improve the accuracy of the damage location (Tallman & Hernandez 2017, Smyl, Bossuyt, Ahmad, Vavilov & Liu 2020). Hence the one estimated solution can be formulated as follows:

$$\Delta\hat{\sigma} = (J^T W J + \Gamma_{TV}^{-1})^{-1} (J^T W \Delta V - g_{TV}) \quad (81)$$

where Γ_{TV} is the Hessian matrix of the isotropic TV function while g_{TV} is the gradient vector. In this way, we can estimate a stable, relatively accurate and unique solution for the ERT inverse problem via TV prior regularization. In pragmatic applications, despite of showing promising results in the SHM fields, ERT still suffers from high computational cost from computing the Hessian matrices (Chen, Hassan, Tallman, Huang & Smyl 2022). In addition, with more electrodes, we can easily obtain larger voltage measurements data which could significantly increase the computational cost. As a result, we face a trade-off problem between the spatial resolution of the reconstruction and the computational cost. The proposed SR approach could potentially reduce the computational cost by reconstructing the internal conductivity from up-sampled low fidelity data.

7.6.1 Experimental Inversion Study

In this section, the ERT experimental set up which was used to take the voltage measurements is introduced at first. Then, we propose the SR approach of up-sampling the voltage measurements taken from 8 electrodes to 16 electrodes using NNs. The experimental ERT voltage measurements used for validating the SR approach in this paper were taken by the KIT4 (Kuopio Impedance Tomography) measurement system. KIT4 system consists of 1) a current injection module with 16 connected electrodes, 2) voltage measurements module which transfers voltage signals, and 3) a controller module (Kourunen, Savolainen, Lehtikoinen, Vauhkonen & Heikkinen 2008). The current injections module consists of a water tank which were filled with water while plastic inclusions were placed in the tank as shown in 43.

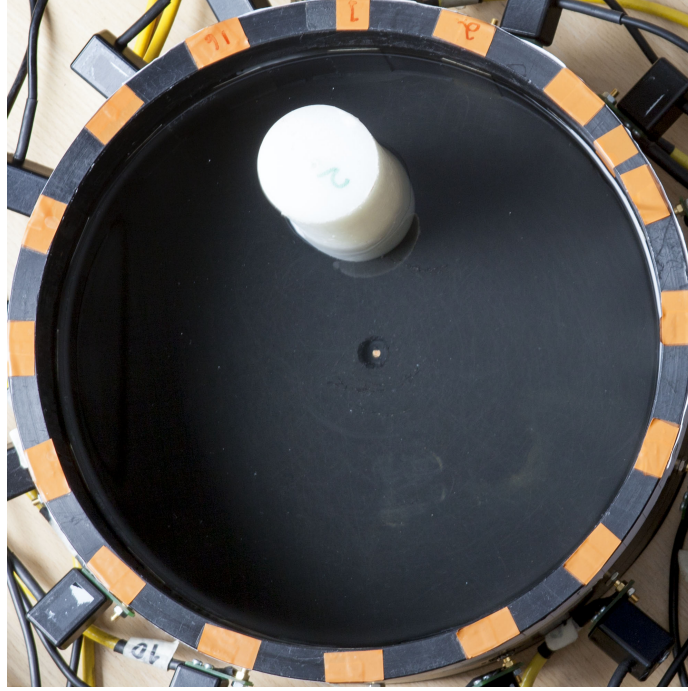


Figure 43: Experimental set up of a KIT4 current injection module which consists of a water tank with a plastic inclusion (Hauptmann, Kolehmainen, Mach, Savolainen, Seppänen & Siltanen 2017).

During the experiments, opposite injection and adjacent measurements protocols were applied on 16 electrodes to take the homogeneous measurements where there was no inclusion in the water tank. Secondly, same protocols were adapted to record the voltage measurements with rectangular and circular inclusions with different locations. Thirdly, since we were using different imaging scheme, the homogeneous voltage measurements were then subtracted from all other voltage measurements. By following the methodology described above, we obtained sets of difference voltage measurement vectors consist of 864 entries based on 16 electrodes. After this, the difference of internal conductivity were then reconstructed using TV prior regularization. These sets of data and reconstructed images were then used to validate the proposed SR approach.

The proposed SR approach utilizes NNs to up-sample the voltage measurements taken from 8 electrodes to 16 electrodes. This SR approach is expressed mathematically as follows:

$$S_V(V_8) \rightarrow V_{16} \quad (82)$$

where S_V represents the NNs operator for up-sampling the boundary measurements, while V_8 represents the difference voltage measurements from 8 electrodes while V_{16} represents the difference voltage measurements from 16 electrodes. In order to further distinguish the differences between a conventional difference imaging inversion and the proposed SR approach, we provide Figure 45 which shows the flowchart of the difference imaging scheme based on voltage measurements taken from 16 electrodes and Figure 46 which demonstrates the flowchart of the proposed SR approach.

In contemplation of sufficiently training NNs, we need a model which could simulate large amount of training samples. Herein, we firstly developed the 2D CEM of the water tank which consists of circular inclusions associated with randomized locations on each training samples. Parameters for the simulated CEM of the ERT experiments is shown in Table 13.

Table 13: Geometry and mesh details for the water tank.

| Parameter | Value |
|----------------------|--------------|
| Radius | 14cm |
| Number of Electrodes | 16 |
| Electrode Width | 2.5cm |
| Number of Elements | 2144 |
| Number of Nodes | 1145 |

This CEM was then discretized with 2144 triangular elements and 1145 nodes. The discretized domain is shown in Figure 44. The discretized CEM was then used to generate difference voltage measurement vectors based on 16 electrodes which was later down-sampled to measurements based on 8 electrodes with the same protocols used in the ERT experiments. In this way, each training samples consists of an input vector which has 176 entries and an output vector which has 864 entries. The well-trained NNs was then able to up-sample the measurements that was later used for reconstructing the difference of internal conductivity. Both simulation and experimental reconstructions was used to validate the proposed SR approach.

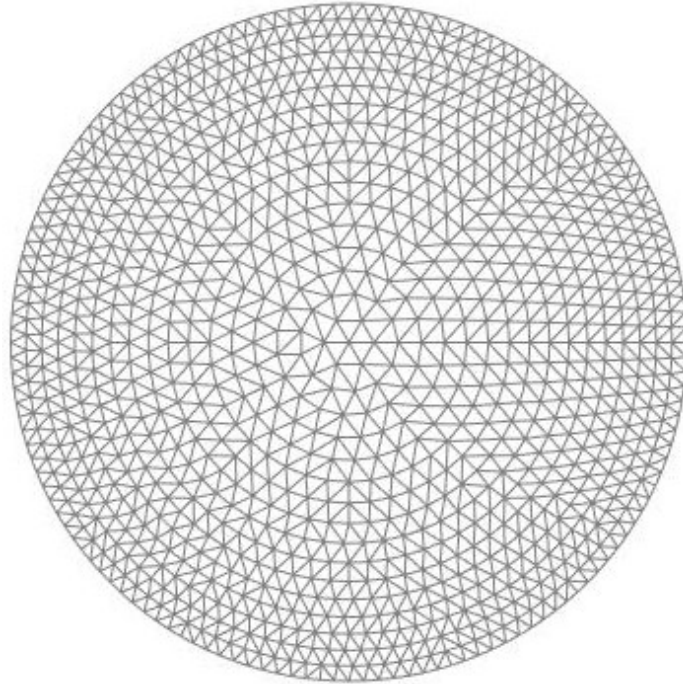


Figure 44: Water tank discretization consisting of with 1145 Nodes and 2144 Elements.

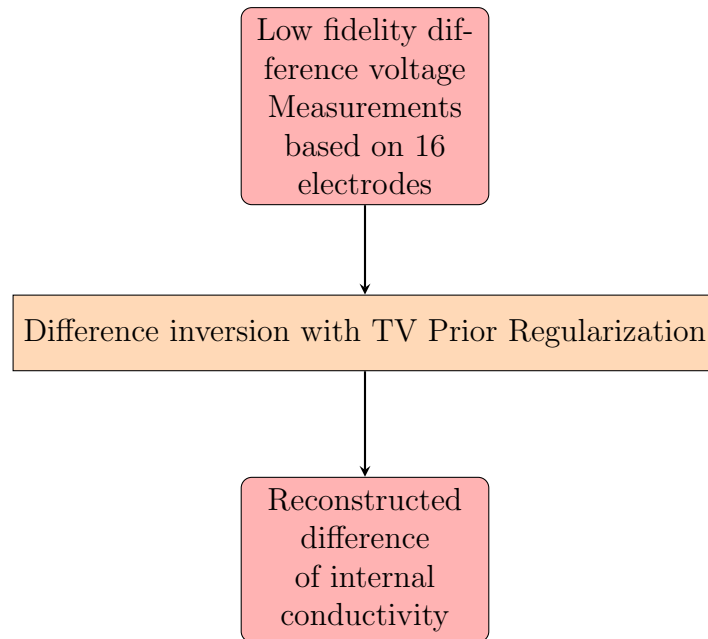


Figure 45: Flowchart of reconstructing the difference of the internal conductivity via solving the conventional ERT inverse problem based on high fidelity measurements with TV prior regularization.

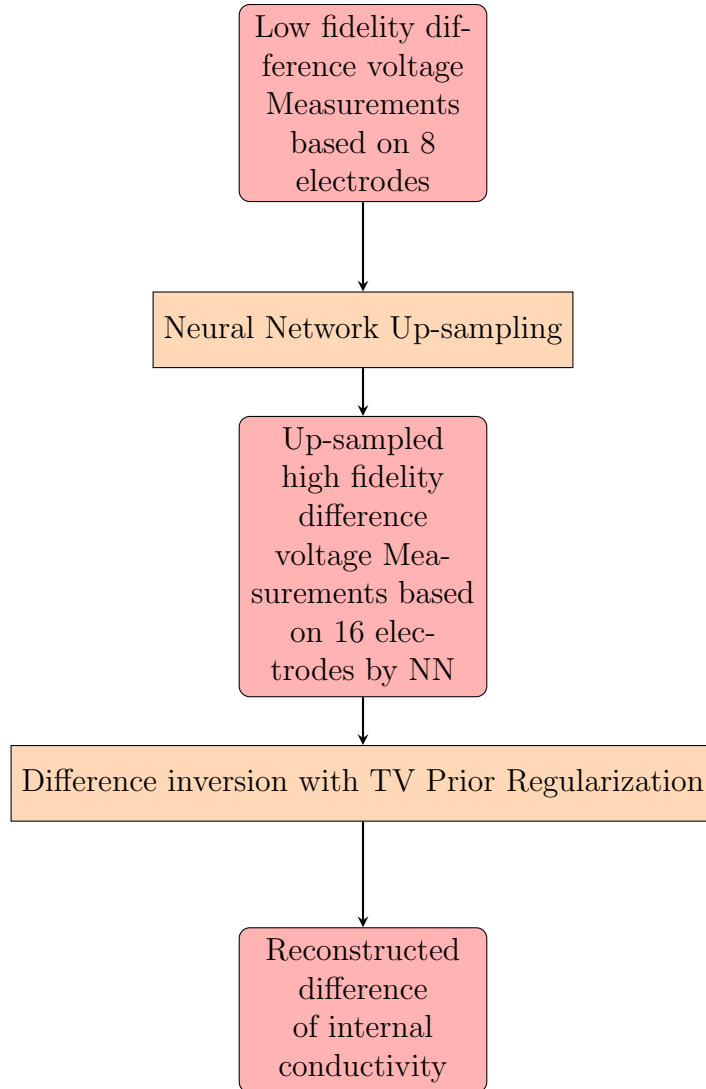


Figure 46: Flowchart of reconstructing difference of the internal conductivity via proposed SR approach based on low fidelity measurements with TV prior regularization.

7.7 Selection of the architecture of NN

7.7.1 Rationale of selecting NN

In this section, we firstly cover the rationale behind selecting NN as the technique for the propose SR approach and then the architectures of NNs used in both mechanical simulation and experimental inversion studies are provided. For the proposed SR approach, we are essentially mapping from an input vector with fewer entries to an output vector with more entries. Herein, the NNs implemented for the SR approach is learning to solve regression problems. We selected NN as the deep learning technique for the proposed methodology due to the following reasons: 1) learning tasks are highly non-linear, 2) presence of the

continuous training data (displacement field for the mechanical study and boundary voltage measurements for the ERT inversion study), 3) potential of pragmatic applications over large area and 4) controllable training process (An & Cercone 1999, Ying 2019, Ertekin & Hopper 2006).

7.7.2 Architecture of selected NNs

In this section, we firstly introduce the detailed architectures of selected NNs followed by presenting the training curves of the NNs for both studies. We want to address that the architectures of NNs were selected by adjusting NNs’ hyperparameters aiming at 1) satisfying Equation 66 and 67 and 2) minimizing the error function.

For the mechanical simulations study, the same NN architectures were used to train the displacement fields in both directions which are denoted as $\mathcal{X}_{\mathcal{D}}$ and $\mathcal{Y}_{\mathcal{D}}$. Each NN consists of 1) an input layer which has 231 neurons, 2) an fully connected layer with 462 neurons followed by a dropout layer, and then 3) an output layer with 2521 neurons. LeakyRelu functions were used as the activation function for all layers. More detailed architecture with learnables weights are shown in Table 14. Training curves for $\mathcal{X}_{\mathcal{D}}$ and $\mathcal{Y}_{\mathcal{D}}$ are shown in Figure 47 and 48. The training processes were terminated when the error ceased to decrease more than 10% within 500 epochs. We used this early-stopping to prevent the NNs from over-fitting the training data. Sharp reduction of the error can be observed at the early epochs which indicates the improved learning performance of the NNs. A steady plateau error loss indicates the gradient descent algorithm has reached at least a local minimum within the error space.

Table 14: Summary of the NN architecture S_x and S_y for up-sampling displacement fields modelled on lower order mesh.

| Input of $x_{p=1}$ or $y_{p=1}$ with size (231,1) | | | |
|---|-------------|--------------------|---------------------|
| Total number of training samples: 4900 | | | |
| Layer (Type) | Activations | Learnables Weights | Activation Function |
| Input layer | 231 | - | - |
| Fully connected layer | 462 | 107, 184 | LeakyReLU |
| Dropout (dropout rate : 20%) | 462 | - | - |
| Output layer | 2521 | 1, 167, 223 | LeakyReLU |
| Output of $x_{p=2}$ or $y_{p=2}$ with size (2521,1) | | | |

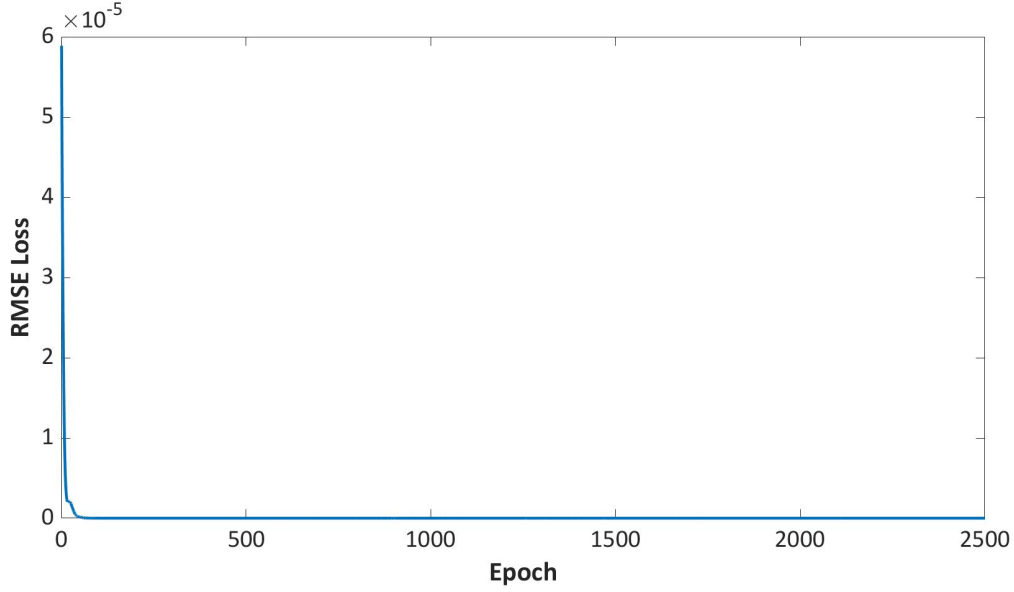


Figure 47: Loss function minimization of SR operator S_x .

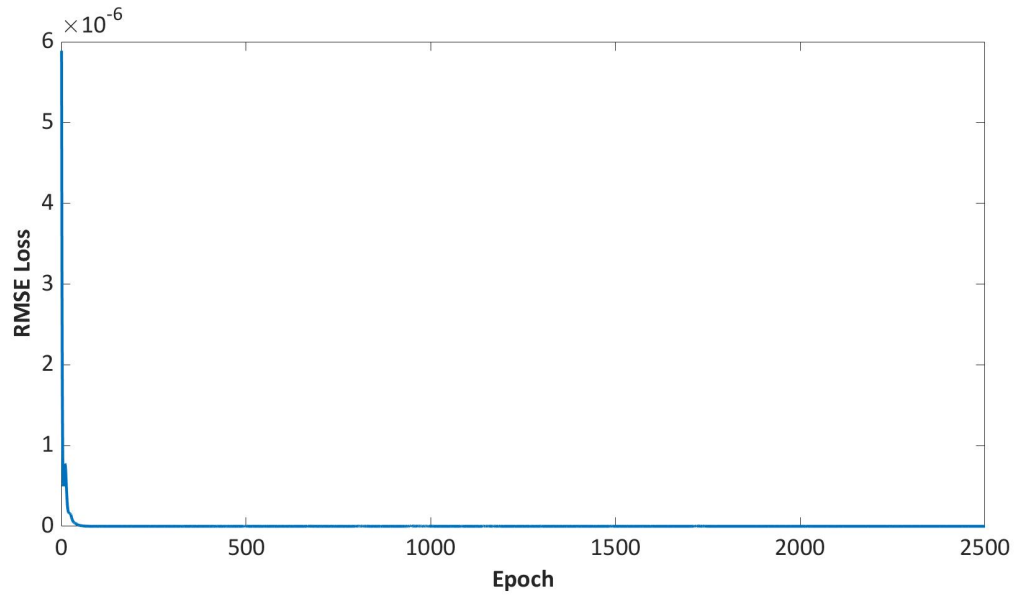


Figure 48: Loss function minimization of SR operator S_y .

For the experimental inversion study, owing to the ill-posed nature of the ERT inverse problem, small prediction error can lead to large differences on the reconstructed internal conductivity. As a result, we implemented a much deeper network than S_x and S_y . S_V consists of 1) an input layer with 176 neurons, 2) a symmetrical architecture with 4 layers consisting 100, 200, 800 and 1300 neurons respectively, and 3) an output layer with 864 neurons. LeakyReLU activation functions were applied on all layers. More detailed architecture with learnable weights are shown in Table 15. Same early-stopping protocols were implanted here

to potentially prevent the NN from over-fitting the training data. The loss function minimization curve for S_V is shown in Figure 49 and similar observations from Figure 47 and 48 can be seen here as the gradient descent algorithm was computed to minimise the MSE loss.

Table 15: Summary of the NN architecture S_V for up-sampling low fidelity voltage measurements based on 8 electrodes.

| Input of V_8 with size (176,1) | | | |
|--|-------------|--------------------|---------------------|
| Total number of training samples: 10,000 | | | |
| Layer (Type) | Activations | Learnables Weights | Activation Function |
| Input layer | 176 | - | - |
| Fully connected layer | 100 | 17,700 | LeakyReLU |
| Fully connected layer | 200 | 20,200 | LeakyReLU |
| Fully connected layer | 800 | 160,200 | LeakyReLU |
| Fully connected layer | 1300 | 1,691,300 | LeakyReLU |
| Fully connected layer | 1300 | 1,691,300 | LeakyReLU |
| Fully connected layer | 1300 | 1,691,300 | LeakyReLU |
| Fully connected layer | 800 | 160,200 | LeakyReLU |
| Fully connected layer | 200 | 20,200 | LeakyReLU |
| Fully connected layer | 100 | 17,700 | LeakyReLU |
| Output layer | 864 | 87,264 | LeakyReLU |
| Output of V_{16} with size (864,1) | | | |

7.8 Results

7.8.1 Mechanical simulation study evaluation

In this section we firstly report the quantitative and qualitative evaluations of the mechanical simulation study followed by the experimental inversion validation of the SR approach. MSE and Norm error for e_1 and e_2 in both directions from the simulation mechanical study are shown in Table 16. We can observe that Equation 66 and 67 are satisfied in both directions in terms of both error criteria. This quantitative results indicate that the proposed SR approach can potentially offer more accurate results on this mechanical simulation case without constructing FEMs on higher order meshes.

In Figure 50, we report the displacement fields results modelled on higher and lower order meshes. All displacement results are interpolated on the lower order ($p = 1$) elements for the convenience of comparison. Firstly, we can conclude intuitively that SR approach yields

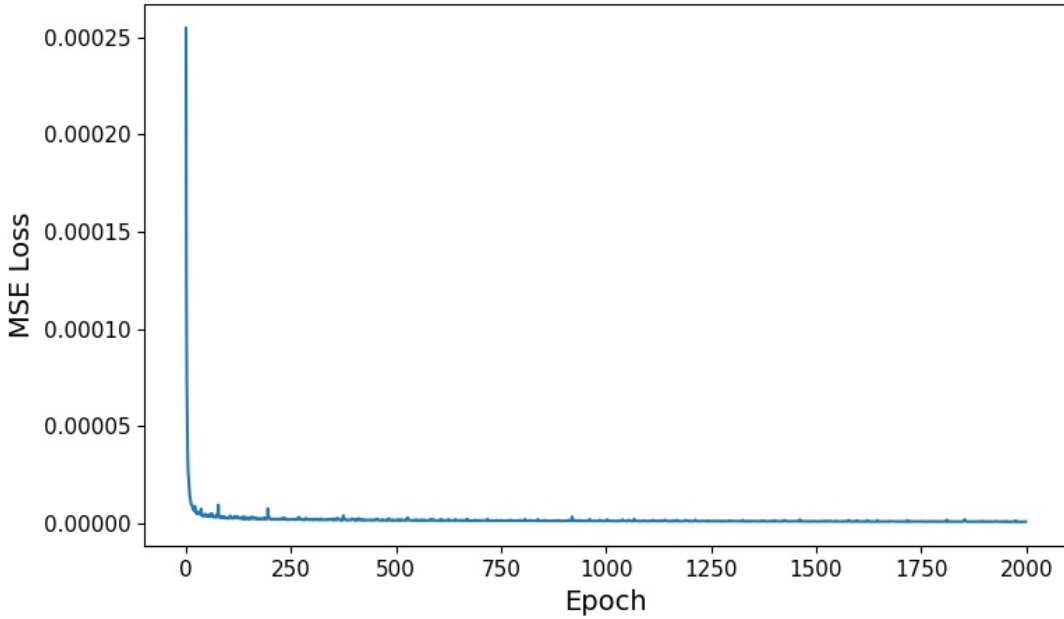


Figure 49: Loss function minimization of SR operator S_V .

similar displacement fields results qualitatively. In addition, we can observe more detailed displacement fields appearing on the right top and bottom regions of the domain in both directions. This observation is consistent with the error analysis presented in Table 16 where the predicted displacement fields based on SR approach offers generally more accurate results. Discussion in term of the mechanical study will be provided henceforth.

Table 16: MSE and norm error analysis of the mechanical simulations study.

| | x-direction | | y-direction | |
|------------|-------------------------|-------------------------|--------------------------|-------------------------|
| Error Type | e_1 | e_2 | e_1 | e_2 |
| Norm error | 2.997×10^{-4} | 0.0262 | 1.109×10^{-4} | 0.0077 |
| MSE error | 3.884×10^{-10} | 5.0183×10^{-8} | 0.3279×10^{-11} | 3.3449×10^{-9} |

7.8.2 Experimental inversion study validation

For the experimental inverse study validation, we firstly use the simulation samples to evaluate qualitatively of the SR approach. As shown in Figure 51, column (a) shows the simulated reconstruction of the difference internal conductivity reconstruction with a circular inclusion while column (b) shows the reconstruction results from the proposed SR approach. Results from SR approach generally captures the correct location and sizing of the inclusion as well

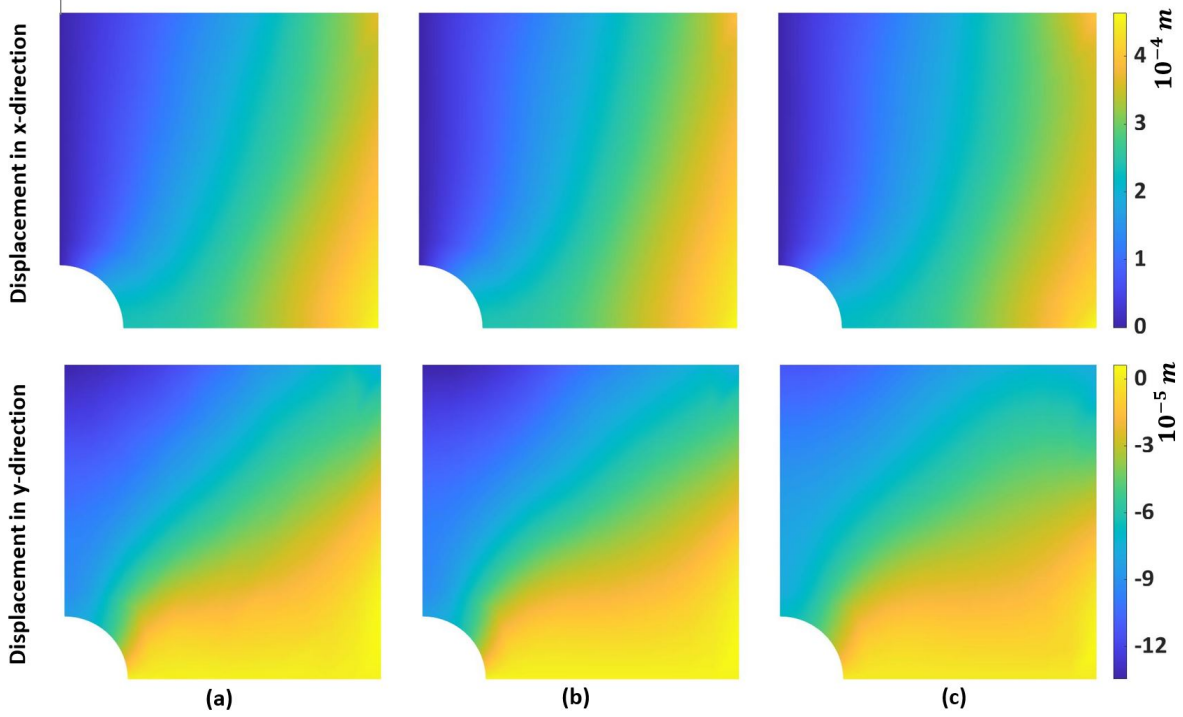


Figure 50: Comparison between the displacement field yielded from the SR approach and the simulation results: a) Predicted displacement field modelled on $p = 2$ mesh which is then interpolated on $p = 1$ mesh; b) Simulated displacement field modelled on $p = 2$ mesh which is then interpolated on $p = 1$ mesh; c) Simulated displacement field modelled on $p = 1$ mesh. as the homogeneous background. However, there are also imperfections in the SR reconstructed results, for example: 1) From the colorbar we notice the magnitude of the difference conductivity value is smaller than the true value, and 2) We observe there are over-predicted values around the inclusions across all validated samples. The reasons causing these error are explained in detail in the discussing section. Secondly, we validated the SR approach with experimental ERT voltage measurements. In Figure 52, column (a) shows the 'true' locations and sizing of the inclusions during the experiments. Column (b) shows the reconstruction of the difference conductivity based on the experimental measurements taken from 16 electrodes while column(c) shows the reconstruction based on the up-sampled measurements via the SR approach. We can firstly observe that both results have similar absolute values with correct localization of the inclusions. These observations indicate the SR approach is potentially capable of up-sampling the low fidelity data to reconstruct the difference conductivity with reduced number of implemented electrodes. However, we can also observe some error such as 1) The SR based reconstruction does not show the rectangular shape of the inclusion, 2)

locations of the SR based reconstruction are not aligned with the actually position of the inclusion, and 3) reconstruction inhomogeneity of case 2 at the boundary locations. The potential reasons causing these error are provided in the following discussion section.

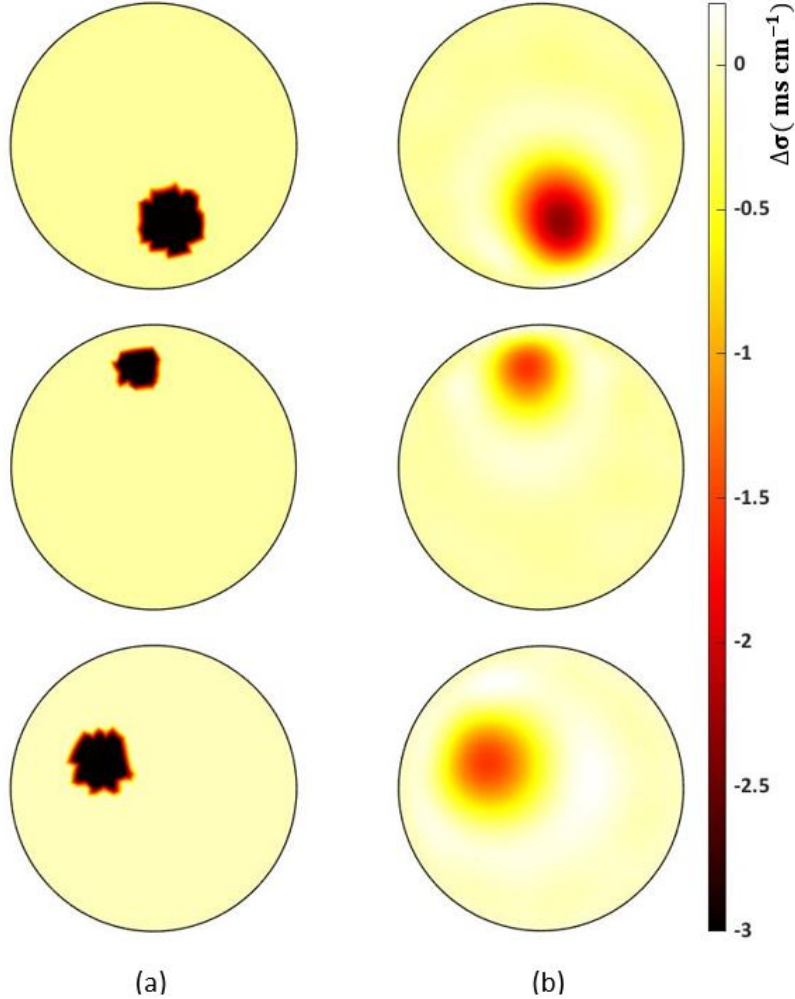


Figure 51: Comparison between the conventional reconstruction of $\Delta\sigma$ based on simulated high fidelity measurements and the reconstruction via proposed SR approach: a) TV prior reconstruction of $\Delta\sigma$ based on high fidelity, simulated measurements based on 16 electrodes; b) TV prior reconstruction of $\Delta\sigma$ based on up-sampled voltage measurements via SR approach.

Taken all the results mentioned together, we can safely conclude that the proposed SR approach successfully improves displacement fields results on this simulation mechanical study by using trained NNs to predict the displacements from lower fidelity data. In addition, the SR approach can also qualitatively up-sample the low fidelity experimental ERT data to

high fidelity data without sacrificing too much accuracy while computing the ERT inverse problem.

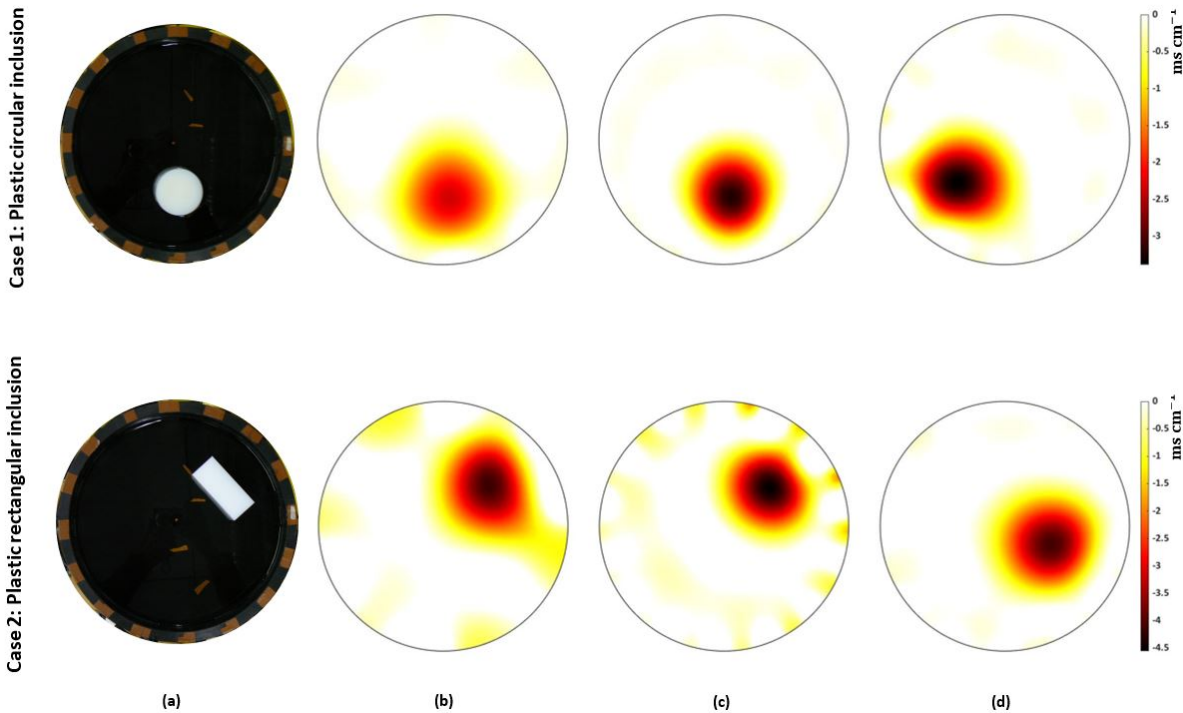


Figure 52: Comparison between the experimental images of the inclusions, the conventional reconstructions of $\Delta\sigma$ and the reconstructions of $\Delta\sigma$ via the SR approach considering two different experimental inclusion cases: a) Experimental positioning images of circular and rectangular inclusions in the water tank; b) TV prior reconstruction of $\Delta\sigma$ based on low fidelity experimental measurements (8 electrodes); c) TV prior reconstruction of $\Delta\sigma$ based on high fidelity experimental measurements (16 electrodes); d) TV prior reconstruction of $\Delta\sigma$ based on up-sampled low fidelity experimental measurements (8 electrodes).

7.9 Discussion

In this section, we first discuss the feasibility of the proposed superresolution (SR) approach in general and then compare its performance in both studies. We then delve into the potential reasons for the imperfections or errors in the results, and propose methods to improve them.

In general, the feasibility of the proposed SR approach has been validated through a mechanical simulation study and an experimental electrical resistance tomography (ERT) inversion study. The results presented above show that the proposed SR approach is capable of 1) improving displacement field results by using trained neural networks (NNs) to predict dis-

placements from lower-fidelity data and 2) up-sampling voltage measurement data for ERT inversion problems with high accuracy.

By comparing the results from both studies, we notice that the proposed SR approach yields relatively more accurate results with the mechanical simulation study, both quantitatively and qualitatively. This is likely due to several factors, such as the similarity in the distribution of inputs and outputs used to train the NNs, the well-posed nature of the mechanical simulation, and the use of simulated data as inputs for the NNs, which leads to perfectly denoised training data.

In contrast, when validating against experimental measurements in the ERT inversion study, we notice inaccuracies in the localization of inclusions. This can be attributed to several reasons, such as the limitation of implementing the SR approach on an ERT inversion problem due to its highly non-linear and ill-posed nature, the difficulty of the gradient descent algorithm in locating the global minimum within the error space, and the discrepancy between the simulated training samples and the experimental measurements, which can increase the bias of the NNs and produce errors during up-sampling.

To potentially improve the results of up-sampling the ERT voltage measurement data via the SR approach, we propose the following methods: increasing the number of training data and the depth of the NNs, which could enable the NNs to recognize more complicated non-linear relationships but at the cost of increased computational cost, and reducing the discrepancy between simulated and experimental measurements by subtracting the differences of simulation and experimental measurements at the reference state. However, it is worth noting that this may require implementing an absolute imaging scheme, as the ill-posed nature of the ERT can lead to minimal differences in absolute voltage measurements associated with inclusions at different locations, which could lead to reduced variance within the training data of the NNs, and thus may require a deeper NN architecture.

Finally, we want to address the fact that the ERT inversion reconstruction does not show the rectangular shape of the inclusion. This can be attributed to several reasons, such as the fineness of the mesh not being sufficient to present the boundary of a rectangular shape, and

the exclusion of measurements simulated with a rectangular inclusion from the training data, in order to simplify the training process of the NNs and test the generalization capability of the trained NNs.

7.10 Conclusions

This paper aims to explore the feasibility of using SR approach by validating it against mechanical simulation study and an experimental inversion problem. The results show that the SR approach can achieve the following objectives: 1) Offer more accurate numerical FEM solutions on discretized mechanical simulations and 2) up-sample the ERT voltage measurements taken from reduced number of electrodes. In addition, Further research should be conducted following the aforementioned proposals to improve the quantitative performance of the SR approach in terms of both studies. [Providing with improved overall accuracy](#), the proposed SR approach can potentially herein reduce the computational requirement/cost needed to compute FEMs and solve ERT inversion problems. Taken the results and discussions together, we can conclude that the SR approach is feasible of increasing the fidelity of the numerical solutions by using data-driven NNs and can be used in ERT inversion once the data-driven NNs can 1) predict more accurate spacial reconstruction and 2) differentiate results on various inclusion shapes.

8 Conclusion

In this section, the summaries of the three publications are provided and then we offer the potential future researches that could be conducted further. In the first paper, we used the proposed deep learned ERT framework to offer probabilistic flexural crack reconstructions using experimental ERT measurements from concrete specimens. CNNs were also utilized to reconstruct probabilistic shear cracks with simulated samples. Results show that both NNs can directly “solve” the ERT inverse problems by mapping the boundary voltage measurements to binary distributions as well as predicting the location/sizing of the potential cracks. Future research on this topic can be conducted in terms of the following aspects: 1) explore different NN architectures (e.g. recurrent neural network (RNN)) to predict the progression of future potential cracks based on temporal data, then 2) more complex cracks patterns can be incorporated into the training samples to improve the NNs performance on more realistic crack patterns, and furthermore, 3) it is also beneficial to develop one generalized NN which is trained by both flexural and shear cracks to reconstruct both crack patterns in one NN.

In the second paper, the feasibility of using NNs to directly reconstruct strain and stress fields based on ERT boundary measurements considering nanomaterials was explored. By increasing the variance of the training sample via randomized force distributions, the training performance was improved. The results show 1) the proposed framework can yield valid reconstructions of strain and stress fields under different loading conditions and 2) significantly reduce the computational cost by solving the ERT inverse problem directly. However, the proposed deep learned frameworks suffer from the trade-off problem between the generalization of the NNs and the output accuracy. Hence, we propose the following approaches that could potentially improve the overall generalization and reconstruction performance: 1) future researchers could conduct experiments on nanomaterials with different loading combinations to mimic realistic and complex loading conditions. By including training sets under those conditions, NNs could potentially predict the strain/stress fields under various loading combinations and 2) one could test the proposed deep learned framework on other piezoresistive material by conducting sensitivity studies of their responses to the deep learned ERT framework.

The third paper sets to explore the feasibility of using learned superresolution to obtain numerical solutions using low-fidelity data. The results have shown that learned superresolution can 1) yield more accurate displacement solutions from mechanical simulation studies and 2) potentially up-sample ERT voltage measurements if the model's prediction accuracy can be improved. More importantly, this learned superresolution approach can be beneficial when the computational power is limited in pragmatic applications. Future researchers can couple superresolution with other SHM data such as dynamic response measurements to reduce the computational costs.

Generally speaking, future researcher could potentially develop continuous, accurate and automatic SHM technique targeting at detect, identify and assess both local and global structural damages. NNs can be utilized to analyse sensor data and mapping patterns between sensor data and structural damage with reduced computational cost. One could also take account of the temporal data of different types of monitoring data to digitalis and potentially predict the structural damages. In addition, reinforcement learning can also be research on optimizing the layout of sensors.

In summary, we have proposed deep learned ERT frameworks to solve ERT inverse problems directly with significantly reducing computational costs. The proposed frameworks were affirmed by simulation and experimental data and has shown their potential as novel SHM frameworks considering cement-based and nanocomposite materials. More importantly, with improved generalization and overall accuracy performance, the proposed deep learned approaches can potentially be applied to other SHM modalities as well to develop integrated SHM systems which are capable of offering accurate and continuous monitoring of the structural states.

9 Bibliography

- Ackley, D. H., Hinton, G. E. & Sejnowski, T. J. (1985), ‘A learning algorithm for boltzmann machines’, *Cognitive science* **9**(1), 147–169.
- Agrawal, T. (2021), *Hyperparameter optimization in machine learning: make your machine learning and deep learning models more efficient*, Springer.
- Ainsworth, M. & Oden, J. T. (1997), ‘A posteriori error estimation in finite element analysis’, *Computer methods in applied mechanics and engineering* **142**(1-2), 1–88.
- Albawi, S., Mohammed, T. A. & Al-Zawi, S. (2017), Understanding of a convolutional neural network, in ‘2017 International Conference on Engineering and Technology (ICET)’, Ieee, pp. 1–6.
- Amsallem, D. & Farhat, C. (2008), ‘Interpolation method for adapting reduced-order models and application to aeroelasticity’, *AIAA journal* **46**(7), 1803–1813.
- An, A. & Cercone, N. (1999), Discretization of continuous attributes for learning classification rules, in ‘Pacific-Asia Conference on Knowledge Discovery and Data Mining’, Springer, pp. 509–514.
- An, J. & Cho, S. (2015), ‘Variational autoencoder based anomaly detection using reconstruction probability’, *Special Lecture on IE* **2**(1), 1–18.
- Areias, P., Reinoso, J., Camanho, P., De Sá, J. C. & Rabczuk, T. (2018), ‘Effective 2d and 3d crack propagation with local mesh refinement and the screened poisson equation’, *Engineering Fracture Mechanics* **189**, 339–360.
- Azócar, D., Elgueta, M. & Rivara, M. C. (2010), ‘Automatic lefm crack propagation method based on local lepp–delaunay mesh refinement’, *Advances in Engineering Software* **41**(2), 111–119.
- Bagwell, S., Ledger, P. D., Gil, A. J., Mallett, M. & Kruip, M. (2017), ‘A linearised hp–finite element framework for acousto-magneto-mechanical coupling in axisymmetric mri

- scanners’, *International Journal for Numerical Methods in Engineering* **112**(10), 1323–1352.
- Baharvand, S., Jozaghi, A., Fatahi-Alkouhi, R., Karimzadeh, S., Nasiri, R. & Lashkar-Ara, B. (2020), ‘Comparative study on the machine learning and regression-based approaches to predict the hydraulic jump sequent depth ratio’, *Iranian Journal of Science and Technology, Transactions of Civil Engineering* pp. 1–14.
- Balageas, D., Fritzen, C.-P. & Güemes, A. (2010), *Structural health monitoring*, Vol. 90, John Wiley & Sons.
- Baltopoulos, A., Polydorides, N., Pambaguan, L., Vavouliotis, A. & Kostopoulos, V. (2015), ‘Exploiting carbon nanotube networks for damage assessment of fiber reinforced composites’, *Composites Part B: Engineering* **76**, 149–158.
- Bao, Y., Guo, Y. & Li, H. (2020), ‘A machine learning–based approach for adaptive sparse time–frequency analysis used in structural health monitoring’, *Structural Health Monitoring* **19**(6), 1963–1975.
- Baum, E. B. (1988), ‘On the capabilities of multilayer perceptrons’, *Journal of complexity* **4**(3), 193–215.
- Bell, B. C. & Surana, K. S. (1994), ‘A space–time coupled p-version least-squares finite element formulation for unsteady fluid dynamics problems’, *International journal for numerical methods in engineering* **37**(20), 3545–3569.
- Bengio, Y. (2009), *Learning deep architectures for AI*, Now Publishers Inc.
- Benner, P., Gugercin, S. & Willcox, K. (2015), ‘A survey of projection-based model reduction methods for parametric dynamical systems’, *SIAM review* **57**(4), 483–531.
- Bentz, D. P. (2007), ‘A virtual rapid chloride permeability test’, *Cement and Concrete Composites* **29**(10), 723–731.

- Bergstra, J. & Bengio, Y. (2012), ‘Random search for hyper-parameter optimization.’, *Journal of machine learning research* **13**(2).
- Bishop, C. M. (1995), ‘Training with noise is equivalent to tikhonov regularization’, *Neural computation* **7**(1), 108–116.
- Bishop, C. M. et al. (1995), *Neural networks for pattern recognition*, Oxford university press.
- Brownlee, J. (2020), *Data preparation for machine learning: data cleaning, feature selection, and data transforms in Python*, Machine Learning Mastery.
- Burger, M., Korolev, Y. & Rasch, J. (2019), ‘Convergence rates and structure of solutions of inverse problems with imperfect forward models’, *Inverse Problems* **35**(2), 024006.
- Chakraborty, S. (2021), ‘Transfer learning based multi-fidelity physics informed deep neural network’, *Journal of Computational Physics* **426**, 109942.
- Chen, L., Gallet, A., Huang, S.-S., Liu, D. & Smyl, D. (0), ‘Probabilistic cracking prediction via deep learned electrical tomography’, *Structural Health Monitoring* **0**(0), 14759217211037236.
- Chen, L., Gallet, A., Huang, S.-S., Liu, D. & Smyl, D. (2022), ‘Probabilistic cracking prediction via deep learned electrical tomography’, *Structural Health Monitoring* **21**(4), 1574–1589.
- Chen, L., Hassan, H., Tallman, T. N., Huang, S.-S. & Smyl, D. (2022), ‘Predicting strain and stress fields in self-sensing nanocomposites using deep learned electrical tomography’, *Smart Materials and Structures* **31**(4), 045024.
- Chen, Y. & Pock, T. (2016), ‘Trainable nonlinear reaction diffusion: A flexible framework for fast and effective image restoration’, *IEEE transactions on pattern analysis and machine intelligence* **39**(6), 1256–1272.

- Cheng, K.-S., Isaacson, D., Newell, J. & Gisser, D. G. (1989), ‘Electrode models for electric current computed tomography’, *IEEE Transactions on Biomedical Engineering* **36**(9), 918–924.
- Chi, H., Zhang, Y., Tang, T. L. E., Mirabella, L., Dalloro, L., Song, L. & Paulino, G. H. (2021), ‘Universal machine learning for topology optimization’, *Computer Methods in Applied Mechanics and Engineering* **375**, 112739.
- Chollet, F. (2015), ‘keras’, <https://github.com/fchollet/keras>.
- Cover, T. M. (1965), ‘Geometrical and statistical properties of systems of linear inequalities with applications in pattern recognition’, *IEEE transactions on electronic computers* (3), 326–334.
- Domhan, T., Springenberg, J. T. & Hutter, F. (2015), Speeding up automatic hyperparameter optimization of deep neural networks by extrapolation of learning curves, *in* ‘Twenty-fourth international joint conference on artificial intelligence’.
- Du, S., Lee, J., Li, H., Wang, L. & Zhai, X. (2019), Gradient descent finds global minima of deep neural networks, *in* ‘International Conference on Machine Learning’, PMLR, pp. 1675–1685.
- Duan, X., Taurand, S. & Soleimani, M. (2019), ‘Artificial skin through super-sensing method and electrical impedance data from conductive fabric with aid of deep learning’, *Scientific reports* **9**(1), 1–11.
- Ertekin, S. & Hopper, G. (2006), Efficient support vector learning for large datasets, *in* ‘Grace Hopper Celebration of Women in Computing’, Citeseer.
- Fan, Y. & Ying, L. (2020), ‘Solving electrical impedance tomography with deep learning’, *Journal of Computational Physics* **404**, 109119.
- Farrar, C. R. & Worden, K. (2012), *Structural health monitoring: a machine learning perspective*, John Wiley & Sons.

- Ferreira, A. & Novotny, A. (2017), ‘A new non-iterative reconstruction method for the electrical impedance tomography problem’, *Inverse Problems* **33**(3), 035005.
- Feurer, M. & Hutter, F. (2019), Hyperparameter optimization, *in* ‘Automated machine learning’, Springer, Cham, pp. 3–33.
- Foucault, G., Cuillière, J.-C., François, V., Léon, J.-C. & Maranzana, R. (2008), ‘Adaptation of cad model topology for finite element analysis’, *Computer-Aided Design* **40**(2), 176–196.
- Gallo, G. J. & Thostenson, E. T. (2015), ‘Electrical characterization and modeling of carbon nanotube and carbon fiber self-sensing composites for enhanced sensing of microcracks’, *Materials today communications* **3**, 17–26.
- Gallo, G. J. & Thostenson, E. T. (2016), ‘Spatial damage detection in electrically anisotropic fiber-reinforced composites using carbon nanotube networks’, *Composite Structures* **141**, 14–23.
- García, S., Ramírez-Gallego, S., Luengo, J., Benítez, J. M. & Herrera, F. (2016), ‘Big data preprocessing: methods and prospects’, *Big Data Analytics* **1**(1), 1–22.
- Géron, A. (2022), *Hands-on machine learning with Scikit-Learn, Keras, and TensorFlow*, ” O’Reilly Media, Inc.”.
- Gholizadeh, S. (2016), ‘A review of non-destructive testing methods of composite materials’, *Procedia Structural Integrity* **1**, 50–57.
- Glorot, X., Bordes, A. & Bengio, Y. (2011), Deep sparse rectifier neural networks, *in* ‘Proceedings of the fourteenth international conference on artificial intelligence and statistics’, pp. 315–323.
- Goodfellow, I., Bengio, Y., Courville, A. & Bengio, Y. (2016), *Deep learning*, Vol. 1, MIT press Cambridge.
- Gowers, K. & Millard, S. (1999), ‘Measurement of concrete resistivity for assessment of corrosion’, *ACI Materials Journal* **96**(5).

- Grohs, P., Hornung, F., Jentzen, A. & Von Wurstemberger, P. (2018), ‘A proof that artificial neural networks overcome the curse of dimensionality in the numerical approximation of black-scholes partial differential equations’, *arXiv preprint arXiv:1809.02362* .
- Hakula, H., Hyvönen, N. & Tuominen, T. (2012), ‘On the hp-adaptive solution of complete electrode model forward problems of electrical impedance tomography’, *Journal of Computational and Applied Mathematics* **236**(18), 4645–4659.
- Hallaji, M., Seppänen, A. & Pour-Ghaz, M. (2014), ‘Electrical impedance tomography-based sensing skin for quantitative imaging of damage in concrete’, *Smart Materials and Structures* **23**(8), 085001.
- Hallaji, M., Seppänen, A. & Pour-Ghaz, M. (2015), ‘Electrical resistance tomography to monitor unsaturated moisture flow in cementitious materials’, *Cement and Concrete Research* **69**, 10–18.
- Hamilton, S. J. & Hauptmann, A. (2018), ‘Deep d-bar: Real-time electrical impedance tomography imaging with deep neural networks’, *IEEE transactions on medical imaging* **37**(10), 2367–2377.
- Hartmann, R., Held, J., Leicht, T. & Prill, F. (2010), Error estimation and adaptive mesh refinement for aerodynamic flows, in ‘ADIGMA-A European Initiative on the Development of Adaptive Higher-Order Variational Methods for Aerospace Applications’, Springer, pp. 339–353.
- Hassan, H. & Tallman, T. N. (2020a), ‘A comparison of metaheuristic algorithms for solving the piezoresistive inverse problem in self-sensing materials’, *IEEE Sensors Journal* **21**(1), 659–666.
- Hassan, H. & Tallman, T. N. (2020b), ‘Failure prediction in self-sensing nanocomposites via genetic algorithm-enabled piezoresistive inversion’, *Structural Health Monitoring* **19**(3), 765–780.

- Hauptmann, A. & Adler, J. (2020), ‘On the unreasonable effectiveness of cnns’, *arXiv preprint arXiv:2007.14745* .
- Hauptmann, A., Kolehmainen, V., Mach, N. M., Savolainen, T., Seppänen, A. & Silta-
nen, S. (2017), ‘Open 2d electrical impedance tomography data archive’, *arXiv preprint arXiv:1704.01178* .
- Henderson, R. P. & Webster, J. G. (1978), ‘An impedance camera for spatially specific
measurements of the thorax’, *IEEE transactions on bio-medical engineering* **25**(3), 250–4.
- Hopfield, J. J. (1982), ‘Neural networks and physical systems with emergent collective com-
putational abilities’, *Proceedings of the national academy of sciences* **79**(8), 2554–2558.
- Hou, T.-C. & Lynch, J. P. (2009), ‘Electrical impedance tomographic methods for sensing
strain fields and crack damage in cementitious structures’, *Journal of Intelligent Material
Systems and Structures* **20**(11), 1363–1379.
- Houston, P., Schwab, C. & Süli, E. (2002), ‘Discontinuous hp-finite element methods for
advection-diffusion-reaction problems’, *SIAM Journal on Numerical Analysis* **39**(6), 2133–
2163.
- Hughes, T. J. (2012), *The finite element method: linear static and dynamic finite element
analysis*, Courier Corporation.
- Jentzen, A., Salimova, D. & Welti, T. (2018), ‘A proof that deep artificial neural networks
overcome the curse of dimensionality in the numerical approximation of kolmogorov par-
tial differential equations with constant diffusion and nonlinear drift coefficients’, *arXiv
preprint arXiv:1809.07321* .
- Jiang, K., Wang, Z., Yi, P. & Jiang, J. (2020), ‘Hierarchical dense recursive network for
image super-resolution’, *Pattern Recognition* **107**, 107475.

- Jiang, K., Wang, Z., Yi, P., Wang, G., Lu, T. & Jiang, J. (2019), ‘Edge-enhanced gan for remote sensing image superresolution’, *IEEE Transactions on Geoscience and Remote Sensing* **57**(8), 5799–5812.
- Karhunen, K., Seppänen, A., Lehtikoinen, A., Blunt, J., Kaipio, J. P. & Monteiro, P. J. (2010), ‘Electrical resistance tomography for assessment of cracks in concrete.’, *ACI Materials Journal* **107**(5).
- Karhunen, K., Seppänen, A., Lehtikoinen, A., Monteiro, P. J. & Kaipio, J. P. (2010), ‘Electrical resistance tomography imaging of concrete’, *Cement and Concrete Research* **40**(1), 137–145.
- Karlik, B. & Olgac, A. V. (2011), ‘Performance analysis of various activation functions in generalized mlp architectures of neural networks’, *International Journal of Artificial Intelligence and Expert Systems* **1**(4), 111–122.
- Kong, X. & Li, J. (2018), ‘Vision-based fatigue crack detection of steel structures using video feature tracking’, *Computer-Aided Civil and Infrastructure Engineering* **33**(9), 783–799.
- Koo, G. & Tallman, T. (2020), ‘Higher-order resistivity-strain relations for self-sensing nanocomposites subject to general deformations’, *Composites Part B: Engineering* **190**, 107907.
- Kourunen, J., Savolainen, T., Lehtikoinen, A., Vauhkonen, M. & Heikkinen, L. (2008), ‘Suitability of a pxi platform for an electrical impedance tomography system’, *Measurement Science and Technology* **20**(1), 015503.
- Kröse, B., Krose, B., van der Smagt, P. & Smagt, P. (1993), ‘An introduction to neural networks’.
- Layssi, H., Ghods, P., Alizadeh, A. R. & Salehi, M. (2015), ‘Electrical resistivity of concrete’, *Concrete International* **37**(5), 41–46.

- LeCun, Y. A., Bottou, L., Orr, G. B. & Müller, K.-R. (2012), Efficient backprop, *in* ‘Neural networks: Tricks of the trade’, Springer, pp. 9–48.
- LeCun, Y., Bengio, Y. & Hinton, G. (2015), ‘Deep learning’, *nature* **521**(7553), 436–444.
- LeCun, Y., Bengio, Y. et al. (1995), ‘Convolutional networks for images, speech, and time series’, *The handbook of brain theory and neural networks* **3361**(10), 1995.
- LeCun, Y., Boser, B., Denker, J. S., Henderson, D., Howard, R. E., Hubbard, W. & Jackel, L. D. (1989), ‘Backpropagation applied to handwritten zip code recognition’, *Neural computation* **1**(4), 541–551.
- Ledger, P. (2012), ‘hp-finite element discretisation of the electrical impedance tomography problem’, *Computer Methods in Applied Mechanics and Engineering* **225**, 154–176.
- Lee, K. & Carlberg, K. T. (2020), ‘Model reduction of dynamical systems on nonlinear manifolds using deep convolutional autoencoders’, *Journal of Computational Physics* **404**, 108973.
- Lennie, P. (2003), ‘The cost of cortical computation’, *Current biology* **13**(6), 493–497.
- Lestari, W., Pinto, B., La Saponara, V., Yasui, J. & Loh, K. J. (2016), ‘Sensing uniaxial tensile damage in fiber-reinforced polymer composites using electrical resistance tomography’, *Smart Materials and Structures* **25**(8), 085016.
- Liu, D., Gu, D., Smyl, D., Khambampati, A. K., Deng, J. & Du, J. (2020), ‘Shape-driven eit reconstruction using fourier representations’, *IEEE Transactions on Medical Imaging* **40**(2), 481–490.
- Liu, D., Smyl, D. & Du, J. (2019), ‘A parametric level set based approach to difference imaging in electrical impedance tomography’, *IEEE transactions on Medical Imaging* **38**(1), 145–155.

- Liu, D., Smyl, D. & Du, J. (2020), ‘Nonstationary shape estimation in electrical impedance tomography using a parametric level set-based extended kalman filter approach’, *IEEE Transactions on Instrumentation and Measurement* **69**(5), 1894–1907.
- Liu, D., Smyl, D., Gu, D. & Du, J. (2020a), ‘Shape-driven difference electrical impedance tomography’, *IEEE Transactions on Medical Imaging* **39**(12), 3801–3812.
- Liu, D., Smyl, D., Gu, D. & Du, J. (2020b), ‘Shape-driven difference electrical impedance tomography’, *IEEE Transactions on Medical Imaging* **39**(12), 3801–3812.
- Liu, D. & Wang, Y. (2019), ‘Multi-fidelity physics-constrained neural network and its application in materials modeling’, *Journal of Mechanical Design* **141**(12).
- Loh, K. J., Hou, T.-C., Lynch, J. P. & Kotov, N. A. (2009), ‘Carbon nanotube sensing skins for spatial strain and impact damage identification’, *Journal of nondestructive evaluation* **28**(1), 9–25.
- Loh, K. J., Kim, J., Lynch, J. P., Kam, N. W. S. & Kotov, N. A. (2007), ‘Multifunctional layer-by-layer carbon nanotube–polyelectrolyte thin films for strain and corrosion sensing’, *Smart Materials and Structures* **16**(2), 429.
- Loyola, B. R., Briggs, T. M., Arronche, L., Loh, K. J., La Saponara, V., O’Bryan, G. & Skinner, J. L. (2013), ‘Detection of spatially distributed damage in fiber-reinforced polymer composites’, *Structural Health Monitoring* **12**(3), 225–239.
- Luo, X., Roads, B. D. & Love, B. C. (2021), ‘The costs and benefits of goal-directed attention in deep convolutional neural networks’, *Computational Brain & Behavior* **4**(2), 213–230.
- Ma, J. & Li, B. (2018), ‘Experimental and analytical studies on h-shaped reinforced concrete squat walls.’, *ACI Structural Journal* **115**(2).
- Mangalgiri, P. (1999), ‘Composite materials for aerospace applications’, *Bulletin of Materials Science* **22**(3), 657–664.

- Maulud, D. & Abdulazeez, A. M. (2020), ‘A review on linear regression comprehensive in machine learning’, *Journal of Applied Science and Technology Trends* **1**(4), 140–147.
- McCarter, W. & Garvin, S. (1989), ‘Dependence of electrical impedance of cement-based materials on their moisture condition’, *Journal of Physics D: Applied Physics* **22**(11), 1773.
- Meng, X. & Karniadakis, G. E. (2020), ‘A composite neural network that learns from multi-fidelity data: Application to function approximation and inverse pde problems’, *Journal of Computational Physics* **401**, 109020.
- Mohtasham Khani, M., Vahidnia, S., Ghasemzadeh, L., Ozturk, Y. E., Yuvalaklioglu, M., Akin, S. & Ure, N. K. (2020), ‘Deep-learning-based crack detection with applications for the structural health monitoring of gas turbines’, *Structural Health Monitoring* **19**(5), 1440–1452.
- Molini, A. B., Valsesia, D., Fracastoro, G. & Magli, E. (2019), ‘Deepsum: Deep neural network for super-resolution of unregistered multitemporal images’, *IEEE Transactions on Geoscience and Remote Sensing* **58**(5), 3644–3656.
- Montinaro, N., Cerniglia, D. & Pitarresi, G. (2018), ‘Evaluation of interlaminar delaminations in titanium-graphite fibre metal laminates by infrared ndt techniques’, *NDT & E International* **98**, 134–146.
- Mousavi, Z., Varahram, S., Ettefagh, M. M., Sadeghi, M. H. & Razavi, S. N. (2020), ‘Deep neural networks-based damage detection using vibration signals of finite element model and real intact state: An evaluation via a lab-scale offshore jacket structure’, *Structural Health Monitoring* p. 1475921720932614.
- Mutlib, N. K., Baharom, S. B., El-Shafie, A. & Nuawi, M. Z. (2016), ‘Ultrasonic health monitoring in structural engineering: buildings and bridges’, *Structural Control and Health Monitoring* **23**(3), 409–422.

- Neelakantan, A., Vilnis, L., Le, Q. V., Sutskever, I., Kaiser, L., Kurach, K. & Martens, J. (2015), ‘Adding gradient noise improves learning for very deep networks’, *arXiv preprint arXiv:1511.06807*.
- Niu, W.-J., Feng, Z.-K., Feng, B.-F., Min, Y.-W., Cheng, C.-T. & Zhou, J.-Z. (2019), ‘Comparison of multiple linear regression, artificial neural network, extreme learning machine, and support vector machine in deriving operation rule of hydropower reservoir’, *Water* **11**(1), 88.
- Nouy, A. (2010), ‘A priori model reduction through proper generalized decomposition for solving time-dependent partial differential equations’, *Computer Methods in Applied Mechanics and Engineering* **199**(23-24), 1603–1626.
- Oden, J. T., Duarte, C. & Zienkiewicz, O. C. (1998), ‘A new cloud-based hp finite element method’, *Computer methods in applied mechanics and engineering* **153**(1-2), 117–126.
- Oh, B. K., Glisic, B., Kim, Y. & Park, H. S. (2020), ‘Convolutional neural network-based data recovery method for structural health monitoring’, *Structural Health Monitoring* **19**(6), 1821–1838.
- O’Shea, K. & Nash, R. (2015), ‘An introduction to convolutional neural networks’, *arXiv preprint arXiv:1511.08458*.
- Papert, S. (1961), Some mathematical models of learning, in ‘Proceedings of the fourth London symposium on information theory’.
- Paszyński, M., Kurtz, J. & Demkowicz, L. (2006), ‘Parallel, fully automatic hp-adaptive 2d finite element package’, *Computer methods in applied mechanics and engineering* **195**(7-8), 711–741.
- Poole, B., Sohl-Dickstein, J. & Ganguli, S. (2014), ‘Analyzing noise in autoencoders and deep networks’, *arXiv preprint arXiv:1406.1831*.

- Pour-Ghaz, M., Niemuth, M. & Weiss, J. (2013), ‘Use of electrical impedance spectroscopy and conductive surface films to detect cracking and damage in cement based materials’, *Special Publication* **292**, 1–16.
- Raissi, M., Perdikaris, P. & Karniadakis, G. E. (2017), ‘Inferring solutions of differential equations using noisy multi-fidelity data’, *Journal of Computational Physics* **335**, 736–746.
- Rashetnia, R., Alla, O. K., Gonzalez-Berrios, G., Seppanen, A. & Pour-Ghaz, M. (2018), ‘Electrical resistance tomography-based sensing skin with internal electrodes for crack detection in large structures’, *Materials Evaluation* **76**(10), 1405–1413.
- Reddy, J. N. (2019), *Introduction to the finite element method*, McGraw-Hill Education.
- Ren, S., Sun, K., Tan, C. & Dong, F. (2019), ‘A two-stage deep learning method for robust shape reconstruction with electrical impedance tomography’, *IEEE Transactions on Instrumentation and Measurement* **69**(7), 4887–4897.
- Rosenblatt, F. (1958), ‘The perceptron: a probabilistic model for information storage and organization in the brain.’, *Psychological review* **65**(6), 386.
- Rumelhart, D. E., Hinton, G. E. & Williams, R. J. (1986), ‘Learning representations by back-propagating errors’, *nature* **323**(6088), 533–536.
- Sarvas, J. (1987), ‘Basic mathematical and electromagnetic concepts of the biomagnetic inverse problem’, *Physics in Medicine & Biology* **32**(1), 11.
- Saxe, J. & Berlin, K. (2015), Deep neural network based malware detection using two dimensional binary program features, in ‘2015 10th International Conference on Malicious and Unwanted Software (MALWARE)’, IEEE, pp. 11–20.
- Seo, J. K., Kim, K. C., Jargal, A., Lee, K. & Harrach, B. (2019), ‘A learning-based method for solving ill-posed nonlinear inverse problems: a simulation study of lung eit’, *SIAM journal on Imaging Sciences* **12**(3), 1275–1295.

- Seppänen, A., Hallaji, M. & Pour-Ghaz, M. (2017), ‘A functionally layered sensing skin for the detection of corrosive elements and cracking’, *Structural Health Monitoring* **16**(2), 215–224.
- Shi, L., Lu, Y. & Guan, R. (2019), ‘Detection of crack development in steel fibre engineered cementitious composite using electrical resistivity tomography’, *Smart Materials and Structures* **28**(12), 125011.
- Shirzad, A., Tabesh, M. & Farmani, R. (2014), ‘A comparison between performance of support vector regression and artificial neural network in prediction of pipe burst rate in water distribution networks’, *KSCE Journal of Civil Engineering* **18**(4), 941–948.
- Simoncelli, E. P. (1994), Design of multi-dimensional derivative filters, in ‘Proceedings of 1st international Conference on image Processing’, Vol. 1, IEEE, pp. 790–794.
- Simos, T. E. (2011), *Recent Advances in Computational and Applied Mathematics*, Springer.
- Smoliński, S. & Radtke, K. (2017), ‘Spatial prediction of demersal fish diversity in the baltic sea: comparison of machine learning and regression-based techniques’, *ICES Journal of Marine Science* **74**(1), 102–111.
- Smyl, D. (2020), ‘Electrical tomography for characterizing transport properties in cement-based materials: A review’, *Construction and Building Materials* **244**, 118299.
- Smyl, D., Bossuyt, S., Ahmad, W., Vavilov, A. & Liu, D. (2020), ‘An overview of 38 least squares-based frameworks for structural damage tomography’, *Structural Health Monitoring* **19**(1), 215–239.
- Smyl, D., Hallaji, M., Seppänen, A. & Pour-Ghaz, M. (2016), ‘Quantitative electrical imaging of three-dimensional moisture flow in cement-based materials’, *International Journal of Heat and Mass Transfer* **103**, 1348–1358.
- Smyl, D. & Liu, D. (2019a), ‘Damage tomography as a state estimation problem: Crack detection using conductive area sensors’, *IEEE Sensors Letters* **3**(10), 1–4.

- Smyl, D. & Liu, D. (2019b), ‘Less is often more: Applied inverse problems using hp-forward models’, *Journal of Computational Physics* **399**, 108949.
- Smyl, D. & Liu, D. (2020), ‘Optimizing electrode positions in 2-d electrical impedance tomography using deep learning’, *IEEE Transactions on Instrumentation and Measurement* **69**(9), 6030–6044.
- Smyl, D., Pour-Ghaz, M. & Seppänen, A. (2018), ‘Detection and reconstruction of complex structural cracking patterns with electrical imaging’, *NDT & E International* **99**, 123–133.
- Smyl, D., Tallman, T. N., Black, J. A., Hauptmann, A. & Liu, D. (2021), ‘Learning and correcting non-gaussian model errors’, *Journal of Computational Physics* **432**, 110152.
- Snoek, J., Larochelle, H. & Adams, R. P. (2012), ‘Practical bayesian optimization of machine learning algorithms’, *Advances in neural information processing systems* **25**.
- Srivastava, N., Hinton, G., Krizhevsky, A., Sutskever, I. & Salakhutdinov, R. (2014), ‘Dropout: a simple way to prevent neural networks from overfitting’, *The journal of machine learning research* **15**(1), 1929–1958.
- Stanley, R. K. & Moore, P. O. (1995), *Nondestructive Testing Handbook V. 9: Special Non-destructive Testing Methods*, ASNT.
- Surana, K. S. & Reddy, J. N. (2016), *The finite element method for boundary value problems: mathematics and computations*, CRC press.
- Takeda, T., Shindo, Y., Kuronuma, Y. & Narita, F. (2011), ‘Modeling and characterization of the electrical conductivity of carbon nanotube-based polymer composites’, *Polymer* **52**(17), 3852–3856.
- Tallman, T., Gungor, S., Koo, G. & Bakis, C. (2017), ‘On the inverse determination of displacements, strains, and stresses in a carbon nanofiber/polyurethane nanocomposite from conductivity data obtained via electrical impedance tomography’, *Journal of Intelligent Material Systems and Structures* **28**(18), 2617–2629.

- Tallman, T., Gungor, S., Wang, K. & Bakis, C. (2014), ‘Damage detection and conductivity evolution in carbon nanofiber epoxy via electrical impedance tomography’, *Smart Materials and Structures* **23**(4), 045034.
- Tallman, T. & Hernandez, J. (2017), ‘The effect of error and regularization norms on strain and damage identification via electrical impedance tomography in piezoresistive nanocomposites’, *NDT & E International* **91**, 156–163.
- Tallman, T. N., Gungor, S., Wang, K. & Bakis, C. E. (2015), ‘Damage detection via electrical impedance tomography in glass fiber/epoxy laminates with carbon black filler’, *Structural Health Monitoring* **14**(1), 100–109.
- Tallman, T. N. & Smyl, D. J. (2020), ‘Structural health and condition monitoring via electrical impedance tomography in self-sensing materials: a review’, *Smart Materials and Structures* **29**(12), 123001.
- Tallman, T. & Wang, K. (2013), ‘An arbitrary strains carbon nanotube composite piezoresistivity model for finite element integration’, *Applied Physics Letters* **102**(1), 011909.
- Tallman, T. & Wang, K. (2016), ‘An inverse methodology for calculating strains from conductivity changes in piezoresistive nanocomposites’, *Smart Materials and Structures* **25**(11), 115046.
- Tan, C., Lv, S., Dong, F. & Takei, M. (2018), ‘Image reconstruction based on convolutional neural network for electrical resistance tomography’, *IEEE Sensors Journal* **19**(1), 196–204.
- Thomas, A., Kim, J., Tallman, T. & Bakis, C. (2019), ‘Damage detection in self-sensing composite tubes via electrical impedance tomography’, *Composites Part B: Engineering* **177**, 107276.
- Tibaduiza, D., Torres-Arredondo, M. Á., Vitola, J., Anaya, M. & Pozo, F. (2018), ‘A damage classification approach for structural health monitoring using machine learning’, *Complexity* **2018**.

- Vauhkonen, M. (1997), ‘Electrical impedance tomography and prior information’.
- Vauhkonen, M., Vadasz, D., Karjalainen, P. A., Somersalo, E. & Kaipio, J. P. (1998), ‘Tikhonov regularization and prior information in electrical impedance tomography’, *IEEE transactions on medical imaging* **17**(2), 285–293.
- Vilhunen, T., Kaipio, J., Vauhkonen, P., Savolainen, T. & Vauhkonen, M. (2002), ‘Simultaneous reconstruction of electrode contact impedances and internal electrical properties: I. theory’, *Measurement Science and Technology* **13**(12), 1848.
- Wang, Q., Zhang, H., Li, X., Duan, X., Wang, J., Zhang, R., Zhang, H., Ma, Y., Wang, H. & Jia, J. (2021), ‘Error-constraint deep learning scheme for electrical impedance tomography (eit)’, *IEEE Transactions on Instrumentation and Measurement* .
- Wei, Z., Liu, D. & Chen, X. (2019), ‘Dominant-current deep learning scheme for electrical impedance tomography’, *IEEE Transactions on Biomedical Engineering* **66**(9), 2546–2555.
- Wu, J. (2017), ‘Introduction to convolutional neural networks’, *National Key Lab for Novel Software Technology. Nanjing University. China* **5**, 23.
- Yang, L. & Shami, A. (2020), ‘On hyperparameter optimization of machine learning algorithms: Theory and practice’, *Neurocomputing* **415**, 295–316.
- Yang, W. & York, T. (1999), ‘New ac-based capacitance tomography system’, *IEE Proceedings-Science, Measurement and Technology* **146**(1), 47–53.
- Yeo, K., Hwang, Y., Liu, X. & Kalagnanam, J. (2019), ‘Development of hp-inverse model by using generalized polynomial chaos’, *Computer Methods in Applied Mechanics and Engineering* **347**, 1–20.
- Ying, X. (2019), An overview of overfitting and its solutions, *in* ‘Journal of Physics: Conference Series’, Vol. 1168, IOP Publishing, p. 022022.

Yu, T. & Bui, T. Q. (2018), ‘Numerical simulation of 2-d weak and strong discontinuities by a novel approach based on xfem with local mesh refinement’, *Computers & Structures* **196**, 112–133.

Zhang, S., Gain, A. L. & Norato, J. A. (2020), ‘Adaptive mesh refinement for topology optimization with discrete geometric components’, *Computer Methods in Applied Mechanics and Engineering* **364**, 112930.

Zhou, X., Bhat, P., Ouyang, H. & Yu, J. (2017), ‘Localization of cracks in cementitious materials under uniaxial tension with electrical resistance tomography’, *Construction and Building Materials* **138**, 45–55.

10 Appendix

In this appendix I offer more insight regarding 1) constructing training data for NN training and 2) tuning of hyperparameters during NN training. I have also summarised my research experience based on the work done related to this thesis to offer suggestions to future researcher who are keen to continue the work but has faced difficulties with the two mentioned problems above.

10.1 Hyperparameter Tuning in Neural Network Training

Aiming at minimizing the cost function of NN training, one needs to constantly adjust the hyperparameters of the NNs to improve their performance. According to recent studies, the following techniques are used to achieve this goal: 1) Bayesian Optimization, which utilizes probabilistic models to compare the NNs' performances with various hyperparameter settings. This technique is often seen as efficient but difficult to implement (Snoek, Larochelle & Adams 2012). 2) Grid Search, a technique that tests different combinations of hyperparameters with predefined ranges and finally chooses the parameters that yield the least error. This technique can therefore require high computation cost. 3) Random Search, a similar technique to Grid Search, but potentially more efficient since it randomly samples the hyperparameters from the defined range rather than testing all possible combinations (Bergstra & Bengio 2012). 4) In addition, one can take a hybrid approach by combining the techniques mentioned above with potential optimization algorithms to localize the optimized hyperparameters (Domhan, Springenberg & Hutter 2015, Agrawal 2021, Feurer & Hutter 2019, Yang & Shami 2020).

In my research mentioned in this thesis, the criteria of selecting the hyperparameter is choosing the combination that yield the least error. I took a hybrid approach with Grid and Random Search. The main reasons are as follows: 1) With all available and proven working techniques mentioned above, the selection and tuning of hyperparameters are still highly independent of NNs' architecture and the training tasks, hence with limited previous research related to these fields, it is hard, for example, to establish a Bayesian probabilistic model. 2) In addition, with limited computational power and limited research program time,

the trade-off problem of computation cost and output performance needs to be carefully balanced.

10.2 Generating and Pre-Process of training data for Neural Networks

Aiming to reduce overall training time and improve performance, when generating training data, one should: 1) Ensure the simulated data distribution and accuracy are close to real-time data. 2) Carefully consider and treat the quantity of data as an essential hyperparameter to provide sufficient information for the training task and avoid overfitting in neural networks. 3) Ensure the variance of the training data is sufficient to reach required generalization performance, and that the proportion of different data classes is equal. 4) Use relevant augmentation techniques to increase the dataset size. (Goodfellow, Bengio, Courville & Bengio 2016, Géron 2022, García, Ramírez-Gallego, Luengo, Benítez & Herrera 2016, Brownlee 2020).

In my thesis, I regularly use different techniques to ensure the noisiness in our training data are reduced and the data quality are satisfying sufficient for network trainings. For example, the mesh sizing in our FEA modelling was chosen to provide sufficient data but also without reaching high dimensional training space. In addition, in our second research project, simulated elastic modulus distribution and the applied force distribution were randomized to ensure the variance of the training for better generalization performance. More detailed methodologies implemented can be found in Chapter 5.6.2 and 6.7.2.